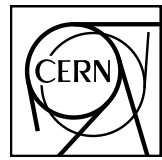


EUROPEAN ORGANIZATION FOR NUCLEAR RESEARCH



September 5, 2018

D-hadron correlations in pp collisions at $\sqrt{s_{\text{NN}}} = 5.02 \text{ TeV}$

F. Colamaria, S. Kumar, M. Mazzilli

Abstract

In this note, we present the analysis of azimuthal correlations of D mesons and primary charged π, K, p, e, μ performed in the ALICE central barrel in pp collisions at $\sqrt{s_{\text{NN}}} = 5.02 \text{ TeV}$, from 2017 data taking. The analysis is performed in an extended p_T range and with additional observables with respect to pp 2013 data analysis. After a description of the analysis strategy, corrections and systematic uncertainties, the results obtained for prompt D^0, D^{*+} and D^+ mesons in different ranges of transverse momentum of the D meson and of the associated particles are presented. The results are then compared to perturbative QCD inspired Monte Carlo models and also with pp at 7 and 13 TeV analysis results for the common p_T ranges as well as with the 2016 p-Pb results.

1 **Contents**

2	1	Introduction and Motivation	3
3	2	Data/Monte Carlo samples and event selection	4
4	3	Analysis strategy	6
5	3.1	Mass plots and cut optimization	9
6	3.1.1	Extension to very-low p_T of D mesons	13
7	3.2	Code used for the analysis	14
8	3.3	Further details on corrections	14
9	3.3.1	Event Mixing	14
10	3.3.2	Tracking and D-meson trigger efficiency	22
11	3.3.3	Correction for bias on B to D decay topologies	28
12	3.3.4	Secondary track contamination	31
13	3.3.5	Beauty feed-down	35
14	4	Systematic uncertainties on $\Delta\phi$ correlation distributions	36
15	4.1	Uncertainty on S and B extraction	36
16	4.2	Uncertainty on background correlation shape	36
17	4.3	Uncertainty on D-meson cut stability	40
18	4.4	Uncertainty on tracking efficiency evaluation	49
19	4.5	Uncertainty on secondary particle contamination	49
20	4.6	Uncertainty on feed-down subtraction	53
21	4.7	Uncertainty on correction for the bias on B to D decay topologies	53
22	4.8	Summary table	54
23	5	Results	56
24	5.1	Comparing the three D meson correlation distributions	56
25	5.2	Average of D^0 , D^+ and D^{*+} results	62
26	5.3	Fit of correlation distributions and observables	67
27	5.3.1	Generalized Gaussian for near-side peak	73
28	5.4	Systematic uncertainties on fit observables	81
29	5.5	Results for near-side yield and width, away-side yield and width, and baseline	81
30	5.6	Final plots and comparisons	91
31	5.6.1	Comparisons of pp and p–Pb at 5 TeV	91

32	5.6.2 Comparisons of pp at 5, 7 and 13 TeV	96
33	5.6.3 Comparisons of pp at 5 TeV and model predictions	96
34	5.7 Planned results for HP approvals	110
35	6 Bibliography	111

36 1 Introduction and Motivation

37 The study of the azimuthal correlations of heavy-flavour particles and charged particles at the LHC
 38 energies provides a way to characterize charm production and fragmentation processes in pp collisions.
 39 The measurement also provide a way to probe our understanding of QCD in the perturbative regime,
 40 accessible in a large kinematic range given the large mass of heavy quarks. Flavour conservation in
 41 QCD implies that charm quarks are always produced as pairs of quarks and anti-quarks. The azimuthal
 42 correlations obtained using a meson carrying a heavy quark as trigger particle with the other charged
 43 particles in the same event give the possibility to study the underlying charm production mechanism in
 44 detail. In particular, prompt charm quark-antiquark pair production is back to back in azimuth at first
 45 order in leading-order perturbative-QCD (pQCD). If a hadron from the quark hadronization is taken as
 46 trigger particle, a near-side (at $\Delta\phi = 0$) and an away-side (at $\Delta\phi = \pi$) peaks would appear in the azimuthal
 47 correlation distributions, coming from the fragmentation of the quark pair. Heavy quarks produced from
 48 the splitting of a massless gluon can be rather collimated and may generate sprays of hadrons at small
 49 $\Delta\phi$. Finally, for hard-scattering topologies classified as “flavour-excitation”, a charm quark undergoes a
 50 hard interaction from an initial splitting ($g \rightarrow c\bar{c}$), leading to a big separation in rapidity of the hadrons
 51 originating from the antiquark (quark) with respect to the trigger D meson and contribute to a rather flat
 52 term to the $\Delta\phi$ -correlation distribution.

53 In the following note, we first describe the analysis strategy for the pp 2017 data sample at $\sqrt{s} = 5$ TeV
 54 in all its steps, followed by the list of analysis corrections and the estimation of systematic uncertainties.
 55 Finally the results of $\Delta\phi$ correlations, and quantitative observable extracted to fits to those distributions,
 56 obtained for prompt D^0 , D^+ and D^{*+} in different ranges of transverse momentum for the D-meson
 57 (trigger particle) and the associated particles are presented.

58 The extension of the momentum ranges (both for D mesons and associated particles) with respect to the
 59 2010 and 2016 pp datasets (at $\sqrt{s} = 7$ TeV and $\sqrt{s} = 13$ TeV, respectively), as well as the improved
 60 precision in the common ranges allow a more thorough investigation of the charm quark fragmenta-
 61 tion properties (multiplicity of tracks as a function of momentum, geometrical profile of charm jets, p_T
 62 distribution of the tracks inside the jet). This can also allow us to put better constraints of charm frag-
 63 mentation and charm jet properties provided by models. Furthermore, 2017 pp data sample allows us a
 64 direct and more reasonable comparison with 2016 p-Pb data, since it has the same center-of-mass energy
 65 and, thanks to the higher precision and statistics, it was possible to exploit the azimuthal correlations in
 66 the same (extended and more differential) p_T ranges of both the trigger and the associated particle of the
 67 2016 p-Pb data sample (with the exclusion of the $p_T > 3$ GeV range only for the associated tracks). This
 68 new pp reference data, together with new p-Pb 2016 data will help to study cold nuclear matter effects
 69 affecting the charm fragmentation in p-Pb with better precision. In addition, this new pp data can also be
 70 used as solid and precise references in view of an analysis on a Pb-Pb sample at the same energy, which
 71 will be taken during the last weeks of 2018 data taking.

72 **2 Data/Monte Carlo samples and event selection**

73 The data used for the analyses were the AOD samples of the following four datasets: LHC17p_FAST,
 74 LHC17p_CENT_woSDD, LHC17q_FAST and LHC17q_CENT_woSDD (in all the cases, exploiting the
 75 pass1 reconstruction). The reason for choosing these data samples (in particular, those without the drifts
 76 for the CENT cluster) is explained later on, in this section. Exactly as done in the p–Pb 2016 data sample,
 77 also split in a similar fashion, it was verified, by looking at D-meson and associated charged track η and
 78 φ distributions, and at the mixed-event correlation distributions for each sub-samples, that no visible
 79 differences is present for the four periods (though the 17q samples taken alone suffer from very large
 80 statistical uncertainties), hence it was possible to perform the analysis directly on the merged samples
 81 without any bias.

82 The Monte Carlo productions adopted for this study were:

- 83 1. LHC18a4a2_fast, a HF production (HIJING with GEANT3) anchored to LHC17p,q with enrichment
 84 of heavy quarks (charm and beauty) in each of the event, produced by PYTHIA6 with Perugia2011 tune,
 85 and with forced hadronic decays of the charmed hadrons. This production was used
 86 for D-meson efficiency evaluation, purity estimation and Monte Carlo closure test.
- 87 2. LHC17l3b_fast, minimum-bias sample produced with DPMJET generator, used for the evaluation
 88 of the tracking efficiencies.

89 Table 1 shows the list of runs used for the analysis, for each of the data taking periods, and of the Monte
 90 Carlo productions used to evaluate the corrections:

91 The trigger mask request for the event selection is kINT7. Only events with a reconstructed primary
 92 vertex within 10 cm from the centre of the detector along the beam line are considered. This choice max-
 93 imises the detector coverage of the selected events, considering the longitudinal size of the interaction
 94 region, and the detector acceptances, without introducing sizeable η dependencies for the reconstruction
 95 efficiencies in the considered pseudorapidity ranges. Beam-gas events are removed by offline selec-
 96 tions based on the timing information provided by the V0 and the Zero Degree Calorimeters, and the
 97 correlation between the number of hits and track segments in the SPD detector. This is automatically
 98 performed in the Physic Selection, a positive outcome of which is required during our event selection.
 99 The pile-up cuts for out-of-bunch pile-up protection are also invoked when calling the Physics Sele-
 100 tion task. The minimum-bias trigger efficiency is 100% for events with D mesons with $p_T > 1 \text{ GeV}/c$.
 101 For the analyzed data samples, the probability of pile-up from collisions in the same bunch crossing is
 102 below 2% per triggered event (in most of the runs, well below 1%). Events in which more than one
 103 primary interaction vertex is reconstructed with the SPD detector are rejected (via a call to AliRDHF-
 104 Cuts::kRejectMVPileupEvent method with default parameters), which effectively removes the impact of
 105 pile-up events on the analysis. Out-of-bunch tracks are also effectively rejected by the Physics Selection
 106 pile-up cuts, and also by the request of at least one point in the SPD, which has a very limited time
 107 acquisition window (300 ns).
 108 Since data collected during pp 2017 data taking are distinguished into two categories - one including
 109 SDD detector (CENT_wSDD sample) and the second one without the SDD in the reconstruction, or
 110 in the acquisition (CENT_woSDD and FAST samples, respectively), a study of performance of the D-
 111 hadron correlation analysis with respect to the data samples employed has been carried out for D^{*+} and
 112 D^+ mesons (more sensitive to the presence of the SDD w.r.t. the D^0 , due to their reconstruction from
 113 three decay tracks), very similar of what was done for the p-Pb 2016 data sample (refer to p-Pb 2016
 114 analysis note at [7]), reaching exactly the same conclusion, of a more solid analysis being obtained using
 115 more uniform samples (FAST and CENT_woSDD), at the price of a slight reduction of the statistical
 116 precision.

3 Analysis strategy

The analysis follows the same strategy one used in 2016 p-Pb and pp data samples (see published paper [2] and analysis notes [8], [7]). Correlation pairs are formed by trigger particles (D mesons) reconstructed and selected in the following p_T^{trig} ranges: $3 < p_T^{\text{trig}} < 5 \text{ GeV}/c$, $5 < p_T^{\text{trig}} < 8 \text{ GeV}/c$, $8 < p_T^{\text{trig}} < 16 \text{ GeV}/c$, $16 < p_T^{\text{trig}} < 24 \text{ GeV}/c$ (the possibility of extending the analysis in $2 < p_T^{\text{trig}} < 3$ was also exploited. Further details are furnished in the next paragraph). Associated particles (charged tracks) have been reconstructed in the following p_T^{assoc} regions: $p_T^{\text{assoc}} > 0.3 \text{ GeV}/c$, $0.3 < p_T^{\text{assoc}} < 1 \text{ GeV}/c$, $p_T^{\text{assoc}} > 1 \text{ GeV}/c$, $1 < p_T^{\text{assoc}} < 2 \text{ GeV}/c$, $2 < p_T^{\text{assoc}} < 3 \text{ GeV}/c$. In this analysis, the particle identification defines the trigger particle rather than a momentum cut and therefore the momentum range of the associated particles is not constrained by that of the trigger particle. Our definition of associated particle includes primary particles of the following species: pion, kaon, proton, electron, muon. The primary particle definition comprises particle coming from the primary vertex of interaction, including those coming from strong and electromagnetic decay of unstable particles, and particles deriving from the decay of hadrons with charm or beauty. We therefore include any charged π, K, p, e, μ except those coming from weak decays of strange particles and particles produced in the interaction with the detector material. This definition corresponds to that used in the method `AliAODMCParticle::IsPyphysicalPrimary()`. All associated particles surviving the selection cuts and not matching the adopted criterion are considered as a contamination whose contribution has to be corrected for.

135

136 The analysis is performed through the following steps:

- 137 1. **D meson selection and signal extraction.** For each single event, “trigger” particles are defined
138 as the selected D meson candidates (D^0 , D^+ and D^{*+}) within a given p_T^{trig} range. The detection
139 strategy for D mesons at central rapidity is the same performed for the analyses of the D-meson
140 production at central rapidity [1], and also applied for the D-h analysis on 2010 pp, 2016 pp and
141 2016 p-Pb samples ([8], [7]). It is based on the reconstruction of decay vertices displayed from the
142 primary vertex by a few hundred μm and on the identification of the decay-particle species. The
143 identification of the charged kaon and pion in the TPC and TOF detectors is also used, to further
144 reduce the background at low p_T . An invariant-mass analysis is then used to extract the raw signal
145 yield, using the same fit functions described in [2]. The D mesons are selected in the rapidity range
146 varying from $|y| < 0.5$ at low p_T to $|y| < 0.8$ for $p_T > 5 \text{ GeV}/c$.
- 147 2. **Correlation of D candidates with associated tracks.** Particle pairs are formed by correlating each
148 trigger particle with the charged primary particles passing the track selection (excluding those
149 coming from the decay of the D-meson candidate) in a specified p_T^{assoc} interval (which can overlap
150 with the p_T^{trig} range) and in the pseudo-rapidity range $|\eta| < 0.8$. For the D^0 meson, also the low-
151 momentum pion tracks from feed-down of D^{*+} mesons are removed via 3σ invariant mass cut on
152 the $M(K\pi\pi) - M(K\pi)$ difference. This because these soft pion are not related to the charm quark
153 fragmentation chain. For D meson candidates in the invariant mass signal region, defined by a \pm
154 2σ interval around the D meson mass peak, the azimuthal angle difference $\varphi^{\text{assoc}} - \varphi^{\text{trigg}} \equiv \Delta\varphi$ and
155 the pseudorapidity difference $\eta^{\text{assoc}} - \eta^{\text{trig}} \equiv \Delta\eta$ are evaluated and stored to build two-dimensional
156 correlation distribution.
- 157 3. **Correction for limited acceptance and detector inhomogeneities with Event Mixing** The angular
158 correlation distribution may be affected, even for uncorrelated pair of particles, by structures
159 not due to physical effects, but originating from the limited detector acceptance, as well as from
160 angular inhomogeneities in the trigger and track reconstruction efficiencies as a function of $\Delta\varphi$
161 and $\Delta\eta$. Effects of this kind are removed using the Event Mixing technique. In this technique, the
162 analysis is executed on the same data sample of the standard one (called “same event” analysis,

SE), but the trigger particles found in each event are correlated to charged particles reconstructed in different events (“Mixed Events” analysis, ME) with similar characteristic, in particular concerning the event multiplicity and z position of the primary vertex (see Section 3.3.1).

The differential yield of associated particles per trigger particle is obtained by

$$\frac{1}{N_{\text{trig}}} \frac{d^2 N^{\text{pair}}}{d\Delta\eta \, d\Delta\varphi} = B_{ME}(0,0) \times \frac{S(\Delta\eta, \Delta\varphi)}{B_{ME}(\Delta\eta, \Delta\varphi)}, \quad (1)$$

where N^{pair} is the total number of correlated D-hadron pairs. The functions $S(\Delta\eta, \Delta\varphi)$ and $B_{ME}(\Delta\eta, \Delta\varphi)$ are the signal and the mixed event background distributions, respectively. The later is normalized to its value in $(\Delta\eta, \Delta\varphi) = (0,0)$, i.e. $(B(0,0))$. Further details on the mixed-event correction are provided in the next section.

4. **Subtraction of background correlation from signal distribution.** The invariant mass signal region also includes background D-meson candidates. Their contribution to the raw correlation distribution is subtracted as follows. For each p_T bin, the mean and the sigma of the invariant mass spectrum are extracted. For D^0 and D^+ , a “background” region is defined in the sidebands of the mass distribution as the interval $4 \text{ GeV}/c^2 < |m - m^{\text{pdg}}| < 8 \text{ GeV}/c^2$ (for the D^{*+} meson, only the right sideband is used). The angular correlation distribution for background candidates in this region is extracted and normalized with respect to the background in the signal region estimated from the mass fit. This normalized background correlation distribution is then subtracted from the raw signal one to obtain the signal correlation distribution. The normalization factor is the ratio of the number of background candidates under the signal peak (obtained by integrating the background of the fit function within the signal region) over the number of background candidates in the sidebands (obtained via bin-counting in the sideband region). An example of the signal region, sideband and sideband-subtracted 1D correlation distributions (along $\Delta\varphi$) is shown in figure 1, together with the comparison of the three distributions after the normalization to the number of triggers.
5. **Correction for D meson efficiency and associated track efficiency.** After filling the signal and background correlation distributions, it is necessary to take into account also for the correlations with tracks, those are not reconstructed, or not passing the quality selection due to poor reconstruction. In the same way, the loss of D-mesons which are not reconstructed, or do not pass the selection, impacts the correlation distribution shape. Hence, each pair is weighted by the inverse of the product of the associated track and D meson reconstruction efficiency, ε_{trk} and $\varepsilon_{\text{trig}}$. Further details are provided later on in this section.
6. **Projection in $\Delta\varphi$.** The limited statistics available does not allow to study the two dimensional $(\Delta\eta, \Delta\varphi)$ distribution, which is therefore projected to the $\Delta\varphi$ axis by integrating on $|\Delta\eta| < 1$. Despite, in principle, our maximum $\Delta\eta$ acceptance is of $|\Delta\eta| < 1.6$, removing the large $|\Delta\eta|$ regions allow us to reject angular regions with very low statistics, where fluctuations would be amplified by a large mixed-event correction, and avoid the so-called wings effect.
As the difference in the azimuthal angle is periodic ($\Delta\varphi = 0 = 2\pi$), the $\Delta\varphi$ -range is limited to the essential range of 2π . The $\Delta\varphi$ -limits are chosen to be $[-\pi/2, 3\pi/2]$ in order to provide a good visibility of the correlation pattern, which peaks around 0 and π .
7. **Correction for the contamination of secondary particles** The DCA to primary vertex cut, applied during the associated track selection, has the role of removing the secondary particles from the associated track sample. Secondary particles are indeed produced either from long-lived strange hadrons or from interaction of particles with the detector material. A residual contamination from secondary tracks is hence expected in the correlation distributions. This contamination

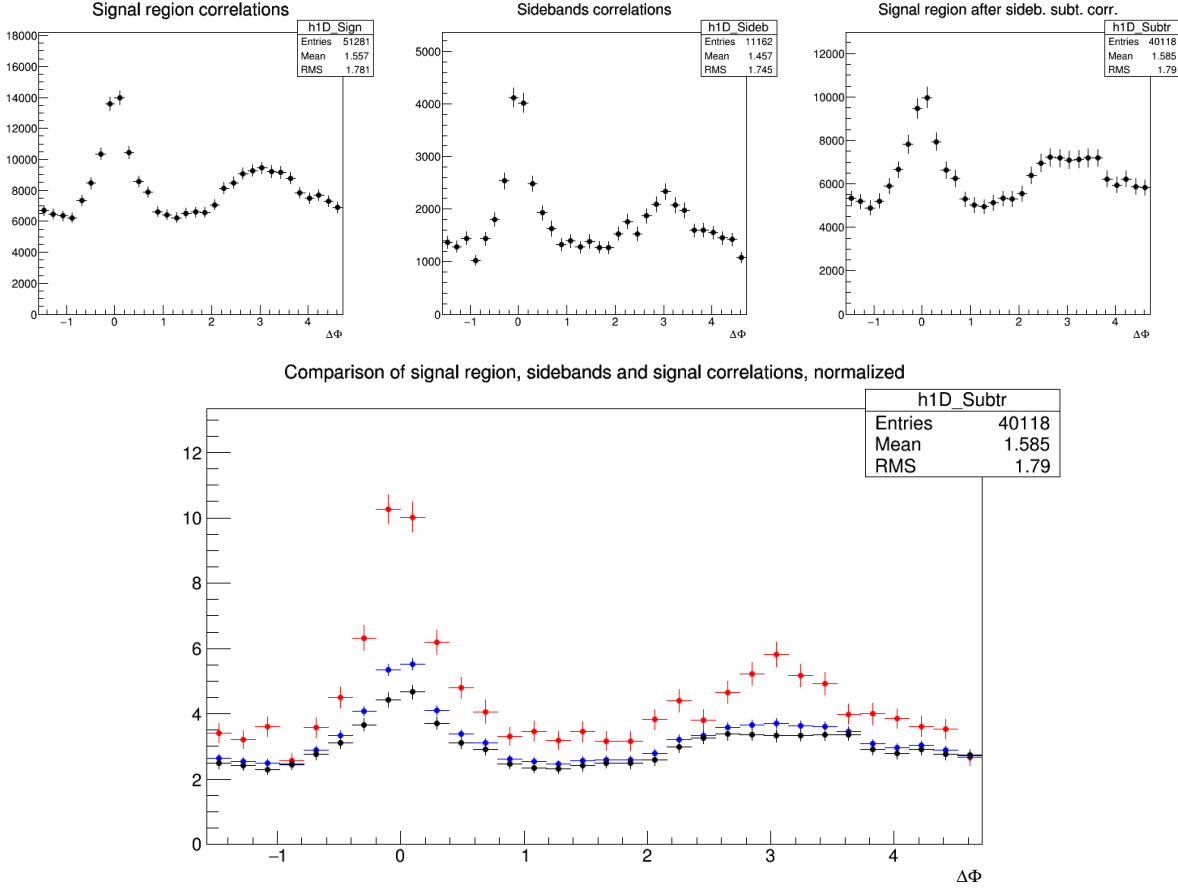


Figure 1: Top: Example of D^{*+} - h signal region (left), sideband (middle), and signal minus sideband (right) correlation distributions. Bottom: signal region per-trigger normalized correlation distribution (blue), sideband region per-trigger normalized correlation distribution (red), background-subtracted per-trigger normalized correlation distribution (black).

is estimated from Monte Carlo simulation based on Pythia as described more in detail in the next section. The background-subtracted event-mixing corrected correlations are multiplied by a purity factor to encounter this contribution.

- 8. **Correction for bias on B to D decay topologies** The presence of the topological cuts for the D-meson selection indirectly induce a bias on the topology of the B to D decay topologies, favouring cases with a small opening angle between the D-meson and the other tracks from the B decay. This affects the feed-down component of the data correlation distributions. This effect is corrected for with a procedure described in the subsection 3.3.3.
- 9. **Correction for feed-down of D meson from b-hadron decay** The selection strategy employed for the D meson candidates selection enhances the fraction of reconstructed D mesons coming from the decay of a b-hadron. Typical values, with the cuts used for the D-meson selection, are of the order of 10% or less. The correlation distribution of these secondary D mesons will be sensitive to the properties of beauty jets and beauty hadron decay, which in general differ from those relative to charm jets and hadrons. The procedure used to subtract this contribution is described in the next paragraphs of this section.
- 10. **Study of correlation properties.** The properties of the azimuthal correlation distribution are quantified by fitting the distribution with a function composed of two Gaussian functions, modelling the near and the away side peaks, and a constant term describing the baseline. The mean of the

Gaussian are fixed at $\Delta\phi = 0$ and $\Delta\phi = \pi$. To accomplish the 2π periodicity of the $\Delta\phi$ variable, the Gaussian functions are “duplicated” with mean shifted by $\Delta\phi = 2\pi$ and $\Delta\phi = -2\pi$. The fitting procedure is described in details in Section 5.

3.1 Mass plots and cut optimization

The invariant mass distributions of D^0 , D^{*+} and D^+ in the various p_T ranges are shown in Figs. 2, 3, Figs. 4, 5 and Figs. 6, 7 respectively. Note that the distributions are weighted by the D-meson selection and reconstruction efficiency, to allow a correct normalization of the correlation distributions, which have also these weights.

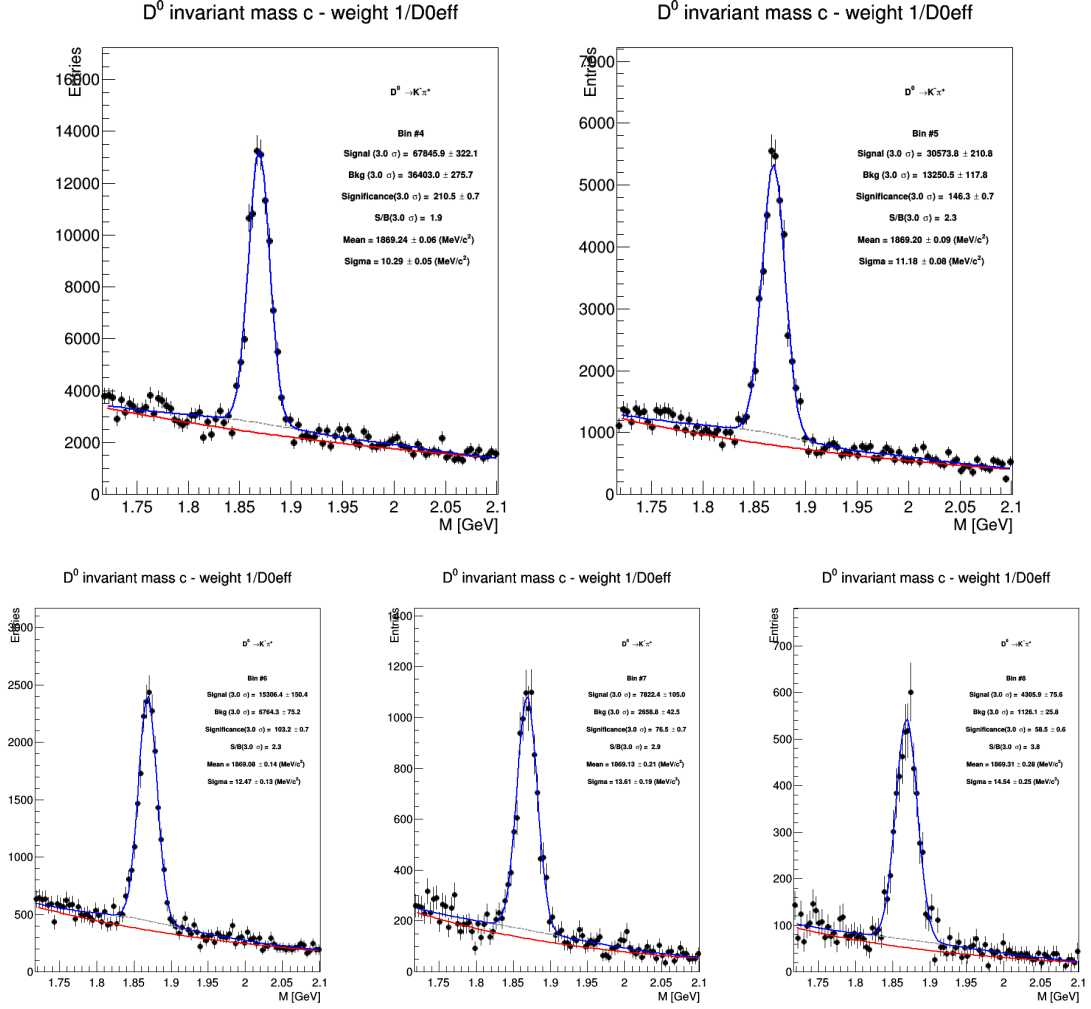


Figure 2: Invariant mass distributions of D^0 corrected with efficiency in different p_T regions. Top: $3 < p_T^D < 4$ GeV/ c (left), $4 < p_T^D < 5$ GeV/ c right), Bottom: $5 < p_T^D < 6$ GeV/ c (left), $6 < p_T^D < 7$ GeV/ c (middle), $7 < p_T^D < 8$ GeV/ c (right).

For the D^{*+} , 3 sets of cuts were compared (the 2016 p-Pb, 2016 pp and the standard D2H 2017 pp cuts). The best performance was obtained with 2016 p-Pb cuts in most of the p_T bin analysed. Indeed, despite the looser cuts applied from D2H allow to have higher signal, the p-Pb set of cuts assured a better S/B factor without loosing too much signal. This allows us to reduce fluctuations induced by the sideband subtraction, that is the limiting factor for the analysis performance. The same holds for the D^+ , but with the addition of cuts on the normalized decay length in xy plane and of the normalized difference between measured and expected daughter track impact parameters (topomatic cut).

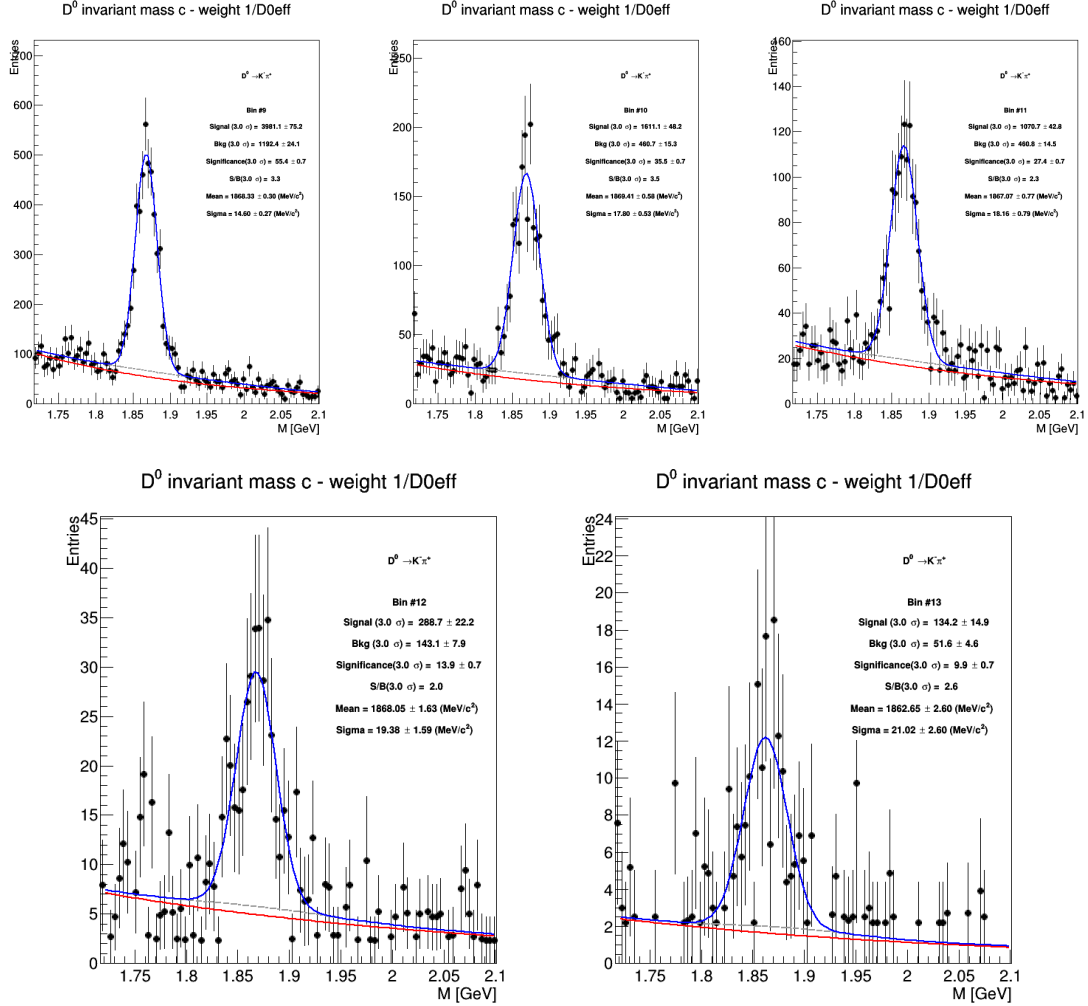


Figure 3: Invariant mass distributions of D^0 corrected with efficiency in different p_T regions. Top: $8 < p_T^D < 10$ GeV/ c , $10 < p_T^D < 12$ GeV/ c (middle), $12 < p_T^D < 16$ GeV/ c (right), Bottom: $12 < p_T^D < 16$ GeV/ c , $16 < p_T^D < 24$ GeV/ c .

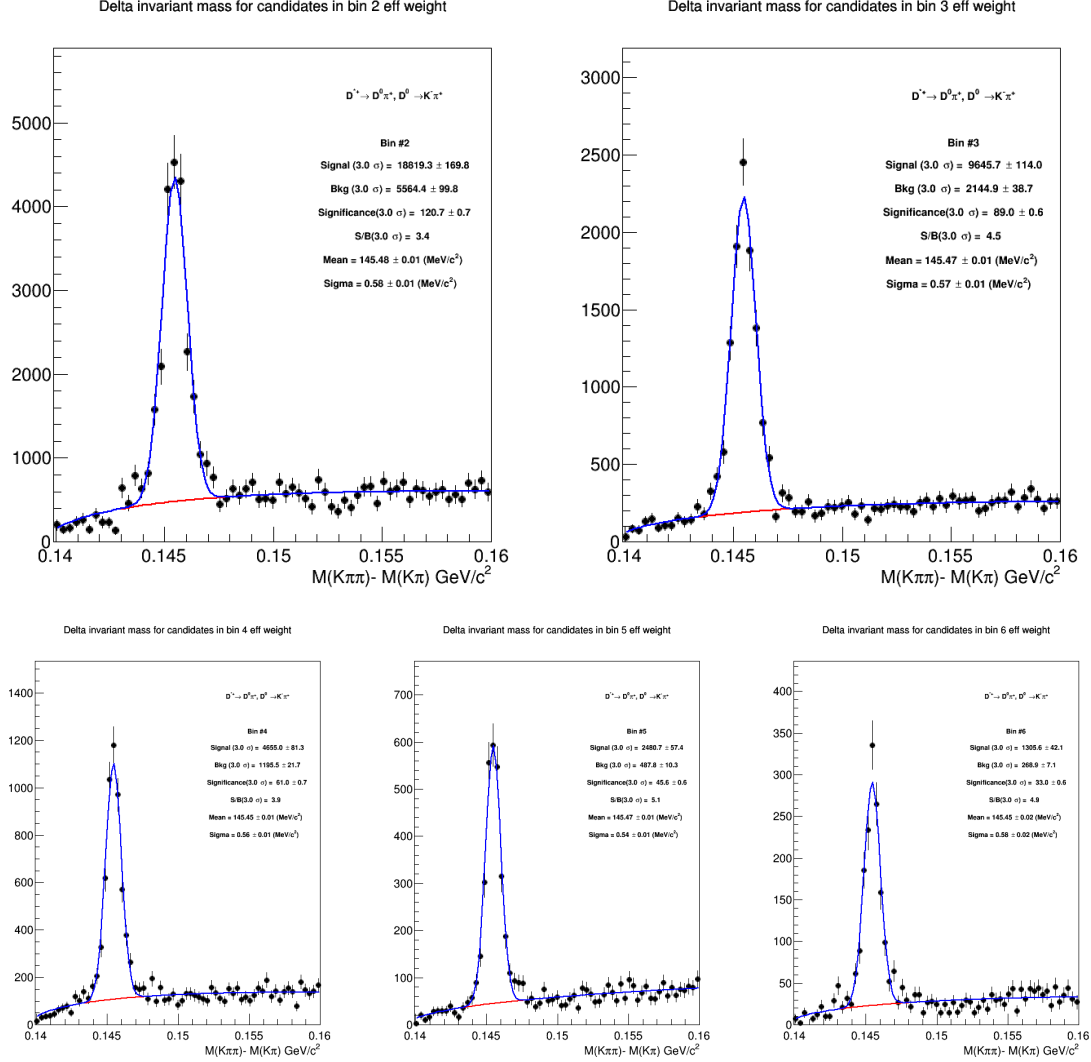


Figure 4: Invariant mass distributions of D^{*+} corrected with efficiency in different p_T regions. Top: $3 < p_T^D < 4 \text{ GeV}/c$ (left), $4 < p_T^D < 5 \text{ GeV}/c$ right), Bottom: $5 < p_T^D < 6 \text{ GeV}/c$ (left), $6 < p_T^D < 7 \text{ GeV}/c$ (middle), $7 < p_T^D < 8 \text{ GeV}/c$ (right).

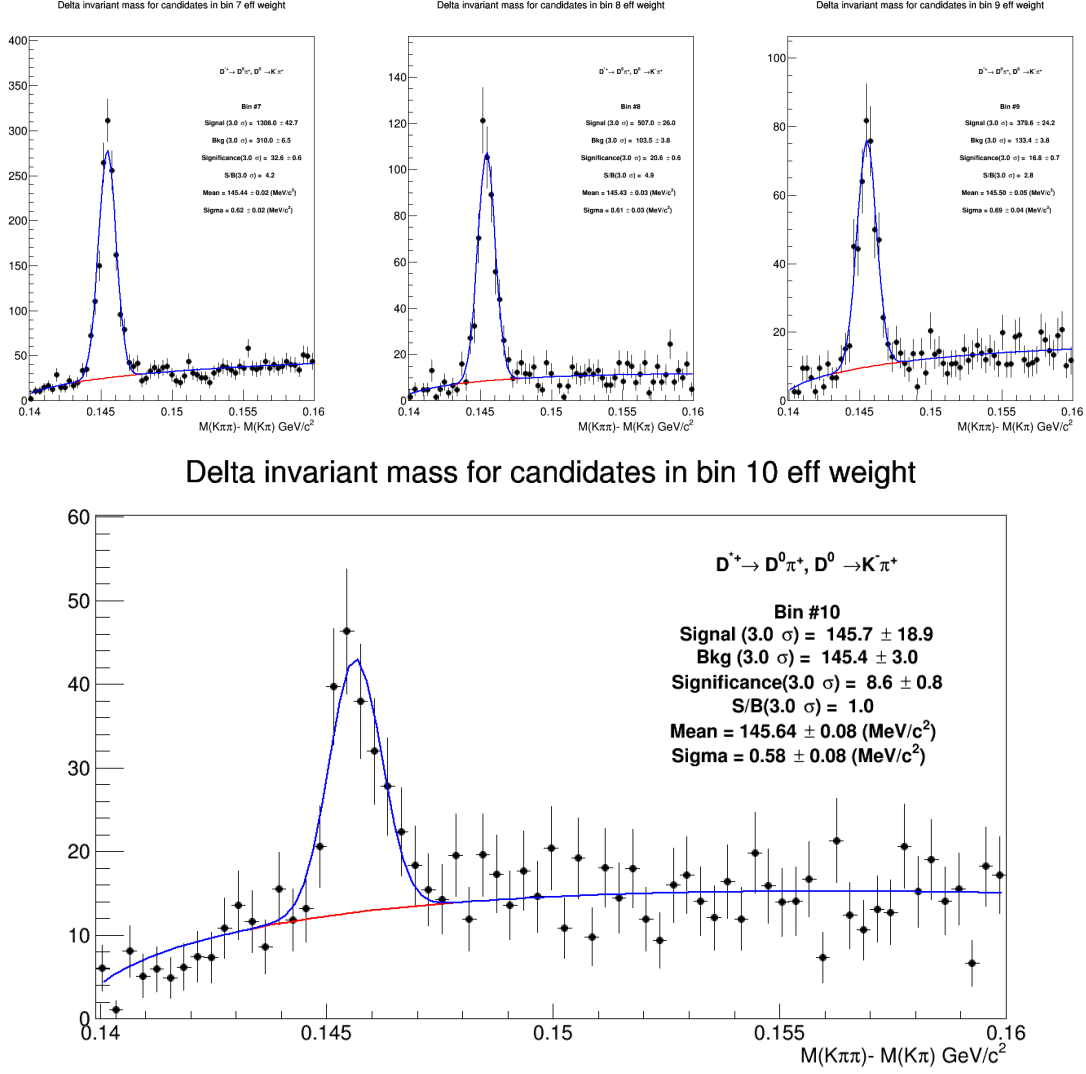


Figure 5: Invariant mass distributions of D^{*+} corrected with efficiency in different p_T regions. Top: $8 < p_T^D < 10$ GeV/c , $10 < p_T^D < 12$ GeV/c (middle), $12 < p_T^D < 16$ GeV/c (right) and Bottom: $16 < p_T^D < 24$ GeV/c .

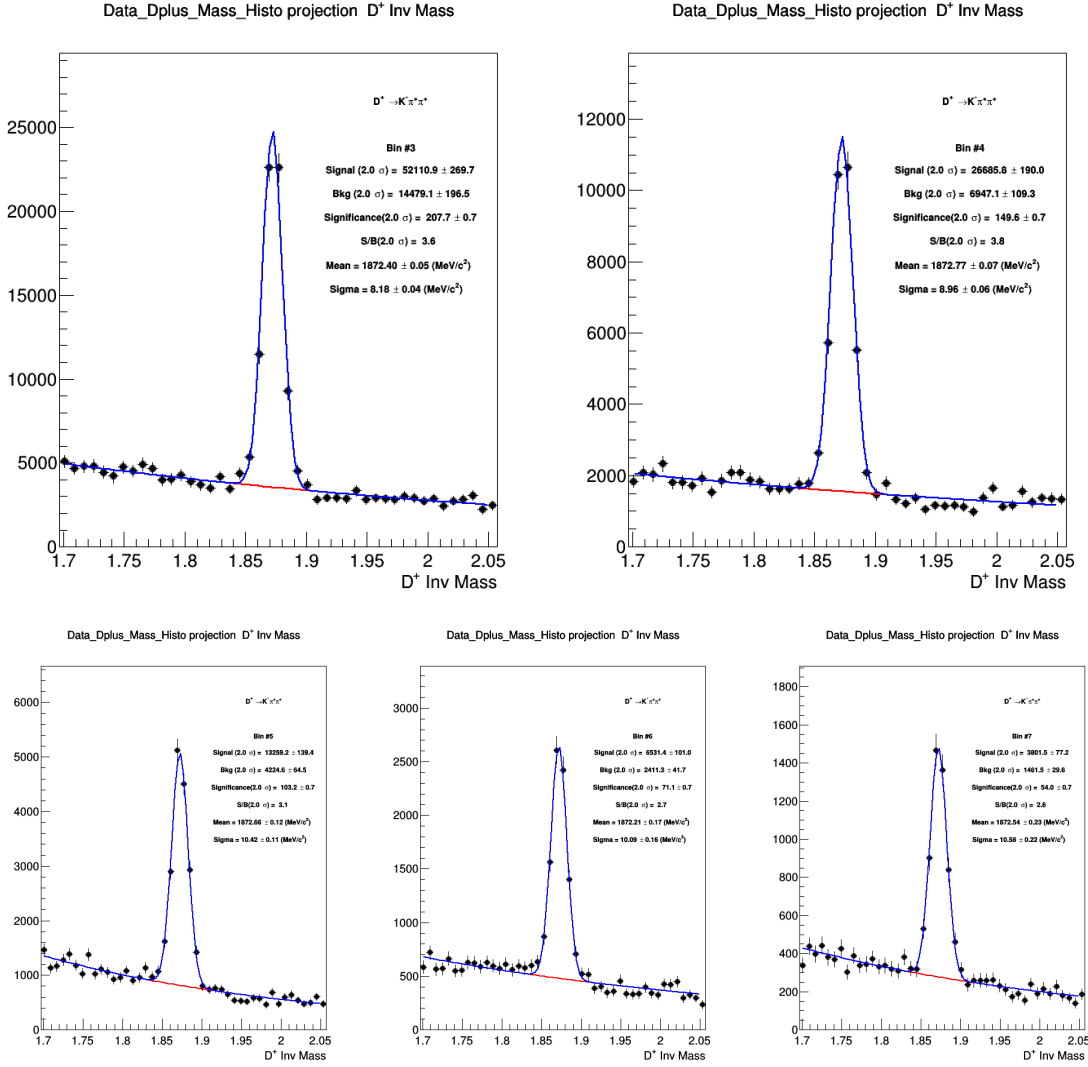


Figure 6: Invariant mass distribution of D^+ corrected with efficiency in different p_T regions. Top: $3 < p_T^D < 4$ GeV/c (left), $4 < p_T^D < 5$ GeV/c right), Bottom: $5 < p_T^D < 6$ GeV/c (left), $6 < p_T^D < 7$ GeV/c (middle), $7 < p_T^D < 8$ GeV/c (right);.

240 A particular cut optimization was instead performed for the D^0 meson. Twelve cut sets were tried, with
 241 the goal of increasing the S/B factor, in order to reduce fluctuations induced by the sideband subtraction as
 242 explained. In Figure 8 the D^0 -h correlation distributions are shown for the different cut sets, in exemplary
 243 kinematic regions (5 to 8 GeV/c), together with the bin-by-bin relative statistical uncertainty on the data
 244 points. The best cut set (option B, cyan colour) was defined starting from the standard cuts used for the
 245 p-Pb 2016 cross section analysis, with a tightened selection on the cosine of the pointing angle, and with
 246 the addition of a cut on the normalized decay length in xy plane (from 5 to 3 units with increasing p_T^D)
 247 and of a selection on the normalized difference between measured and expected daughter track impact
 248 parameters (topomatic cut) at 3 sigma.

249 3.1.1 Extension to very-low p_T of D mesons

250 Thanks to the higher statistic of the 2017 pp data sample, we tried to enlarge our correlation studies to
 251 very-low p_T of the trigger particle. Indeed, the Figure 9 shows the good performance on the invariant
 252 mass extraction for all the 3 D-mesons with $2 < p_T^D < 3$ GeV/c.

253 The extension of the analysis to this p_T interval is of high interest for the jet structure characterizion.
 254 Indeed, this study allow us to investigate a kinematic region in which the trigger particle has compatible
 255 or even lower momentum with respect to the associated particles. This give us the possibility to better
 256 understand the production processes. In fact, for example, at the Leading Order (LO) for $p_T(\text{trig}) \sim$
 257 $p_T(\text{ass})$ we don't expect any peak on the near-side region. A peak could arise only from Next-to-Leading-
 258 Order production process.

259 Despite the good statistics, it wasn't enough to perform the correlation analysis. Indeed, the correlation
 260 distribution peaks are very small, due to the small energy of the parton, resulting in few tracks being
 261 produced in the fragmentation oon top of the D meson. Hence, the correlation peaks were smoothened by
 262 the baseline fluctuations (of the same order of magnitude of the peak itself), especially on the away-side
 263 region, where indeed most of the fit failed.

264 3.2 Code used for the analysis

265 The code used for D meson-hadron correlation analysis is fully committed in AliPhysics. The anal-
 266 ysis classes can be found in `$ALICE_ROOT/PWGHF/correlationHF/`. The D meson specific classes
 267 where the aforementioned steps are carried out are `AliAnalysisTaskDStarCorrelations`, `AliAnalysis-`
 268 `TaskSED0Correlations` and `AliAnalysisTaskDplusCorrelations`. The classes which are common to the D
 269 meson specific analysis which includes the associated particle cuts and the correlation observables are `Ali-`
 270 `iHFAssociatedTrackCuts`, `AliHFCorrelator`, `AliHFOfflineCorrelator`, `AliReducedParticle` and `AliDhCor-`
 271 `relationExtraction`. Several additional classes and macros in the same folder deal with the correction
 272 steps.

273 3.3 Further details on corrections

274 3.3.1 Event Mixing

275 The event-mixing technique is used for correcting the raw correlation distribution for effects arising
 276 from the detector limited acceptance in rapidity and detector spatial inhomogeneities. The calculation
 277 of the Event Mixing correlation distribution is performed online. An event pool is created, where events
 278 preceding the one containing a D candidate are stored based on their properties (position of the vertex
 279 along the z axis and multiplicity). Each time a D meson candidate is found in an event, only the events
 280 contained in the same pool as the event under analysis is used to evaluate the correlations for the event
 281 mixing correction.

282 The multiplicity and z vertex position bins for the pools used in the p-Pb analysis (for both approaches)
 283 are the following:

- 284 – Multiplicity bins: $(0, 20); (20, 35); (35, +\infty)$
- 285 – Vertex z (cm) = $(-10, -2.5); (-2.5, 2.5); (2.5, 10)$

286 In an ideal case, the mixed event distribution is expected to have a constant flat distribution as function
 287 of $\Delta\phi$ and a triangular shaped distribution in $\Delta\eta$ deriving from the limited η acceptance of the detector.
 288 In case, instead, of detector inefficient regions, or holes, in the same angular position for D meson and
 289 associated tracks, these structures produce an excess of correlations at $\Delta\phi = 0$ in the $\Delta\phi$ distribution,
 290 plus possibly other structures depending on the relative position of the inefficient regions and on their
 291 number. The mixed-event distribution is used as a weight in each correlation bin, i.e, the corrected
 292 correlation distribution is calculated as follows:

$$\frac{dN^{corr}(\Delta\phi, \Delta\eta)}{d\Delta\phi d\Delta\eta} = \frac{\frac{dN^{SE}(\Delta\phi, \Delta\eta)}{d\Delta\phi d\Delta\eta}}{\frac{dN^{ME}(\Delta\phi, \Delta\eta)}{d\Delta\phi d\Delta\eta}} \frac{dN^{ME}(0, 0)}{d\Delta\phi d\Delta\eta} \quad (2)$$

293 In Eq.2, the last term stands for the average of the bins in the region $-0.2 < \Delta\eta < 0.2$, $-0.2 < \Delta\varphi < 0.2$
294 (multiple bins are used to minimize the effect of statistical fluctuations on the normalization of the mixed-
295 event plots). This kind of normalization, adopted in the analysis of hadron-hadron correlations, relies
296 on the fact that at $(\Delta\eta, \Delta\varphi) = (0, 0)$ the trigger and associated particle experience the same detector
297 effects. In the D meson case this is true only on average and not at very low p_T , since D mesons are
298 reconstructed from particles that can go in different detector region. However, $(\Delta\eta, \Delta\varphi) = (0, 0)$ is in
299 any case the region with maximum efficiency for the pairs (both correlated and uncorrelated). Thus the
300 same convention was adopted.

301 The mixed-event correlation distributions are built in both D meson signal and sideband regions. Both
302 are corrected with the relative distributions. An example of the mixed-event distributions, and of the
303 outcome of the mixed-event correction, is provided in Figures 10 and 11. The expected triangular shape
304 in $\Delta\eta$, for the mixed-event distributions, addresses the effect of the limited detector pseudo-rapidity
305 acceptance. Note that the mixed-event distribution is limited to the interval $|\Delta\eta| < 1$: the decision to
306 limit the mixed-event correction, and thus the whole analysis, to this range was taken in order to avoid
307 the so-called “wing effect”, i.e. the wing-like structures arising in the correlation distribution at large $\Delta\eta$
308 due to the limited filling of the correlation bins in that region.

Type	Production	Run list	nEvents
Monte-Carlo	LHC18a4a2_fast (c/b enriched) [GEANT3]	282343, 282342, 282341, 282340, 282314, 282313, 282312, 282309, 282307, 282306, 282305, 282304, 282303, 282302, 282247, 282230, 282229, 282227, 282224, 282206, 282189, 282147, 282146, 282127, 282126, 282125, 282123, 282122, 282120, 282119, 282118, 282099, 282098, 282078, 282051, 282050, 282031, 282025, 282021, 282016, 282008, 282367, 282366, 282365 = [44 runs]	23M
	LHC17l3b_fast (Minimum Bias sample) [GEANT3]	282008, 282016, 282021, 282025, 282031, 282050, 282051, 282078, 282098, 282099, 282118, 282119, 282120, 282122, 282123, 282125, 282126, 282127, 282146, 282147, 282189, 282206, 282224, 282227, 282229, 282230, 282247, 282302, 282303, 282304, 282305, 282306, 282307, 282309, 282312, 282313, 282314, 282340, 282341, 282342, 282365, 282366, 282367 = [44 runs]	23M
Data	LHC17p_pass1_FAST	282343, 282342, 282341, 282340, 282314, 282313, 282312, 282309, 282307, 282306, 282305, 282304, 282303, 282302, 282247, 282230, 282229, 282227, 282224, 282206, 282189, 282147, 282146, 282127, 282126, 282125, 282123, 282122, 282120, 282119, 282118, 282099, 282098, 282078, 282051, 282050, 282031, 282025, 282021, 282016, 282008 = [41 runs]	985M total
	LHC17p_pass1_CENT_woSDD	282343, 282342, 282341, 282340, 282314, 282313, 282312, 282309, 282307, 282306, 282305, 282304, 282303, 282302, 282247, 282230, 282229, 282227, 282224, 282206, 282189, 282147, 282146, 282127, 282126, 282125, 282123, 282122, 282120, 282119, 282118, 282099, 282098, 282078, 282051, 282050, 282031, 282030, 282025, 282021, 282016, 282008 = [42 runs]	
	LHC17q_pass1_FAST	282367, 282366, 282365 = [3 runs]	
	LHC17q_pass1_CENT_woSDD	282367, 282366, 282365 = [3 runs]	

Table 1: Data Set and Run list

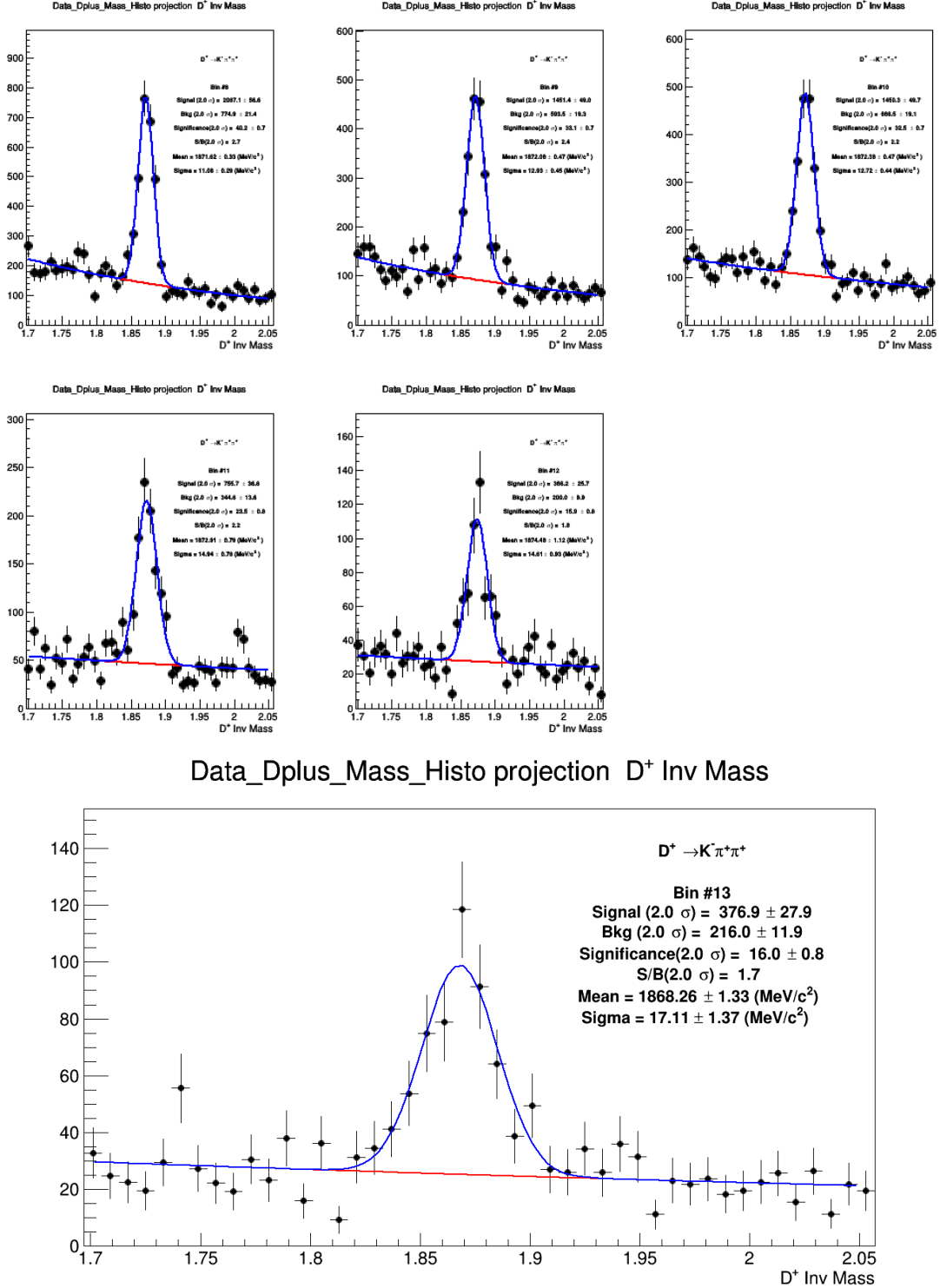


Figure 7: Invariant mass distribution of D^+ corrected with efficiency in different p_T regions. Top: $8 < p_T^D < 10$ GeV/c, $10 < p_T^D < 12$ GeV/c (middle), $12 < p_T^D < 16$ GeV/c (right) and Bottom: $16 < p_T^D < 24$ GeV/c .

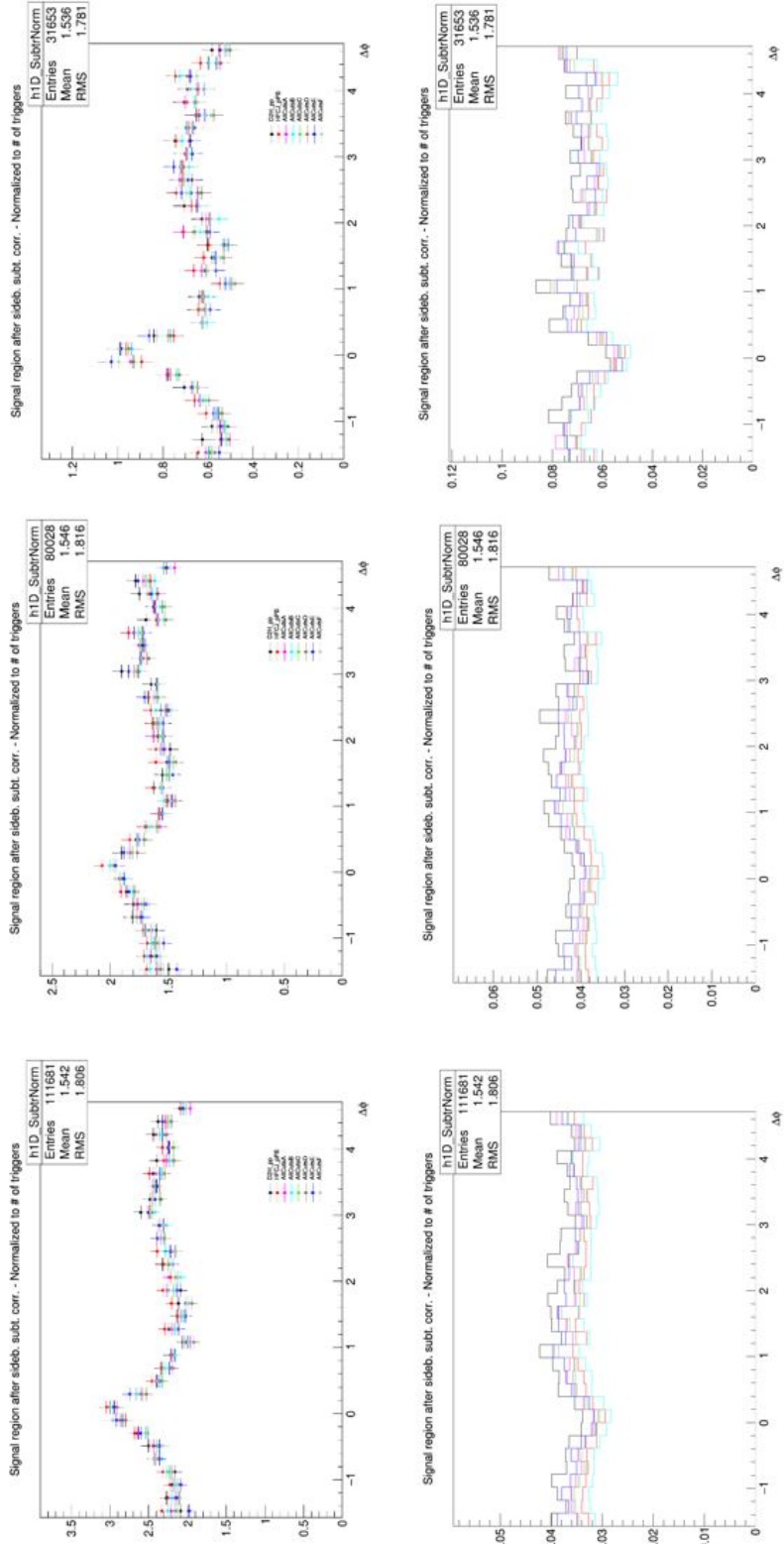


Figure 8: D^0 -h correlation distributions with different cut options (top) and point-by-point relative statistical uncertainty (bottom) for $5 < p_T^D < 8 \text{ GeV}/c$ for associated track $p_T > 0.3 \text{ GeV}/c$ (left), $0.3 < p_T < 1 \text{ GeV}/c$ (middle), $p_T > 1 \text{ GeV}/c$ (right)

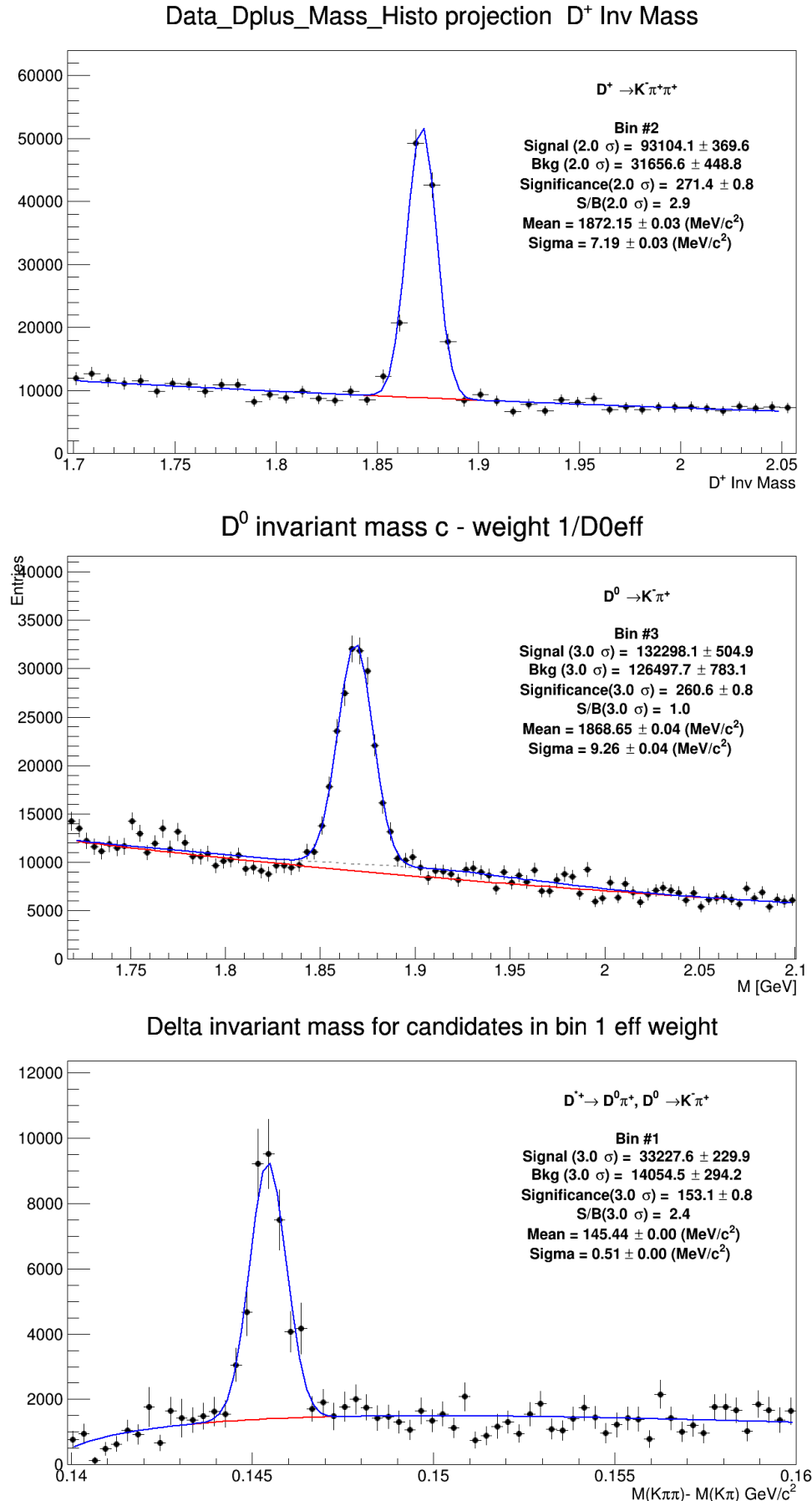


Figure 9: Invariant mass distribution of D⁺ (top), D⁰ (mid) and D^{*+} (bottom) corrected with efficiency for $2 < p_T^D < 3$.

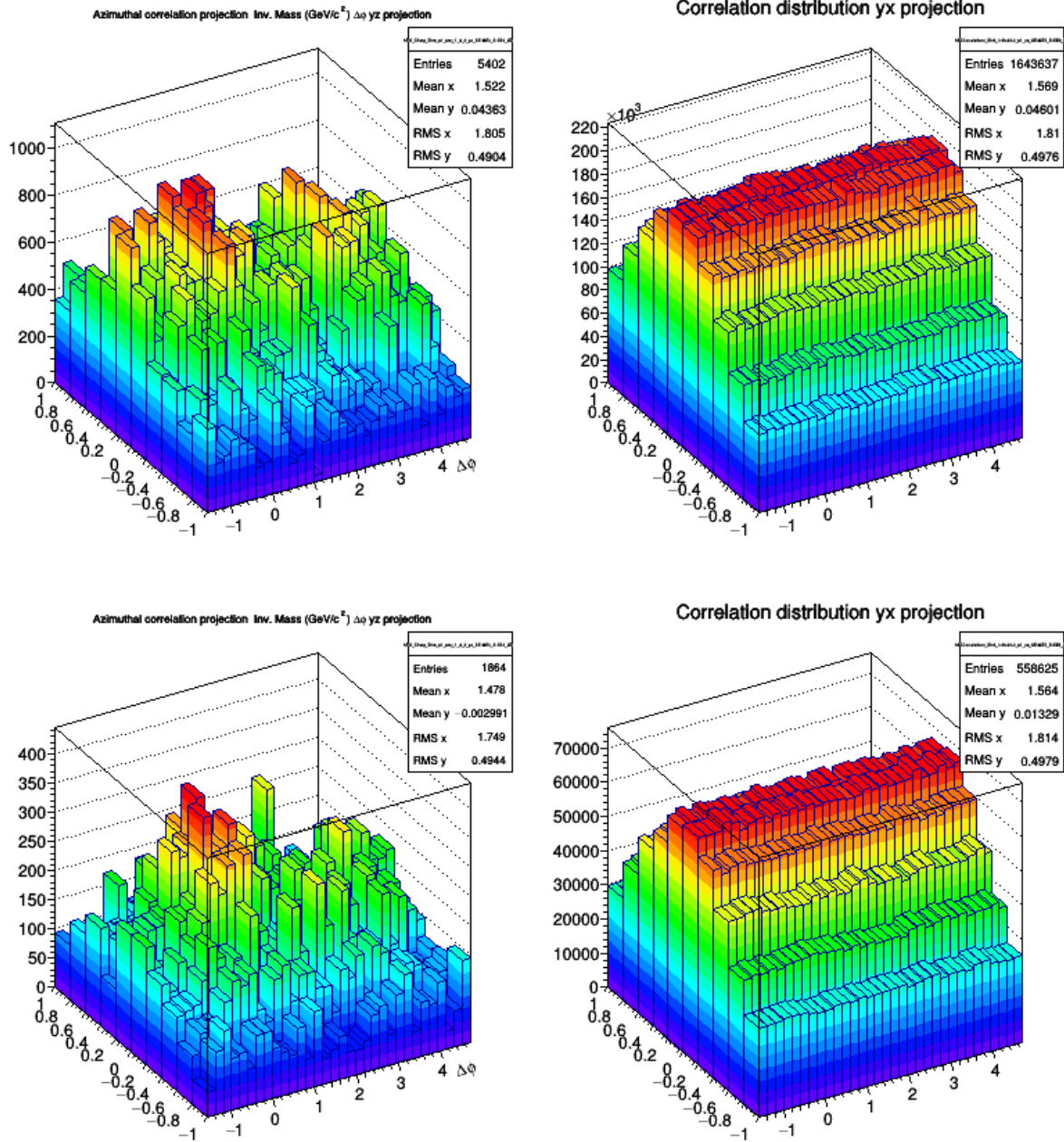


Figure 10: D^{*+} meson ($\Delta\phi$, $\Delta\eta$) correlation for in the signal region (top row) and sidebands (bottom row) from pool1, for Single Event (left) and Mixed Event analysis (center) for high p_T : $3 < p_T < 5$ GeV/c with associated $p_T > 0.3$ GeV/c. The right column shows the SE/ME corrected distributions.

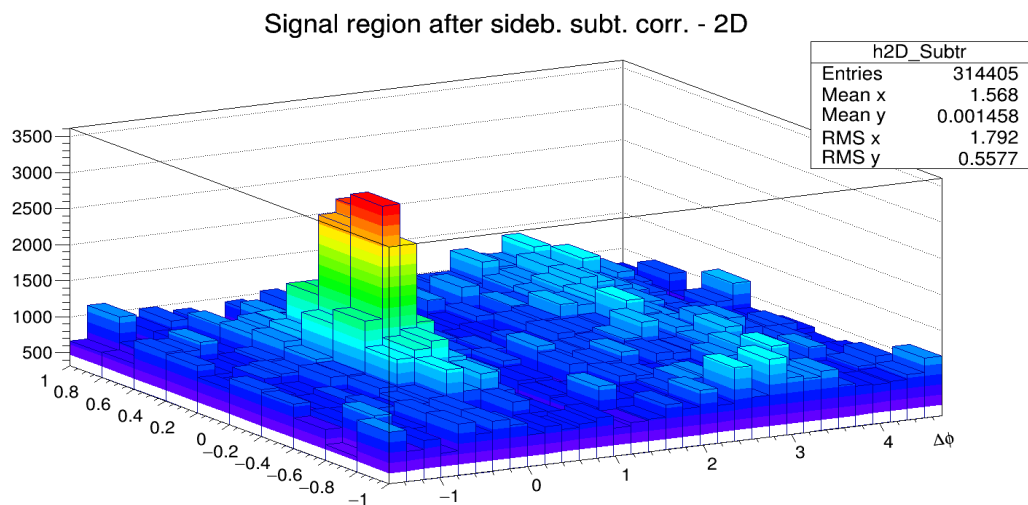


Figure 11: $(\Delta\phi, \Delta\eta)$ correlation distribution of D^{*+} -h with $8 < p_T < 16$ GeV/c and associated track p_T Threshold: $p_T > 0.3$ GeV/c, after the mixed-event correction.

309 **3.3.2 Tracking and D-meson trigger efficiency**

310 **(i) Tracking efficiency** - The tracking efficiency was calculated by obtaining the ratio between the yield
311 at the reconstructed level and generated level, for a defined “type” of particles (in our case non-identified
312 particles) and it is estimated differentially in p_T , η , and z_{vtx} of the charged particles.

313
314 Tracking efficiency maps were produced as TH3D histograms (p_T , η , z_{vtx}) obtained from MC analy-
315 sis on the minimum-bias samples LHC17l3b_fast and LHC17l3b_cent_woSDD anchored to LHC17p,q
316 data samples, considering only primary pions, kaons, protons, electrons and muons, and applying at
317 reconstructed level the track selections (summarized in Table 2). These efficiency maps were used in
318 the analysis tasks to extract single track efficiencies; each correlation pairs found in the data analysis
319 was inserted in correlation plots with a weight of **1/efficiency value**. The 1D (p_T dependence) tracking
320 efficiency for all the five species as well as the tracking efficiency specie by specie are shown in Fig. 12.

³²¹ Details of cuts at event level and particle/track selection at different steps are listed in Table 2 .

MC Generated	
Stages	Cuts
1. MC Part with Generated Cuts	After Event Selection Charge PDG Code Physical Primary Kinematics Cuts $-0.8 < \eta < 0.8$ $p_T > 0.3$ (GeV/c)
2. MC Part with Kine Cuts	
MC Reconstructed	
4. Reco tracks	After Event Selection Physical Primary Kinematics Cuts $-0.8 < \eta < 0.8$ $p_T > 0.3$ (GeV/c) Quality Cuts SetRequireSigmaToVertex(kFALSE) SetDCAToVertex2D(kFALSE) SetMinNCrossedRowsTPC(70) SetMinRatioCrossedRowsOverFindableClustersTPC(0.8) SetMinNClustersITS(2) SetMaxChi2PerClusterTPC(4) SetMaxDCAToVertexZ(1) SetMaxDCAToVertexXY(1) SetRequireTPCRefit(TRUE) SetRequireITSRefit(FALSE) Same as step 6
5. Reco tracks with Kine Cuts	
6. MC true with Quality Cuts	
7. Reco tracks with Quality Cuts	

Table 2: The list of event and particle/track selection cuts used in the estimation of single track efficiency

³²²

³²³ **(ii) D meson efficiency** - Due to limited statistics, the correlation analysis is performed in quite wide p_T bins and in each of them the reconstruction and selection efficiency of D mesons is not flat, in particular in the lower p_T region. We correct for the p_T dependence of the trigger efficiency within each p_T -bin.

³²⁶ This correction is applied online, by using a map of D meson efficiency as a function of p_T and event ³²⁷ multiplicity (in terms of SPD tracklets in $|\eta| < 1$) extracted from the enriched Monte Carlo sample ³²⁸ LHC18a4a2_fast. The η dependence was neglected due to the statistics of the available Monte Carlo ³²⁹ sample, which rule out the possibility of performing a 3D study.

³³⁰ To properly count the number of trigger particles used to normalize the correlation distributions, N_{trig} , ³³¹ each D meson is weighted with the inverse of its efficiency in the invariant mass distribution. The main ³³² role of the correction for the D meson efficiency is to account for the p_T dependence of the correlation ³³³ distribution within a given D meson p_T interval. Indeed, only the p_T shape of the D meson efficiency ³³⁴ within the correlation p_T^{trig} ranges is relevant while the average value in the p_T range is simplified due to ³³⁵ the normalization of the correlation distribution to the number of trigger particles.

³³⁶ Efficiency plots for D^0 , D^+ and D^{*+} mesons are shown in Figs. 13 and 14, for prompt and feed-down D
³³⁷ mesons, respectively.

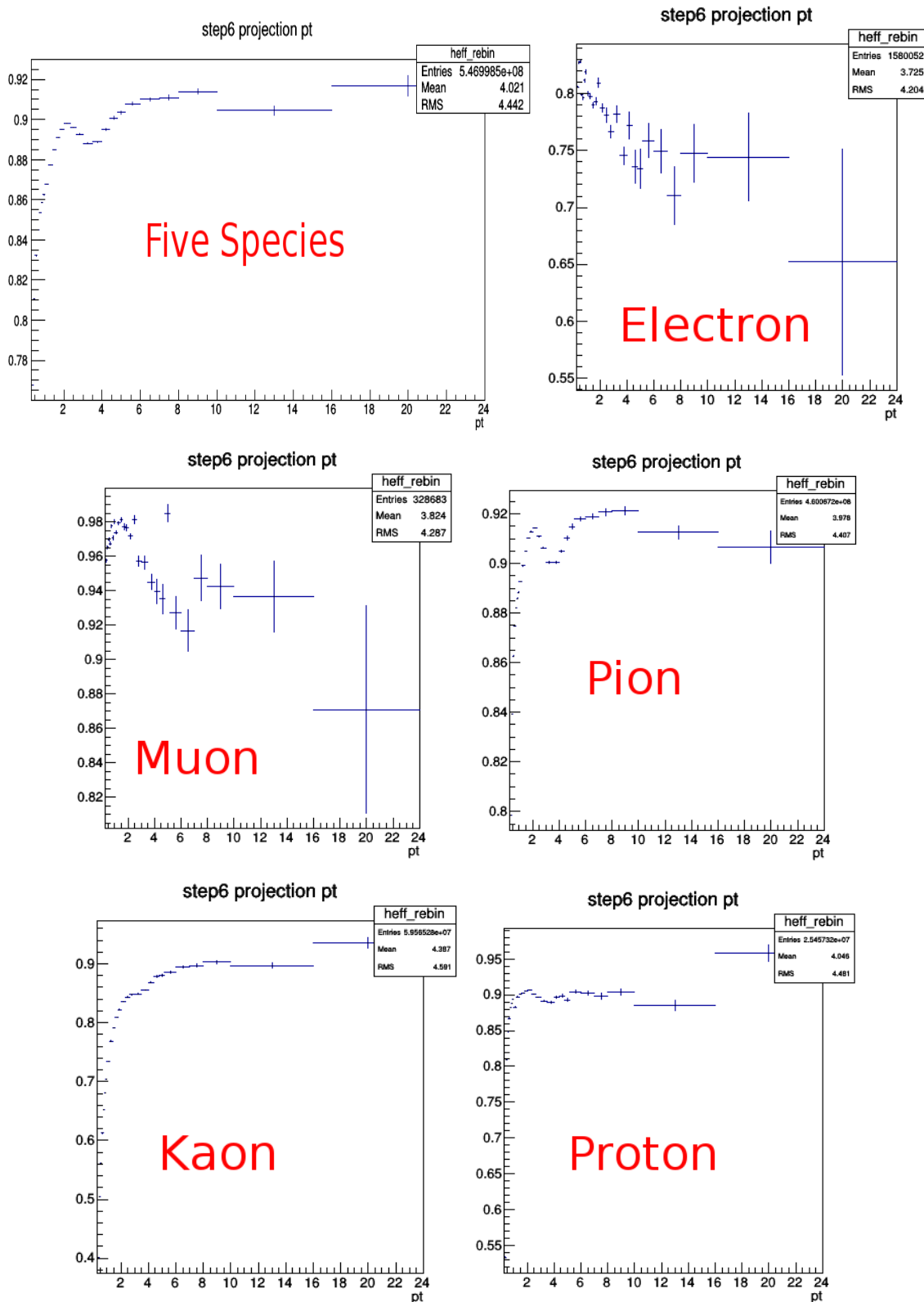


Figure 12: 1D (vs p_T) tracking efficiency map for standard track selection, evaluated for five species (electron, muon, pion, kaon and proton) and also different species using data sample LHC17I3b_fast.

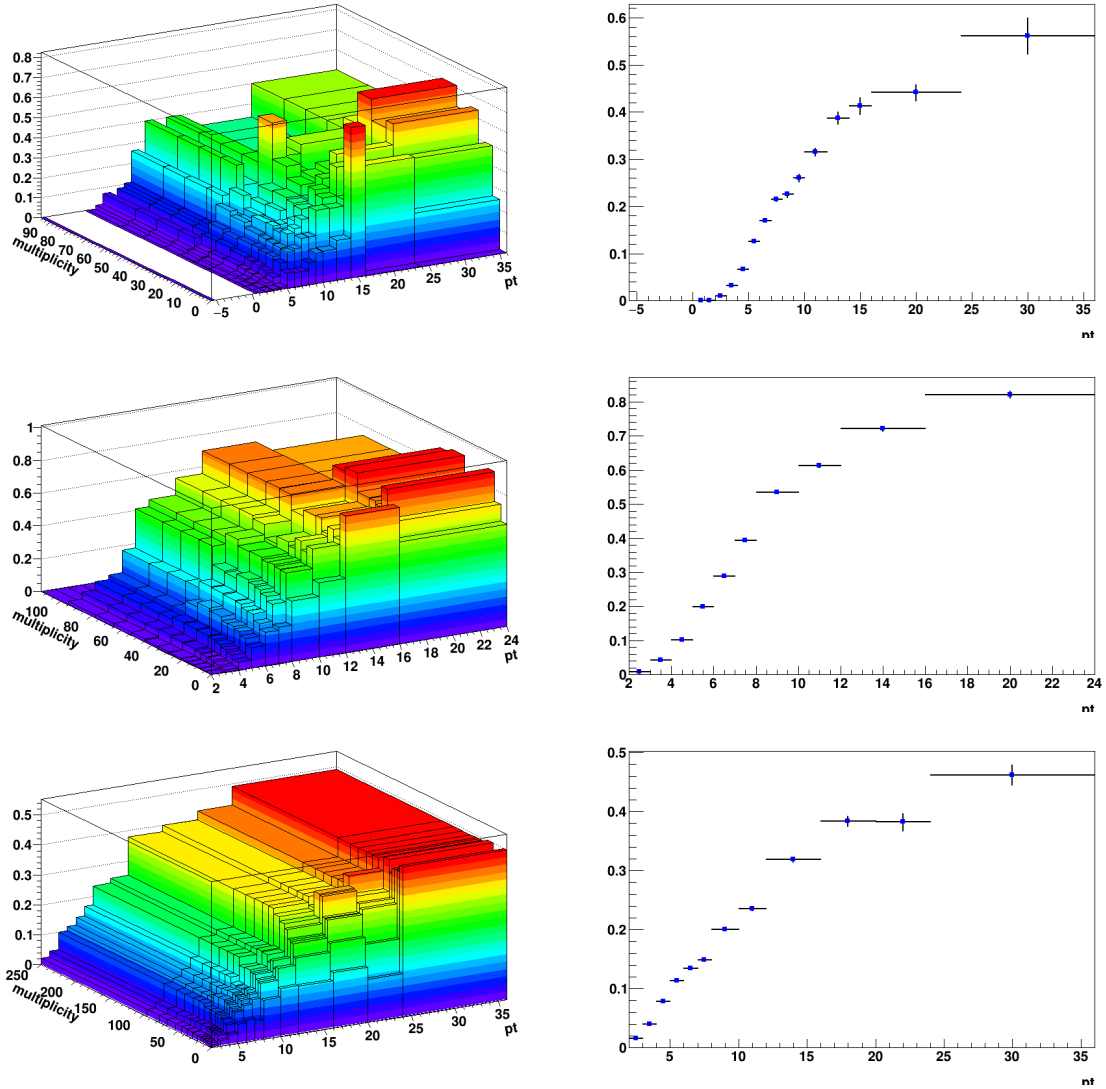


Figure 13: Top panel: (p_T , multiplicity) dependence (left) and p_T dependence (right) of prompt D^+ meson efficiency. Mid panel: (p_T , multiplicity) dependence (left) and p_T dependence (right) of prompt D^{*+} meson efficiency. Bottom panel: (p_T , multiplicity) dependence (left) and p_T dependence (right) of prompt D^0 meson efficiency.

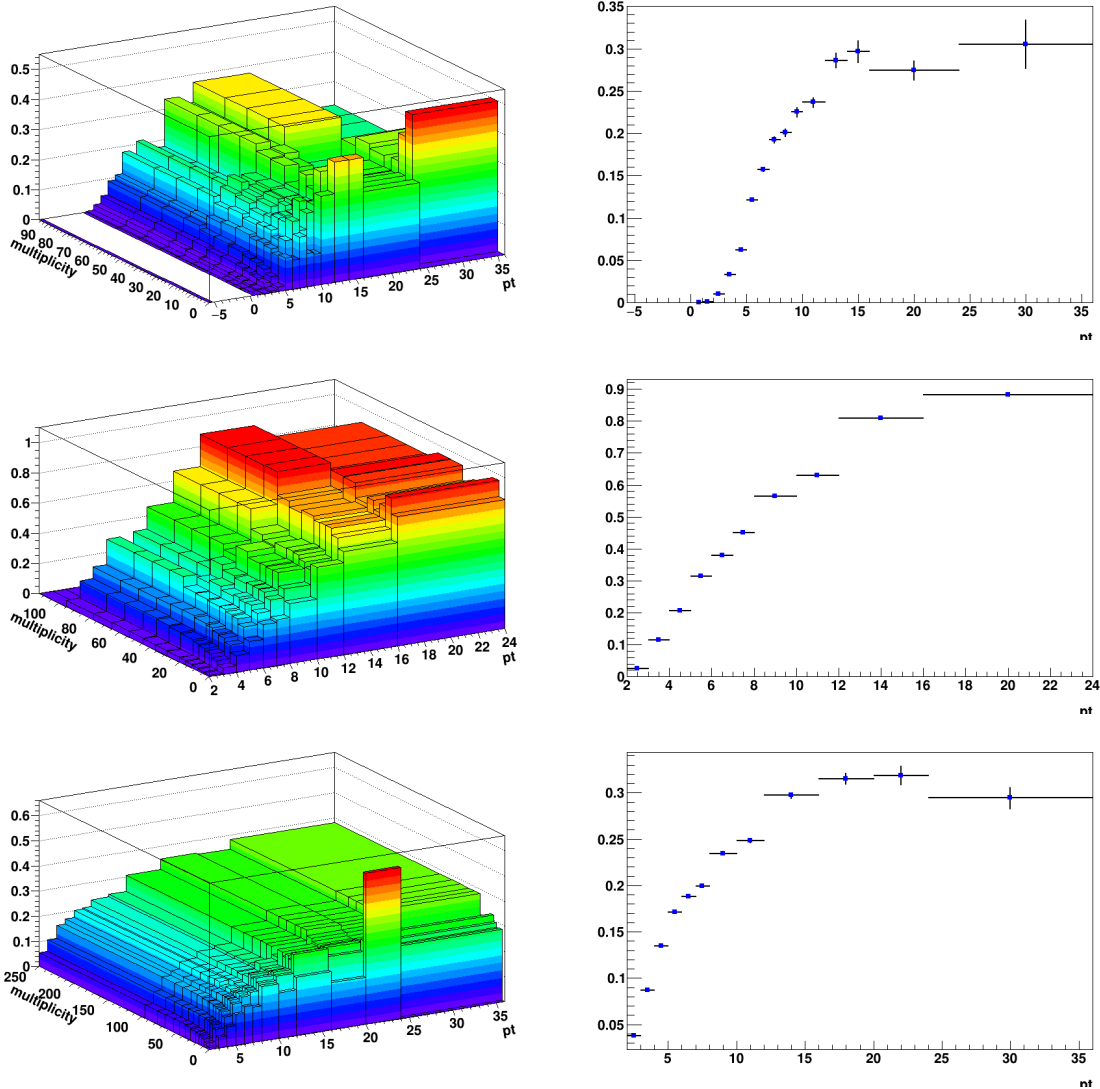


Figure 14: Top panel: (p_T , multiplicity) dependence (left) and p_T dependence (right) of feed-down D⁺ meson efficiency. Mid panel: (p_T , multiplicity) dependence (left) and p_T dependence (right) of feed-down D^{*+} meson efficiency. Bottom panel: (p_T , multiplicity) dependence (left) and p_T dependence (right) of feed-down D⁰ meson efficiency.

338 **3.3.3 Correction for bias on B to D decay topologies**

339 To verify the consistency of the analysis chain and of the corrections applied to the correlation distributions extracted from data, a Monte Carlo closure test was setup and tried on the D^0 - h analysis.

340 On the Monte Carlo enriched with charm and beauty quarks (LHC18a4a2_fast, with GEANT3), the
 341 correlation analysis was performed both at kinematic level and at reconstructed level. At kinematic
 342 level, only acceptance cuts were applied on the D mesons and the associated particles, using the Monte
 343 Carlo information for the identification of the D mesons and the hadrons in the event and rejecting the
 344 non-primary particles. At reconstructed level, the analysis was performed as if it were executed on data,
 345 applying the event selection, the acceptance cuts for D mesons and the associated particles, selecting the
 346 D meson candidates with filtering cuts on their daughters, topological cuts and PID selection, and then
 347 keeping only the true D mesons by matching with the Monte Carlo truth; non-primary particles were
 348 rejected by means of the DCA selection. Event mixing correction was applied both at reconstructed and
 349 at kinematic level, where it takes into account just the effects of the acceptance cuts. In addition, at
 350 reconstructed level, the efficiency corrections for D mesons and associated tracks were also applied.

351 The consistency check was performed to verify whether, after having applied all the corrections to the
 352 azimuthal correlation plots at reconstructed level, the results were compatible with the ones at kinematic
 353 level. Hence, the ratios of fully corrected reconstructed plots over kinematic plots were evaluated in all
 354 the D^0 p_T bins and for the various p_T thresholds for the associated tracks, separating the contributions
 355 for the different origins of particles and triggers. The ratios, shown in Figure 15 for exemplary kinematic
 356 regions (covering anyway the full span of the measurement), denote a good compatibility with 1, within
 357 the uncertainties, of the average reconstructed over generated ratios, in particular for the all D -non HF
 358 track case (blue curves), apart from small downward deviations at low p_T , which will be cured with a 2-
 359 3% asymmetric systematic uncertainty, as also previously done in the pp 2010 and p-Pnb 2013 analyses.

360 The major exceptions to the previous conclusion are clearly the structures in the near side region for the
 361 beauty origin case. It was verified that these structures are induced by our topological selection for the D
 362 mesons. Indeed, in cases in which the D meson triggers come from B hadrons, applying the topological
 363 cuts (especially the cosine of the pointing angle) tends to favour cases with a small angular opening
 364 between the products of the B hadron decay (i.e. the D meson trigger itself and other particles), with
 365 respect to cases where the B decay particles are less collinear.

366 In the Monte Carlo closure test, this situation is reflected in the correlation distributions at reconstructed
 367 level, where the topological selection is applied, while it does not occur at kinematic level. Hence, in
 368 the reconstructed/kinematic ratio, the distribution would show an excess for $\Delta\varphi = 0$ (due to the favoured
 369 decays with small opening angle), which is then compensated by a depletion for larger values of $\Delta\varphi = 0$
 370 (corresponding to B decays with larger angles, which are disfavoured). These structures are prominent at
 371 low D^0 p_T , where the topological cuts are tighter, and tend to disappear at higher p_T , where the selections
 372 are released. They are also larger in the higher associated track p_T ranges, where the fraction of B -hadron
 373 decay tracks dominate the overall correlation distributions.

374 The data correlation distribution need to be corrected for this bias, and in particular for the enhancement
 375 of b -origin correlation pairs at the centre of the near side region, which would influence the near-side
 376 peak features. In order to do this, the amount of the b -origin excess is evaluated from the Reco/Kine
 377 ratio, by considering the b - D^0 -all tracks case (dark green points). The excess at Reco level (affecting
 378 data) is quantified as a $\Delta\varphi$ modulation **modul** for the five points an each side of the $\Delta\varphi = 0$ value (or,
 379 equivalently, on the first five points of the reflected distributions, which start from $\Delta\varphi = 0$). This is
 380 done separately in each p_T range. Then, the correction is done by applying this modulation to the data
 381 correlation distributions, but taking into account that only the correlation entries from $B \rightarrow D$ are affected,
 382 while the $c \rightarrow D$ correlations need to be left unaltered. In particular, it has to be considered that:

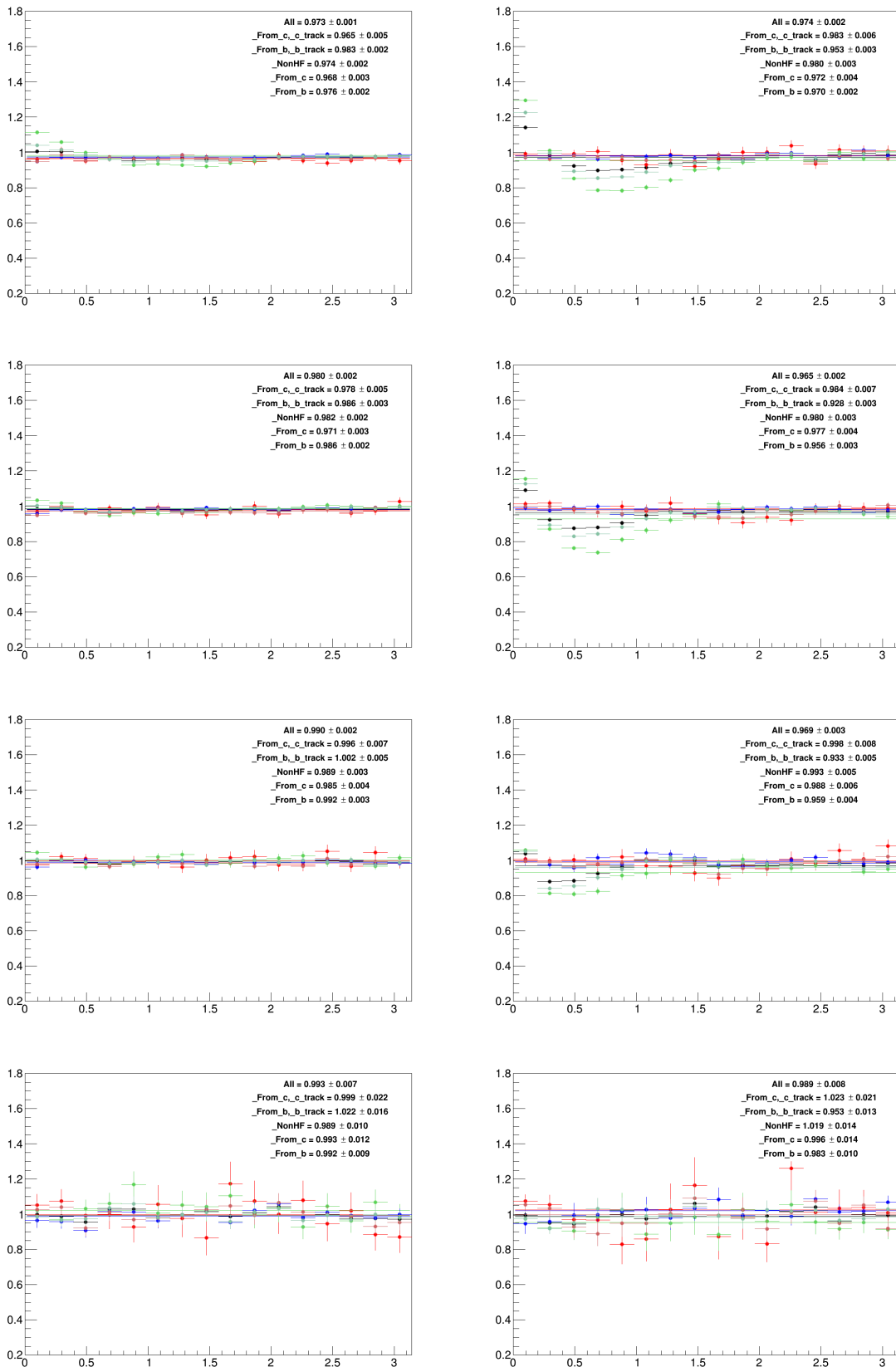


Figure 15: Ratios of fully corrected azimuthal correlation plots at reconstructed level over azimuthal correlation plots at kinematic level, in the two D^0 p_T bins, for the different associated p_T ranges. Black points: All D^0 -all hadrons, normalized by all D^0 triggers; light red points: D^0 from c-hadrons from c, normalized by c- D^0 triggers; dark red points: D^0 from c-all hadrons, normalized by c- D^0 triggers; light green points: D^0 from b-hadrons from b, normalized by b- D^0 triggers; dark green points: D^0 from b-all hadrons, normalized by b- D^0 triggers; blue points: All D^0 -hadrons from light quarks, normalized by all D^0 triggers. The panels show the ranges: $3 < p_T(D) < 5 \text{ GeV}/c$, $0.3 < p_T(\text{assoc}) < 1 \text{ GeV}/c$ (1st row-left); $3 < p_T(D) < 5 \text{ GeV}/c$, $p_T(\text{assoc}) > 1 \text{ GeV}/c$ (1st row-right); $5 < p_T(D) < 8 \text{ GeV}/c$, $0.3 < p_T(\text{assoc}) < 1 \text{ GeV}/c$ (2nd row-left); $5 < p_T(D) < 8 \text{ GeV}/c$, $p_T(\text{assoc}) > 1 \text{ GeV}/c$ (2nd row-right); $8 < p_T(D) < 16 \text{ GeV}/c$, $0.3 < p_T(\text{assoc}) < 1 \text{ GeV}/c$ (3rd row-left), $8 < p_T(D) < 16 \text{ GeV}/c$, $p_T(\text{assoc}) > 1 \text{ GeV}/c$ (3rd row-right); $16 < p_T(D) < 24 \text{ GeV}/c$, $0.3 < p_T(\text{assoc}) < 1 \text{ GeV}/c$ (4th row-left), $16 < p_T(D) < 24 \text{ GeV}/c$, $p_T(\text{assoc}) > 1 \text{ GeV}/c$ (4th row-right).

- On data, the $B \rightarrow D$ correlation pairs are only a fraction ($1 - f_{\text{prompt}}$) of the total.
- The amplitude of $B \rightarrow D|_{\text{amplit}}$ correlation pattern is different (greater) than the amplitude of the $c \rightarrow D|_{\text{amplit}}$ correlation pattern:

Thus, the following equation is applied to get the corrected $C(\Delta\phi)_{\text{corr}}$ data points starting from the raw ones, $C(\Delta\phi)_{\text{raw}}$:

$$C(\Delta\phi)_{\text{corr}} = C(\Delta\phi)_{\text{raw}} \cdot \left[\frac{c \rightarrow D|_{\text{amplit}}}{(B + c) \rightarrow D|_{\text{amplit}}} \cdot f_{\text{prompt}} + \frac{B \rightarrow D|_{\text{amplit}}}{(B + c) \rightarrow D|_{\text{amplit}}} \cdot (1 - f_{\text{prompt}}) \cdot \frac{1}{\text{modul}} \right] \quad (3)$$

where $(B + c) \rightarrow D|_{\text{amplit}} = c \rightarrow D|_{\text{amplit}} \cdot f_{\text{prompt}} + B \rightarrow D|_{\text{amplit}} \cdot (1 - f_{\text{prompt}})$, and where the two amplitudes are evaluated from the Monte Carlo distributions at reconstructed level (so, including the bias), and f_{prompt} with the procedure described in 3.3.5. Applying the **modul** factor to the beauty part of the data correlation distributions brings its value back to the generated level case, effectively removing the bias. The effect of the correction is a shift of the data points in the near-side region (in general, downward in the first and second points, the upward in the others). The maximum value of the shift is of about 5%, at the centre of the near-side peak, for the lowest D-meson p_T range ($3 < p_T < 5 \text{ GeV}/c$) and the highest associated track p_T range ($p_T > 3 \text{ GeV}/c$). The typical values are instead of a couple of percentage points. The correction is zero in the highest D-meson p_T range. To take into account for possible inaccuracies in the definition of the modulations, or in their rescaling, a systematic uncertainty is applied on the corrected data points, with value $|C(\Delta\phi)_{\text{corr}} - C(\Delta\phi)_{\text{raw}}| / \sqrt{12}$, on each side of the data points affected by the bias (symmetric uncertainty).

401 **3.3.4 Secondary track contamination**

402 The secondary tracks inside the associated track sample, due to interaction of primary track with the de-
 403 tector material or to decays of strange hadrons, are mostly removed by the DCA cuts applied during the
 404 cut selection phase ($DCA(xy) < 1 \text{ cm}$, $DCA(z) < 1 \text{ cm}$). Anyway, a small fraction of secondary tracks
 405 survives this cut, and the data correlation distributions have to be corrected for this residual contamina-
 406 tion. The fraction of surviving secondary tracks is evaluated via a study on the LHC18a4a2 fast sample,
 407 by counting the number of tracks accepted by the selection whose corresponding generated-level track
 408 doesn't satisfy the `IsPhysicalPrimary()` call, and dividing this number by the total number of accepted
 409 tracks. The outcome of the check is reported in Figure 16. As it's visible, no more than about 4.5%
 410 secondary tracks pass the selection (6% in the lowest associated p_T range). Moreover, the fraction of
 411 residual secondary tracks is rather flattish along the $\Delta\phi$ axis, as shown, for exemplary p_T regions, in
 412 Figure 17, where the inhomogeneities are generally not larger than about 1%. Anyway, to take into ac-
 413 count these modulations, which vary from bin to bin, the purity correction was performed differentially
 414 though the azimuthal axis (i.e. applied bin-per-bin on the azimuthal correlation distributions). In addi-
 415 tion, this was important to consider since though these structures are small, they could be amplified after
 416 the subtraction of the baseline, when going to the yield evaluation.

417 In particular, three approaches were tried, by multiplying the data correlation distribution in each kine-
 418 matic range by:

- 419 – the MC primary/inclusive histogram (blue histogram in Fig. 17)
- 420 – a polynomial fit applied to the MC primary/inclusive histogram (red curve in Fig. 17)
- 421 – a moving average, considering 3 points, of the MC primary/inclusive histogram (red histogram in
 422 Fig. 17)

423 Each approach has pros and cons, since directly using the primary/inclusive histogram gives a correction
 424 strongly dependent on the statistical fluctuations, while using the fit or the moving average smoothen the
 425 fluctuation, but also the structures with a physical origin (and the fit misses a periodicity condition). For
 426 this reason, a comparison of the outcome of the correction after applying either of the approaches (and
 427 the old 'flat' correction approach) was performed, which gave full compatibility (within less than 1%) of
 428 the correlation distributions corrected with either approach. The moving average approach was chosen
 429 as standard correction procedure.

430 It was also verified with the same Monte Carlo study that applying the DCA selection rejects less than 1%
 431 primary tracks (tagged as false positives) from the associated track sample, and less than 1% of heavy-
 432 flavour originated tracks, again with a flattish azimuthal distribution, inducing hence a fully negligible bias
 433 on the data correlation distributions. This is shown in Figure 18. This was also verified for specific
 434 charm-origin and beauty-origin tracks, due to their larger DCA with respect to primary tracks from light
 435 quarks. In this case, the fraction of rejected charm and beauty tracks stays below 1% in all the kinematic
 436 ranges apart from the associated track p_T regions 0.3-1 and $> 0.3 \text{ GeV}/c$, where the rejection can be
 437 as high as 2%. In these kinematic ranges, though, the data correlation distributions are dominated by
 438 non-heavy-flavour tracks, as it was verified from the simulations, hence the overall bias is still contained
 439 below 1%, thus negligible.

440 These studies were performed on an enriched Monte Carlo sample, which could not fully reproduce
 441 the relative abundances of the species. Anyway, for events with a reconstructed D-meson, this bias is
 442 expected to be minor, and only these events are used in the data analysis. In any case, the percentages
 443 obtained from the study were found to be consistent within 1%.

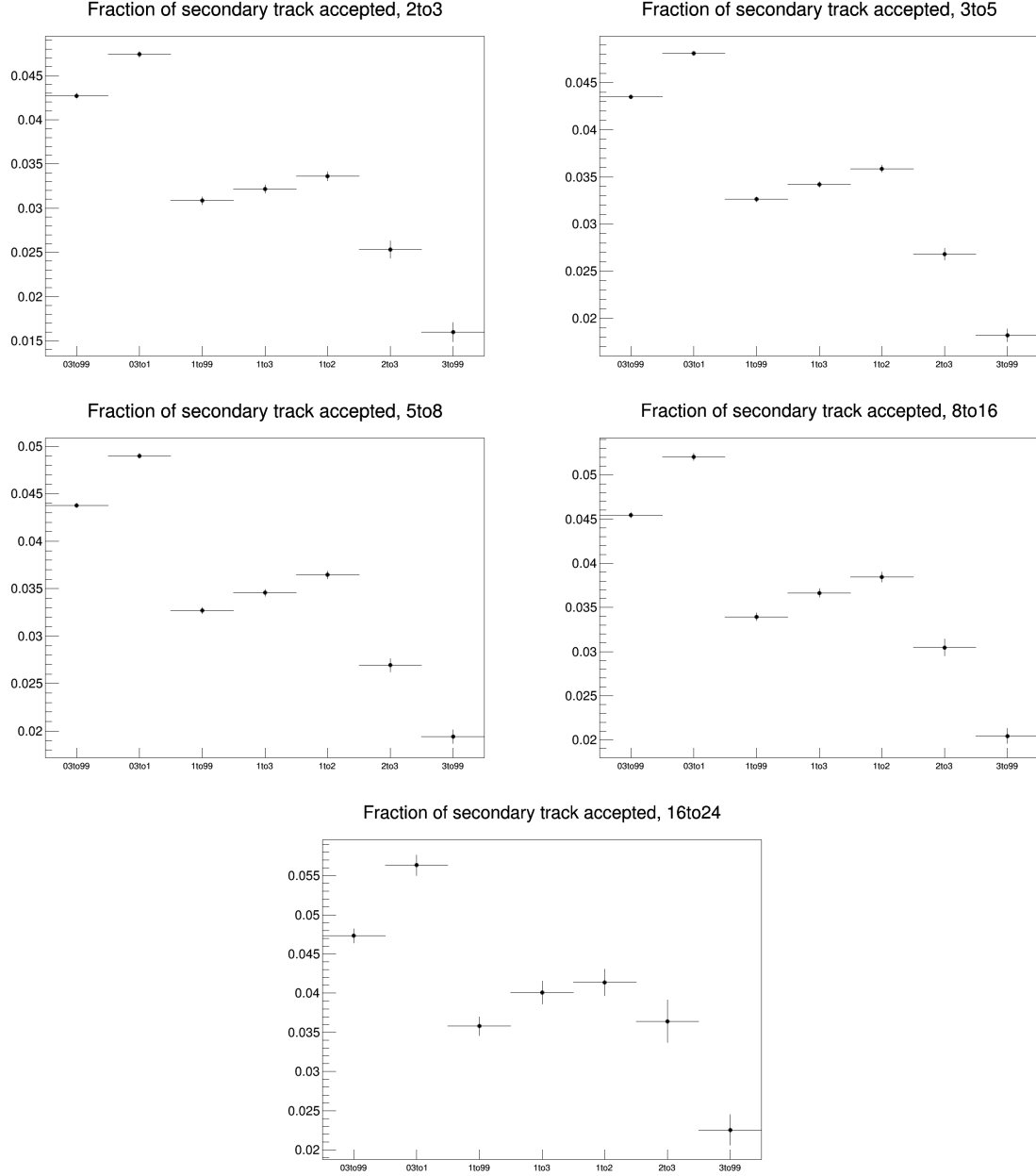


Figure 16: Fraction of secondary tracks over total amount of tracks which pass the DCA selection. The four panel show the fractions for the D-meson p_T ranges: 2-3, 3-5, 5-8, 8-16, 16-24, respectively. Inside each panel, the associated track p_T ranges are shown on the x -axis.

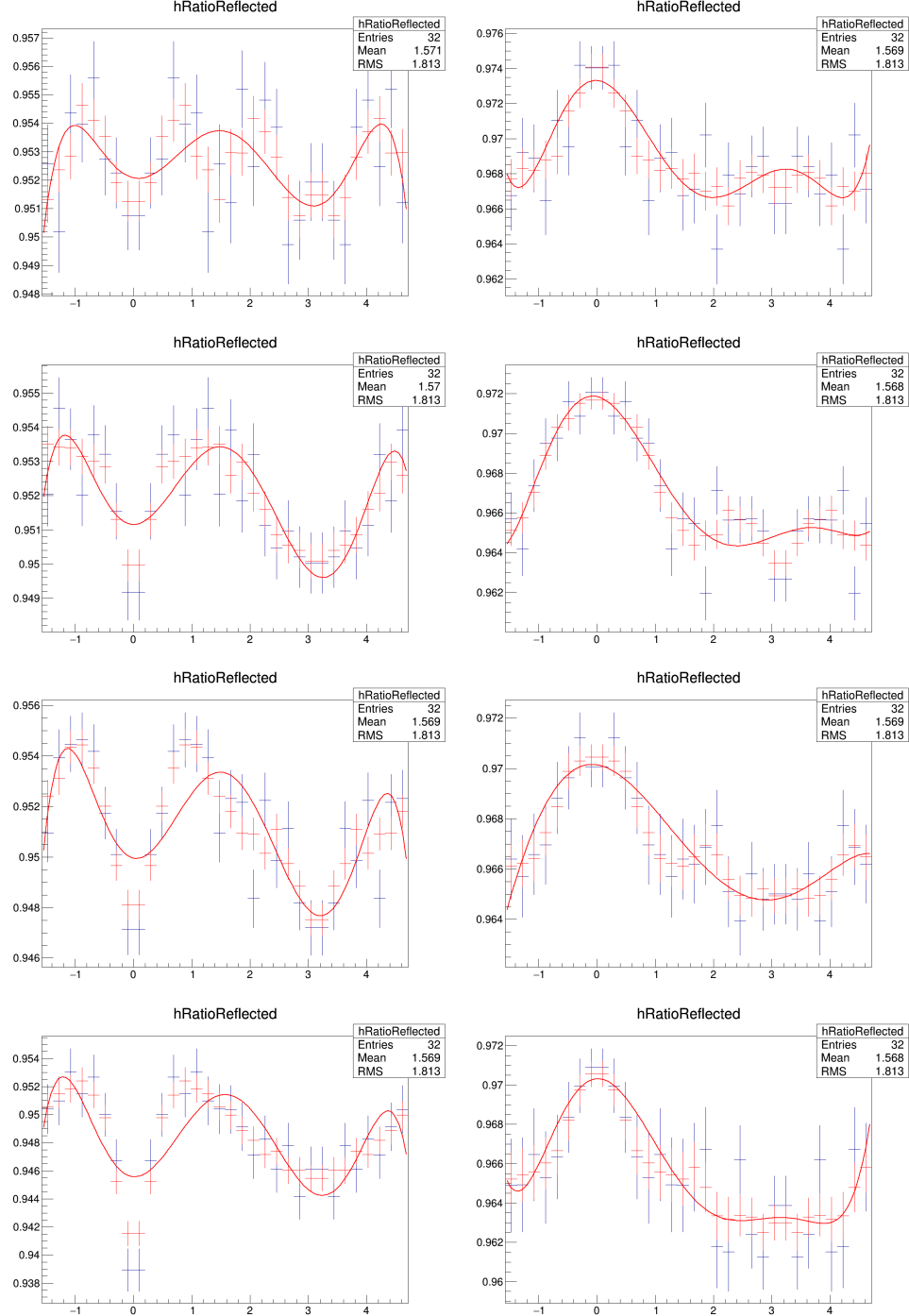


Figure 17: Fraction of primary track in the reconstructed associated track sample (blue histogram). The polynomial fit function (red curve) and the 3-point moving average (red histogram) are also superimposed. The $p_T(D)$ ranges are 2-3, 3-5, 5-8, 8-16 GeV/c, respectively for each row, and $0.3 < p_T(\text{assoc}) < 1$, $p_T(\text{assoc}) > 1$ GeV/c inside each row.

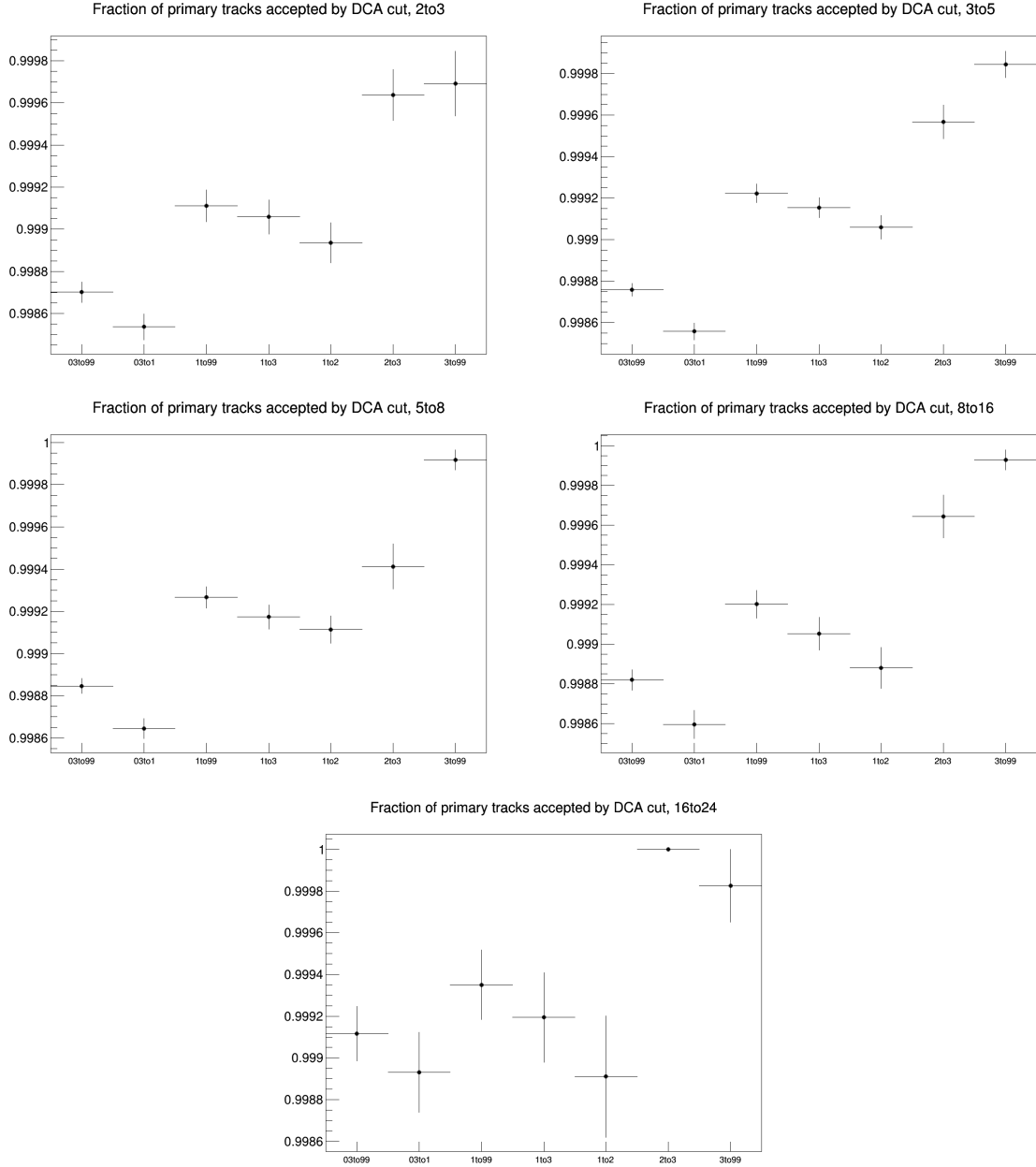


Figure 18: Fraction of primary tracks rejected by the DCA selection. The four panel show the fractions for the D-meson p_T ranges:2-3, 3-5, 5-8, 8-16, 16-24, respectively. Inside each panel, the associated track p_T ranges are shown on the x-axis.

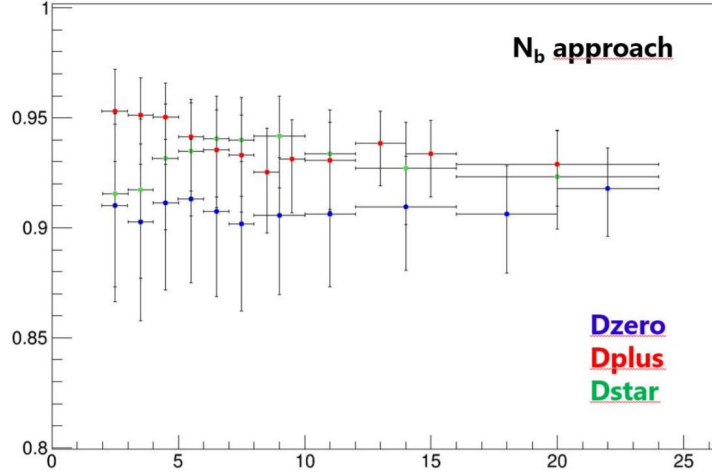


Figure 19: f_{prompt} as a function of the p_T for D^0 , D^{*+} and D^+ estimated on the basis of FONLL predictions

3.3.5 Beauty feed-down

The contribution of correlations of D meson from b-hadron decay is subtracted from the data correlation distributions as:

$$\tilde{C}_{\text{prompt } D}(\Delta\varphi) = \frac{1}{f_{\text{prompt}}} \left(\tilde{C}_{\text{inclusive}}(\Delta\varphi) - (1 - f_{\text{prompt}}) \tilde{C}_{\text{feed-down}}^{\text{MC templ}}(\Delta\varphi) \right). \quad (4)$$

In the above equation, $\tilde{C}_{\text{inclusive}}(\Delta\varphi)$ and $\tilde{C}_{\text{prompt } D}(\Delta\varphi)$ are per-trigger azimuthal correlation distributions before and after feed-down contribution subtraction, f_{prompt} is the fraction of prompt D meson and $\tilde{C}_{\text{feed-down}}^{\text{MC templ}}$ is a template of the azimuthal correlation distribution for the feed-down component obtained from home-made Monte Carlo simulation at generated level, using PYTHIA6 with Perugia2011 tune. In order to avoid biases related to the different event multiplicity in real and simulated events, the correlation distribution was shifted to have its minimum coinciding with the baseline of the data azimuthal-correlation distribution before feed-down subtraction. More details on the procedure can be found in [8].

The value of f_{prompt} (Figure 19), which depends on D-meson species and varies as a function of the p_T , is estimated on the basis of FONLL predictions for the production of feed-down D mesons at central rapidity, in pp collisions at $\sqrt{s} = 5$ TeV, and using the reconstruction efficiency of prompt and feed-down D mesons, following the so-called N_b approach defined in [1]. Typical values are about 8-10% for the D^0 , about 4-7% for the D^+ and about 5-8% for the D^{*+} , fully consistent with the value obtained for the p-Pb data sample, with rather similar cut selections.

4 Systematic uncertainties on $\Delta\phi$ correlation distributions

4.1 Uncertainty on S and B extraction

The systematic uncertainty for the D meson yield extraction was determined separately for the three mesons. It was obtained by evaluating the value of the signal candidate from the invariant mass spectra with the following differences with respect to the standard approach:

- Changing the background fit function, for D^0 and D^+ (tried with polynomials of 1st and 2nd order) and for D^{*+} (tried with polynomials of 2nd order and a power function);
- Changing the range in which the signal is extracted from the Gaussian fit;
- Reducing the range of invariant mass axis in which the signal region is defined (and S and B are extracted);
- Rebinning the invariant mass distributions before the fit for D^0 and D^+
- Extracting S and B via integral of the fit functions or B via bin counting and S via integral of the Gaussian function.

Both the value of the yield and the sidebands correlations normalization factor are affected by changing the yield extraction approach, while the rest of the procedure to extract the azimuthal correlation distribution is the same as in the standard analysis. The fully corrected azimuthal correlation plots were evaluated, for each of these approaches, in all D meson p_T bins and for each value of associated tracks p_T threshold. The ratios of the correlation distributions obtained with the standard yield extraction procedure and by differentiating the approach were evaluated. From the average of these ratios, which are found to be flat versus $\Delta\phi$, a systematic uncertainty can be extracted, which was taken of about 1% for $3 < p_T(D) < 16 \text{ GeV}/c$ and up to 3% in $16 < p_T(D) < 24 \text{ GeV}/c$. No dependence versus the associated track p_T was assumed, since from a physics point of view we don't expect a modification of the signal and sideband values to have a dependence of this kind. Figures 20, show the ratios obtained by the above mentioned procedure for exemplary p_T ranges, which anyway span over the full kinematic ranges analyzed, for D^0 -h correlations. Figures 21 and 22 show the same ratios for D^{*+} -h, D^+ -h as well.

4.2 Uncertainty on background correlation shape

The systematic uncertainty for the subtraction of the background correlations includes the effects due to a potentially biased description of the background correlation shape, which is evaluated from of the sidebands correlations. In particular, the background correlation shape could present some hidden invariant mass dependence. To estimate this uncertainty, the invariant mass range of the sidebands definitions was varied with respect to the default values. For the D^0 meson, the usual range of the sidebands is 4 to 8 σ from the centre of the peak of the Gaussian fit and it was modified, for both sidebands to:

- inner half (4 to 6 σ from the centre of the peak);
- outer half (6 to 8 σ from the centre of the peak)
- extended to 4 to 10 σ (in case this is possible without exceeding the fitting range of the mass plots)

Slightly different variations, but with the same reasoning, were considered for the D^+ meson.

For the D^{*+} meson, the usual range of sideband in invariant mass spectra is 5 to 10 σ (only on the right side) from the centre of the peak of the Gaussian fit of the invariant mass spectra, and it was modified to:

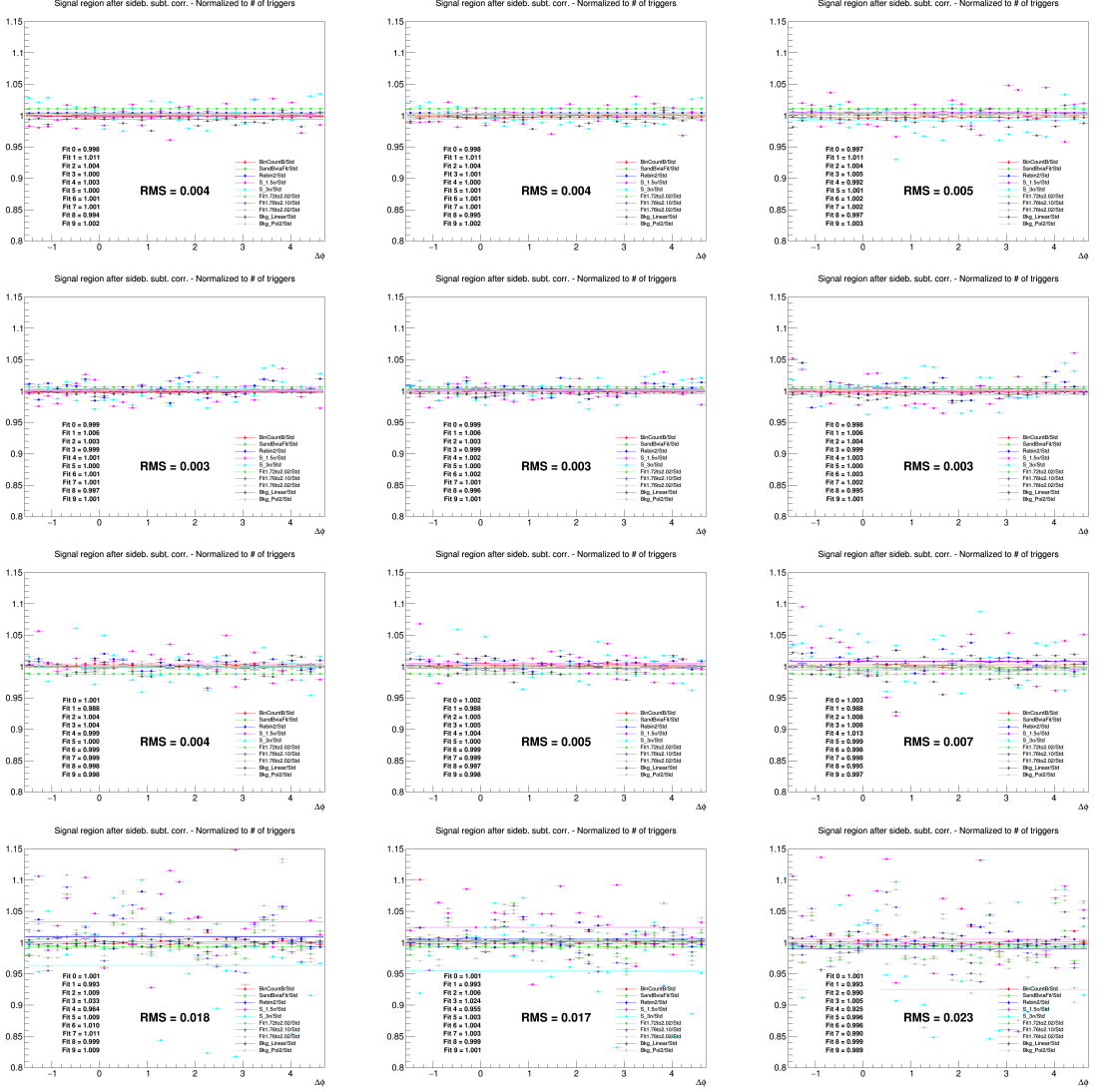


Figure 20: Ratios of D⁰-h correlation plots obtained changing S and B extraction procedure over those obtained with standard yield extraction procedure. Rows: p_T(D⁰) 3-5, 5-8, 8-16, 16-24 GeV/c. In each row, the panels show the associated track p_T ranges 0.3-1 GeV/c, >0.3 GeV/c, and >1 GeV/c, respectively.

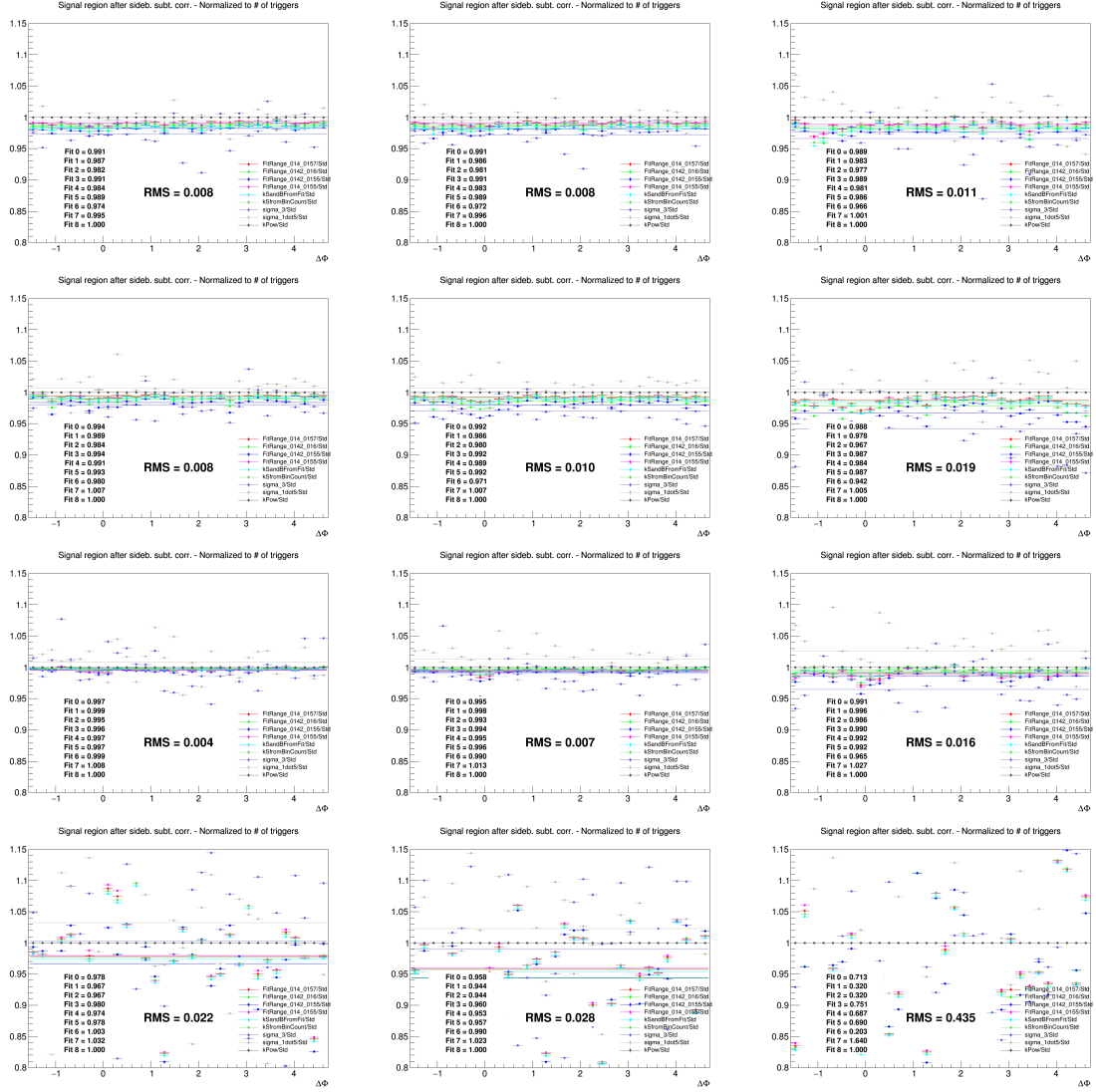


Figure 21: Ratios of $D^*+ - h$ correlation plots obtained changing S and B extraction procedure over those obtained with standard yield extraction procedure. Rows: $p_T(D^*)$ 3-5, 5-8, 8-16, 16-24 GeV/c . In each row, the panels show the associated track p_T ranges $>0.3 \text{ GeV}/c$, $0.3\text{-}1 \text{ GeV}/c$ and $>1 \text{ GeV}/c$, respectively.

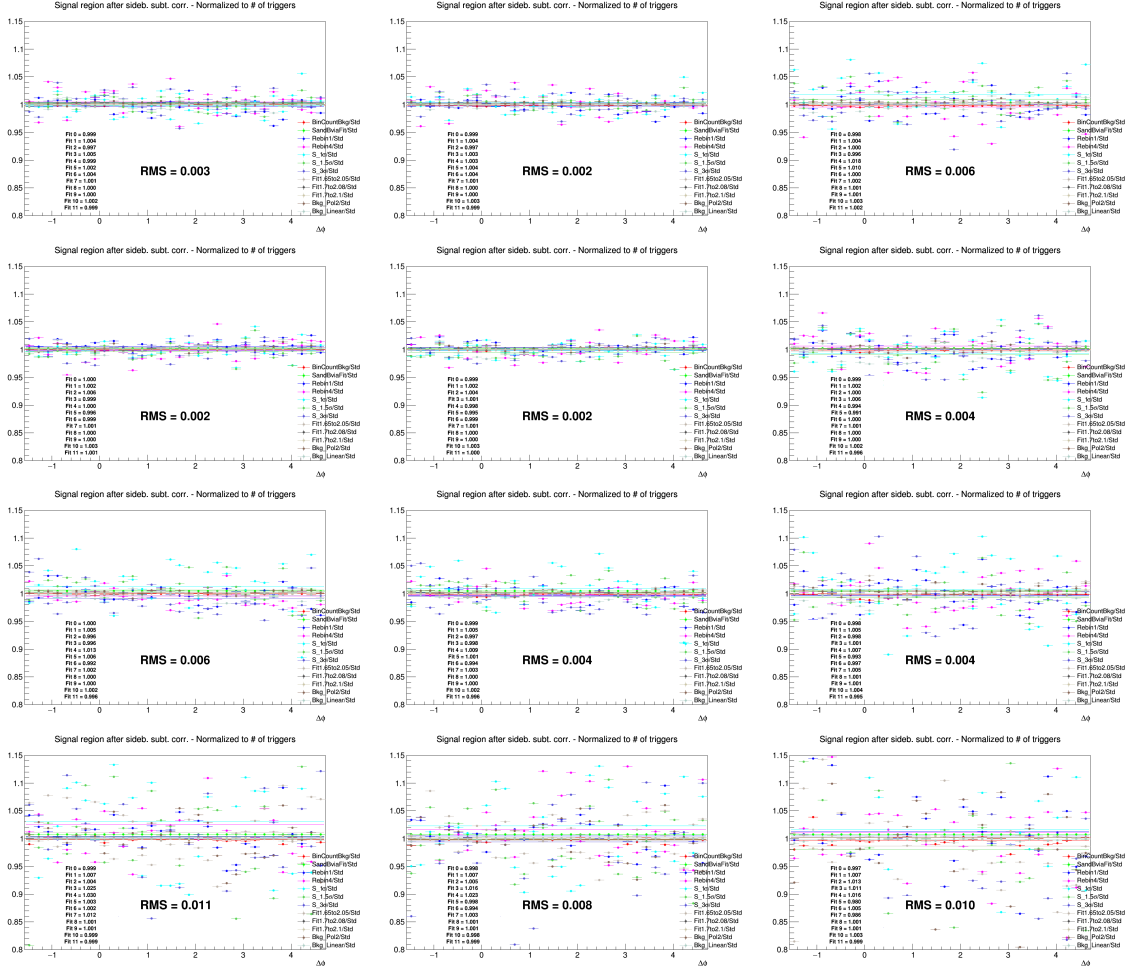


Figure 22: Ratios of D⁺ - h correlation plots obtained changing S and B extraction procedure over those obtained with standard yield extraction procedure. Rows: $p_T(D^+)$ 3-5, 5-8, 8-16, 16-24 GeV/c. In each row, the panels show the associated track p_T ranges 0.3-1 GeV/c, >0.3 GeV/c, and >1 GeV/c, respectively.

- 499 – inner half (5 to 8 σ from the centre of the peak);
- 500 – outer half (8 to 13 σ from the centre of the peak);
- 501 – extended to 5 to 13 σ from the centre of the peak;
- 502 – extended to 6 to 16 σ from the centre of the peak.

503 The rest of the procedure for the azimuthal correlations distribution was unchanged, and the ratios of
 504 the fully corrected azimuthal correlation plots obtained with the standard sidebands range and the corre-
 505 lation plots extracted with different sidebands definitions, were evaluated for each D-meson p_T bin and
 506 associated tracks p_T threshold. Results of this check are shown in Figures 23, 24 and 25 for D^0 , D^{*+} ,
 507 D^+ respectively, for exemplary p_T ranges, spanning over the full kinematic regions analysis. From the
 508 values of the ratios extracted from the checks, which do not show any azimuthal dependence a systematic
 509 uncertainty for the background subtraction can be evaluated. Also no dependence versus the associated
 510 track p_T was assumed also in this case. The uncertainty was hence taken of 1-2% for all the mesons in
 511 $3 < p_T(D) < 16 \text{ GeV}/c$ and up to 3% in $16 < p_T(D) < 24 \text{ GeV}/c$.

512 4.3 Uncertainty on D-meson cut stability

513 To study the systematics due to the topological selections on the D meson, the cut variation approach was
 514 used. For each D-meson, alternate sets of released and tightened selection cuts were applied to extract
 515 the correlation distribution, varying in particular the cosine of the pointing angle, the maximum DCA
 516 among the daughter tracks and the product of the daughter track impact parameters. For each set of cuts
 517 new 2D (p_T vs multiplicity), D meson efficiency map was computed. In Figures 26, 27, 28 (for D^0 , D^{*+}
 518 and D^+ , respectively) the ratio of the different 1D efficiencies with the alternate cuts with respect to the
 519 default cut selection is chosen, to highlight how the different selections effectively varied the efficiency
 520 values, especially at low p_T , where cuts are more effective.

521 Figure 29, 30, 31 show the ratio of the correlation distributions with alternate cut sets over those with the
 522 standard approach, for exemplary p_T ranges covering the full kinematic region of interest for the analyses.
 523 The ratios are reasonably flat in $\Delta\phi$, hence a flat systematic was evaluated as systematic uncertainty from
 524 D-meson the cut variations. For the D^0 , the uncertainty was considered of 2% for all the p_T ranges of
 525 trigger and tracks analyzed. The uncertainty was evaluated to be from 1% to 2.5% depending on the
 526 D-meson specie and on the kinematic range.

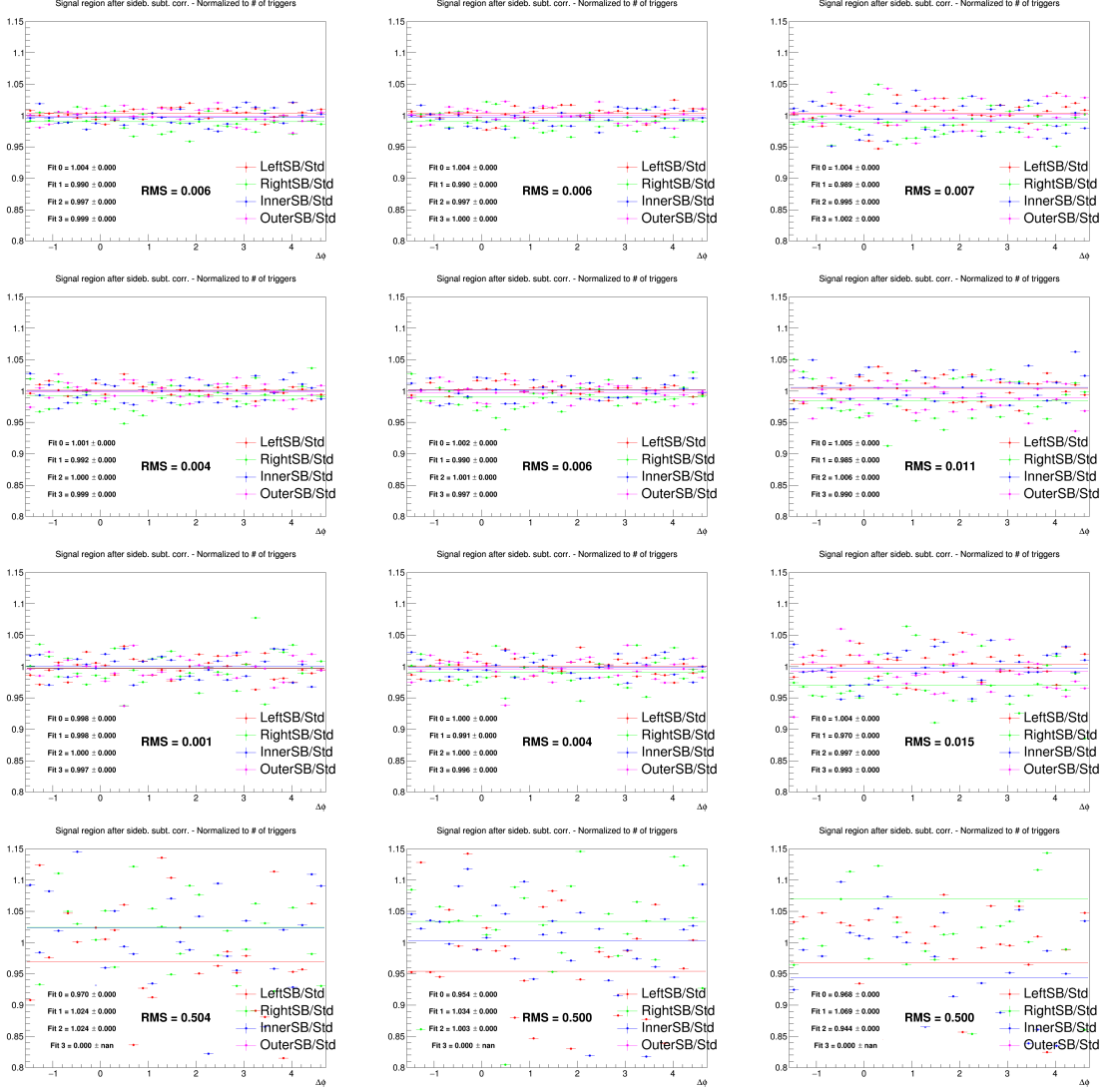


Figure 23: Ratios of D⁰-h correlation plots obtained by changing the sideband ranges over those obtained with standard sideband ranges. Rows: p_T(D⁰) 3-5, 5-8, 8-16, 16-24 GeV/c. In each row, the panels show the associated track p_T ranges 0.3-1, >0.3 GeV/c and >1 GeV/c, respectively.

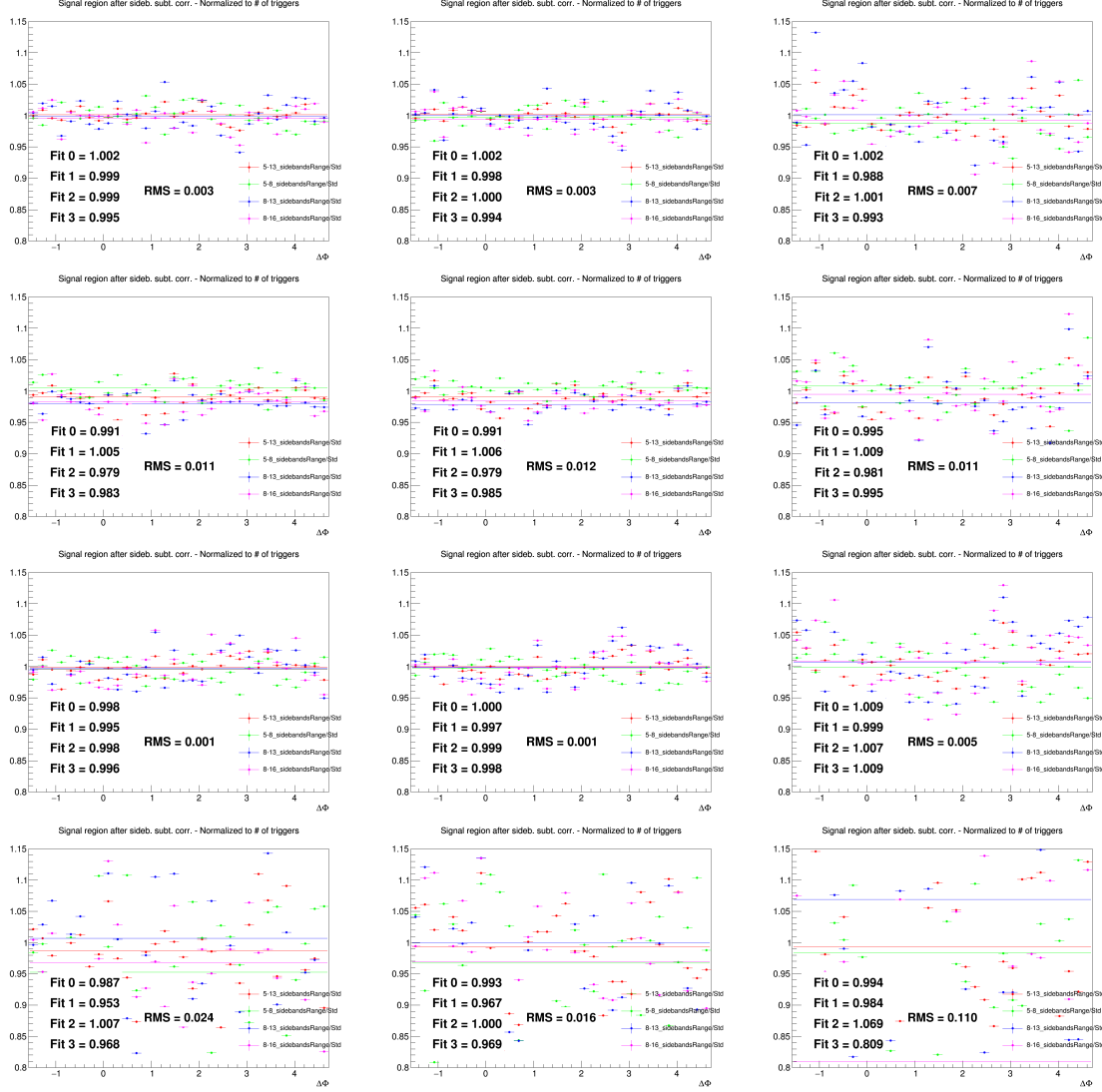


Figure 24: Ratios of $D^*+ - h$ correlation plots obtained by changing the sideband ranges over those obtained with standard sideband ranges. Rows: $p_T(D^*)$ 3-5, 5-8, 8-16, 16-24 GeV/ c . In each row, the panels show the associated track p_T ranges 0.3-1, >0.3 GeV/ c and >1 GeV/ c , respectively.

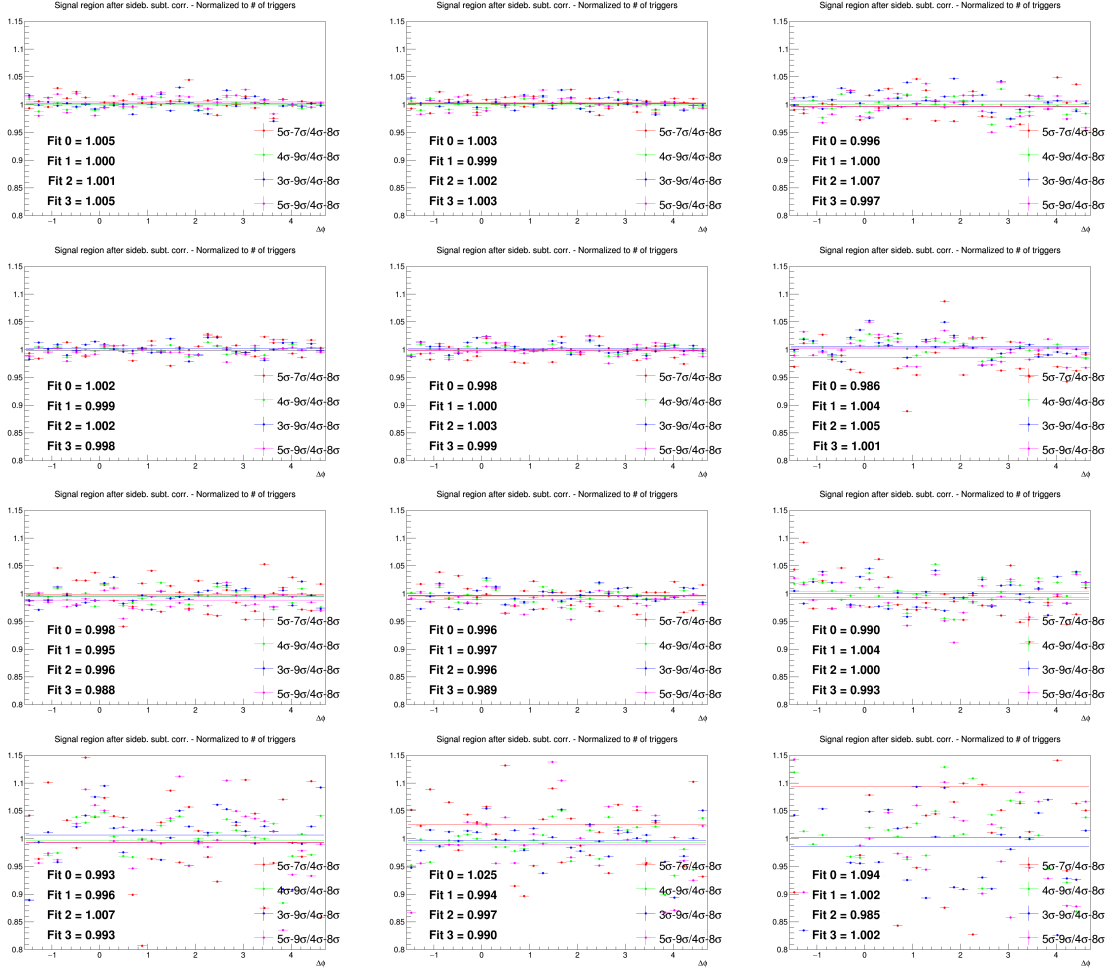


Figure 25: Ratios of D⁺-h correlation plots obtained by changing the sideband ranges over those obtained with standard sideband ranges. Rows: $p_T(D^+)$ 3-5, 5-8, 8-16, 16-24 GeV/c. In each row, the panels show the associated track p_T ranges 0.3-1, >0.3 GeV/c and >1 GeV/c, respectively.

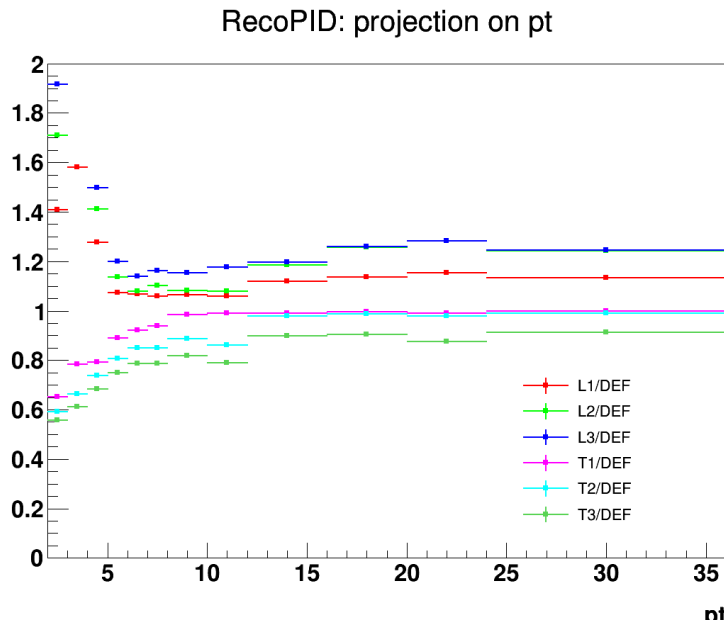


Figure 26: Ratio of D^0 efficiencies with alternate cut variations w.r.t. the standard cut used for the analysis.

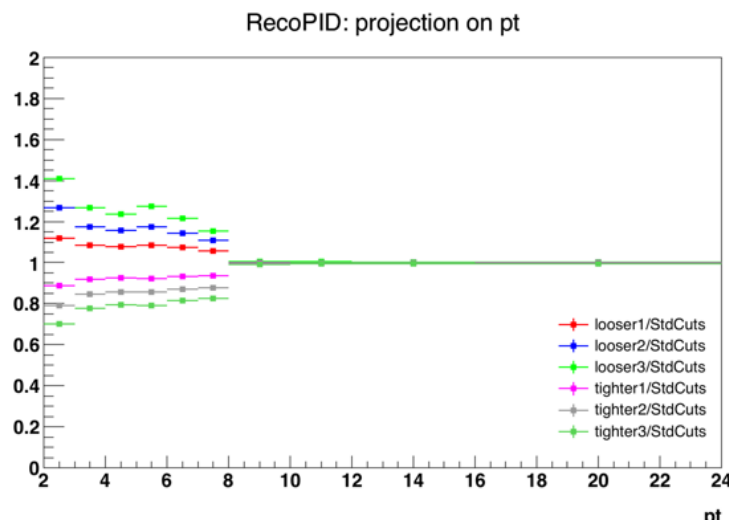


Figure 27: Ratio of D^{*+} efficiencies with alternate cut variations w.r.t. the standard cut used for the analysis.

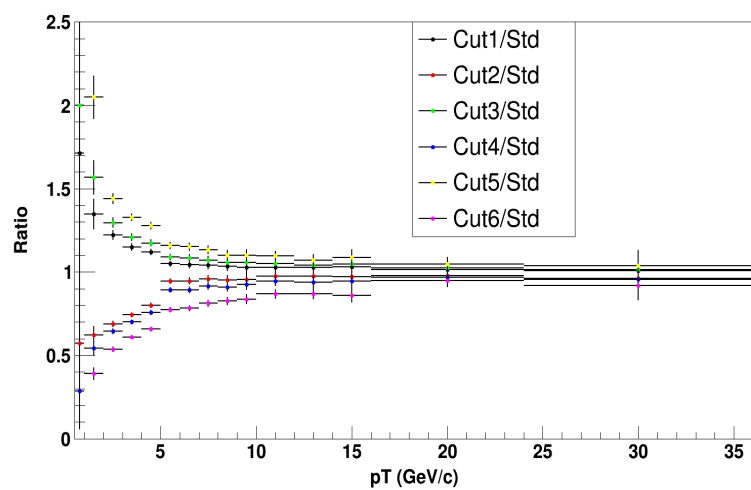


Figure 28: Ratio of D⁺ efficiencies with alternate cut variations w.r.t. the standard cut used for the analysis.

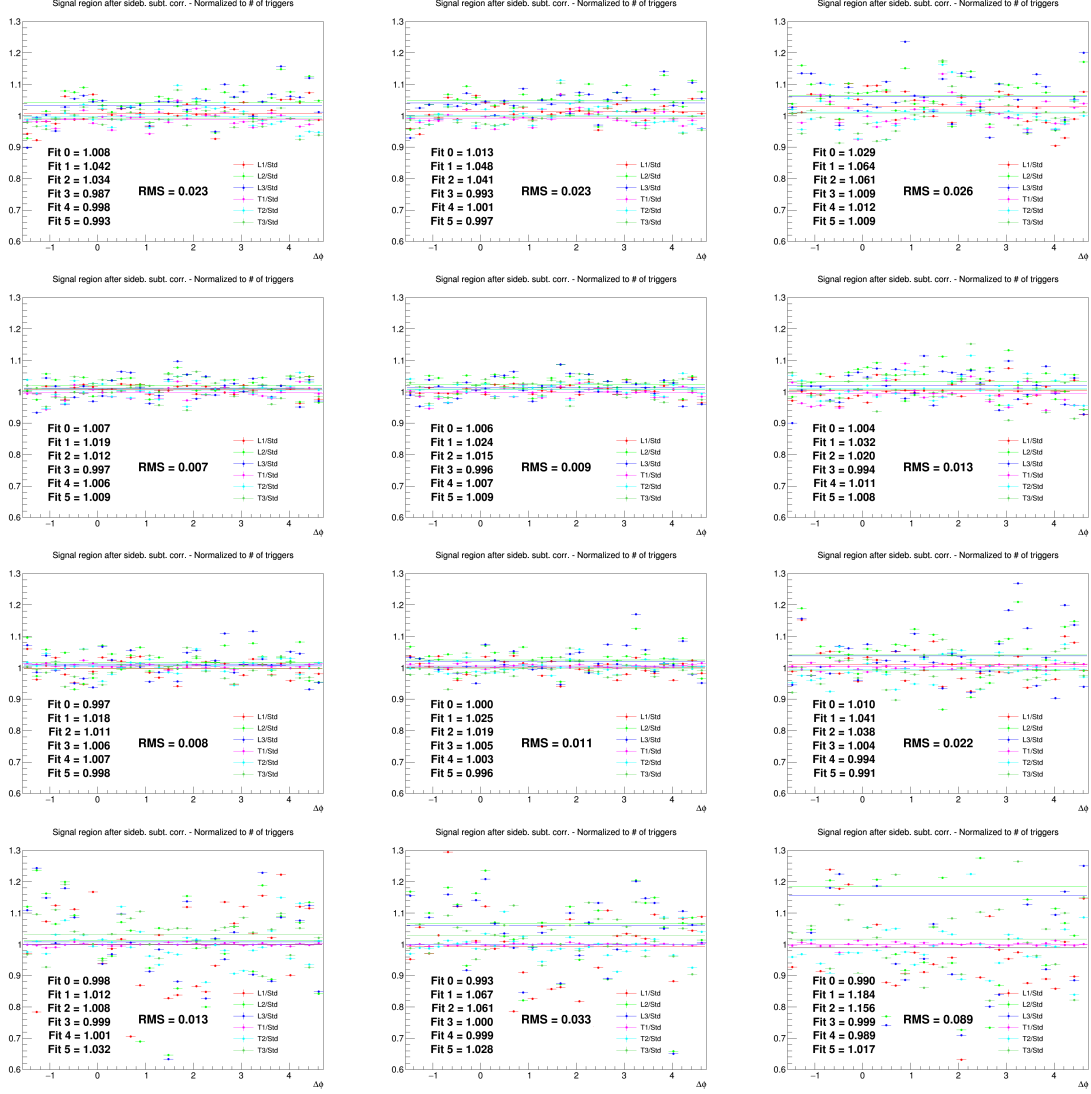


Figure 29: Ratios of D^0 -h correlation plots obtained with alternate D-meson cut sets over those obtained with standard selection. Rows: $p_T(D^0)$ 3-5, 5-8, 8-16, 16-24 GeV/c. In each row, the panels show the associated track p_T ranges 0.3-1, >0.3 GeV/c, >1 GeV/c, respectively.

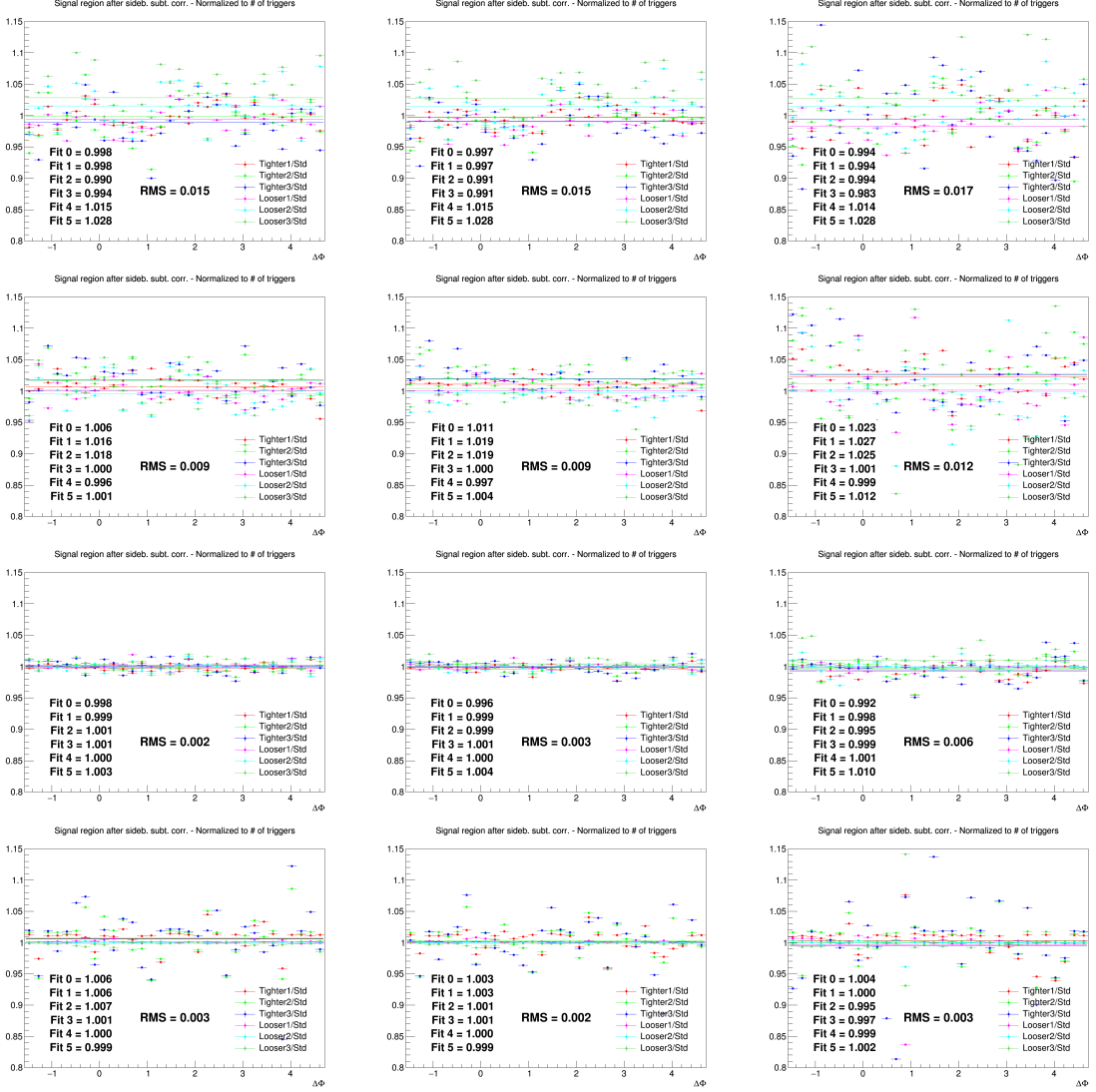


Figure 30: Ratios of D^{*+} - h correlation plots obtained with alternate D-meson cut sets over those obtained with standard selection. Rows: $p_T(D^{*+})$ 3-5, 5-8, 8-16, 16-24 GeV/ c . In each row, the panels show the associated track p_T ranges 0.3-1, >0.3 GeV/ c , >1 GeV/ c , respectively.

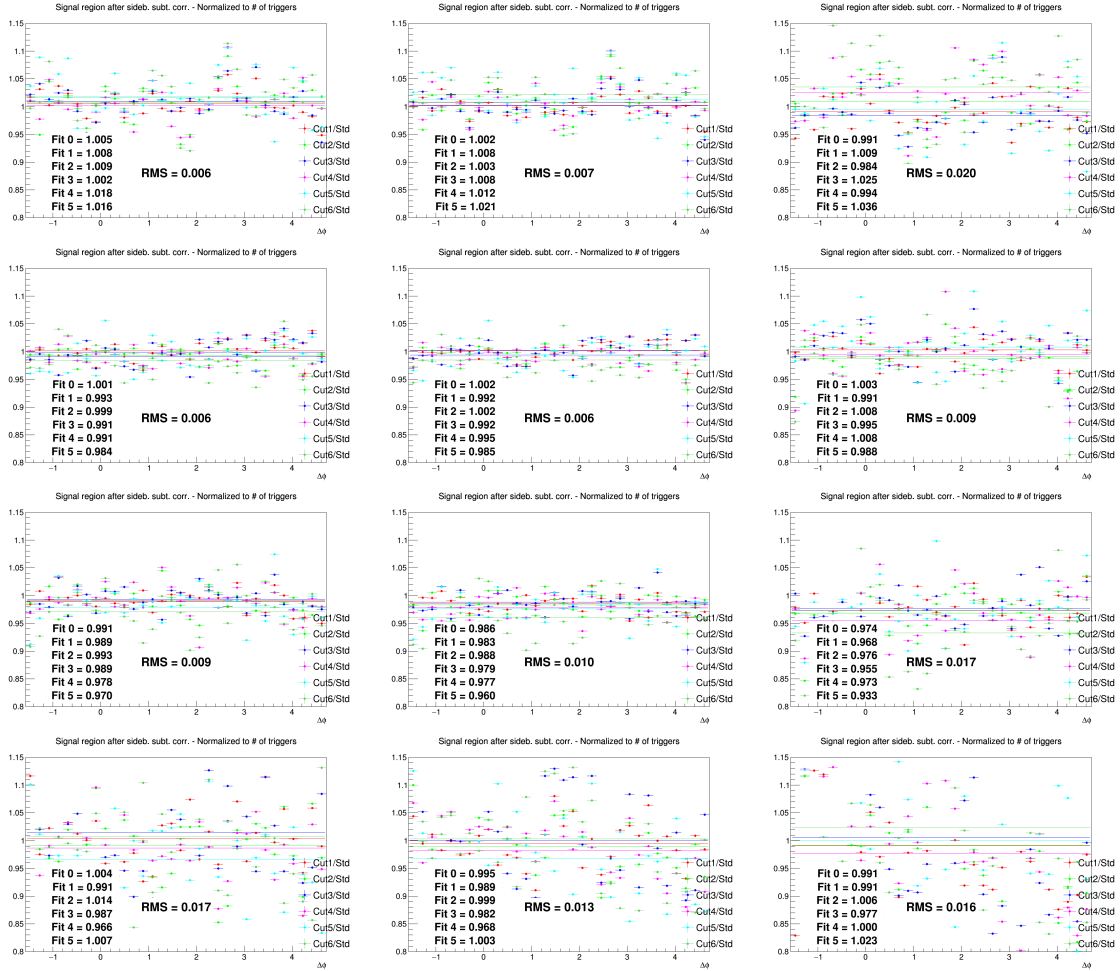


Figure 31: Ratios of $D^+ - h$ correlation plots obtained with alternate D-meson cut sets over those obtained with standard selection. Rows: $p_T(D^+)$ 3-5, 5-8, 8-16, 16-24 GeV/ c . In each row, the panels show the associated track p_T ranges 0.3-1, >0.3 GeV/ c , >1 GeV/ c , respectively.

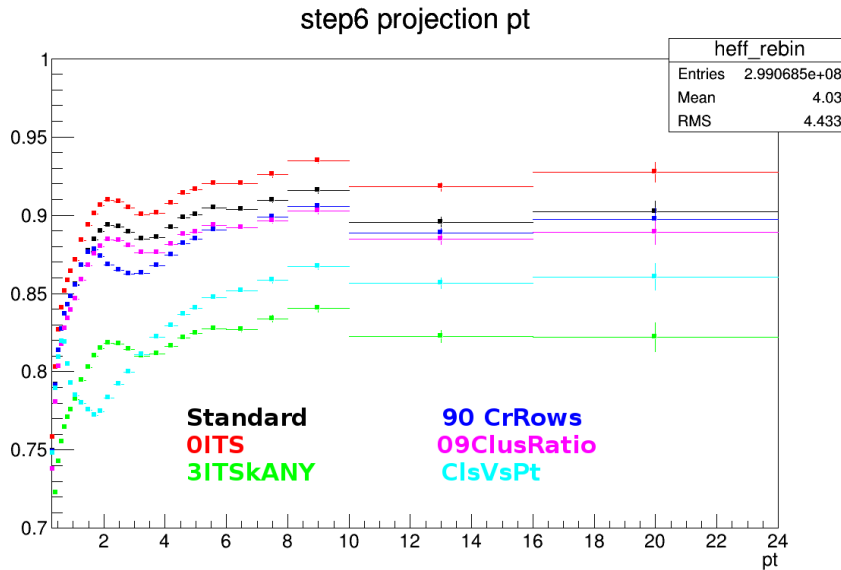


Figure 32: Associated track selection and reconstruction efficiencies for alternate selections.

527 4.4 Uncertainty on tracking efficiency evaluation

528 The systematic uncertainty assigned to cover a possible bias on the associated tracking efficiency is eval-
 529 uated by varying the associated track selection. With respect to what done in subsection 4.4, additional
 530 variations were studied, for all the D-mesons, in particular:

- 531 – No request on the minimum number of ITS clusters
- 532 – Minimum 3 ITS clusters + kAny request for SPD + filterbit 4 request
- 533 – Minimum number of TPC crossed row of 90
- 534 – Minimum ratio of TPC crossed rows/findable crossed rows of 0.9
- 535 – p_T -dependent cut on minimum number of TPC clusters ($> 120 - (5/p_T)$)

536 Figures 32 show the associated track selection and reconstruction efficiencies (and their ratios w.r.t.
 537 standard-cut efficiency) for alternate cut sets.

538 In Fig. 33, 35, 34 the ratios of correlation distributions with alternate/standard track selections are shown,
 539 in the various p_T ranges, for the D^0 , D^{*+} and D^+ mesons as trigger, respectively. For this uncertainty,
 540 to the values obtained from the above ratio an additional 2%, for a wrong evaluation of the ITS-TPC
 541 matching efficiency, is added in quadrature, as prescribed by the DPG group (being 1% for associated
 542 track $p_T < 1$, 2% in 1-2 and 2.7% in 2-3 GeV/c). The assigned uncertainty is 3 to 4.5%, slightly
 543 increasing with the p_T of the associated tracks (mainly due to the increase of the ITS-TPC matching
 544 efficiency).

545 4.5 Uncertainty on secondary particle contamination

546 Secondary particles, i.e. particles coming from strange hadrons decays or particles produced in inter-
 547 actions with the material, are expected to be tagged and removed by means of a distance of closest
 548 approach (DCA) from primary vertex cut. The uncertainty arising from the residual contamination of
 549 secondary tracks can be estimated from a Monte Carlo study, at reconstructed level. The number of
 550 primary/secondary tracks which are accepted/rejected from the DCA cut was determined for different

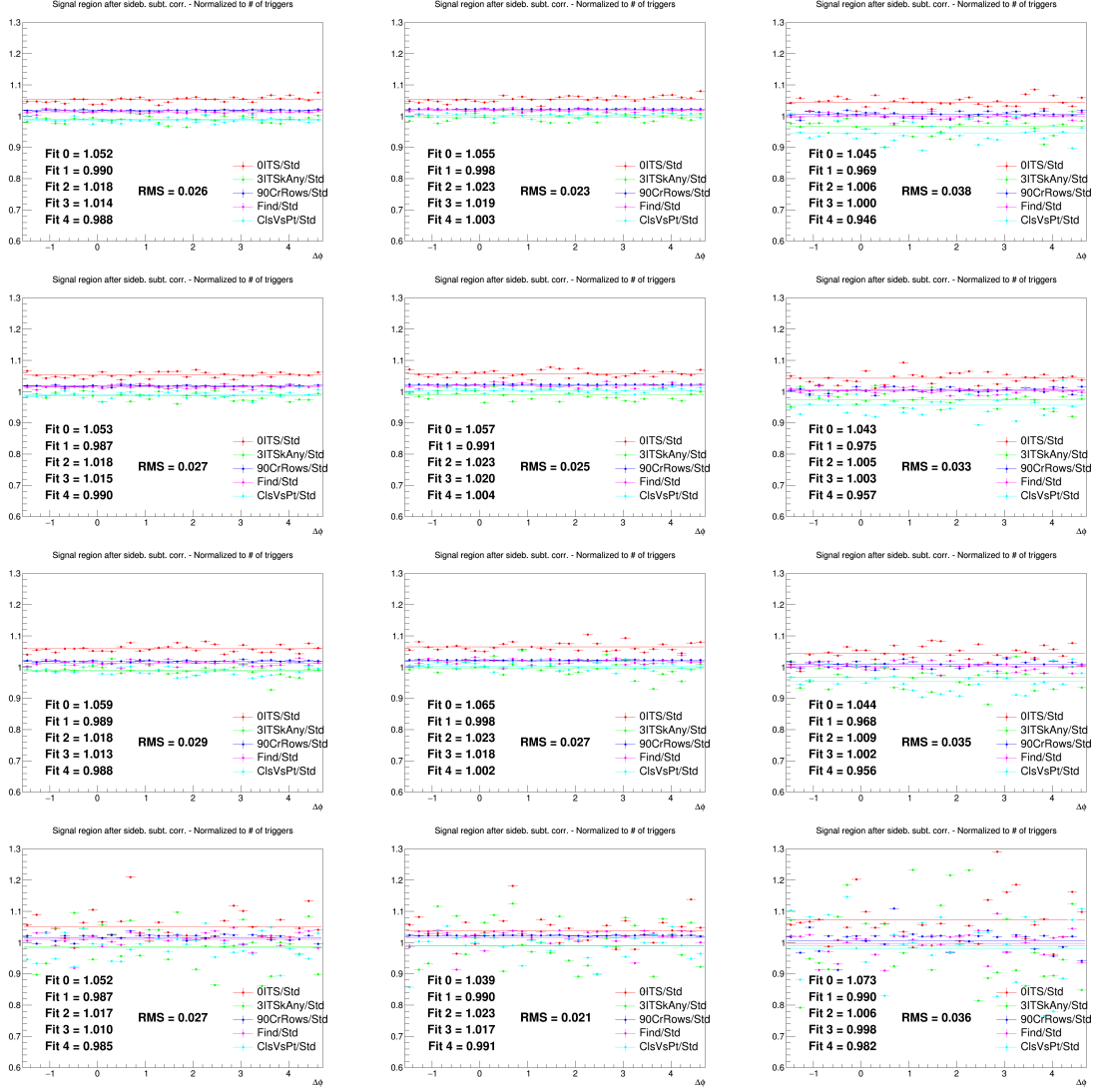


Figure 33: Ratios of D⁰-h correlation plots obtained with alternate associated track selection over those obtained with the standard cuts. Rows: $p_T(D^0)$ 3-5, 5-8, 8-16, 16-24 GeV/c. In each row, the panels show the associated track p_T ranges > 0.3, 0.3-1, > 1 GeV/c, respectively.

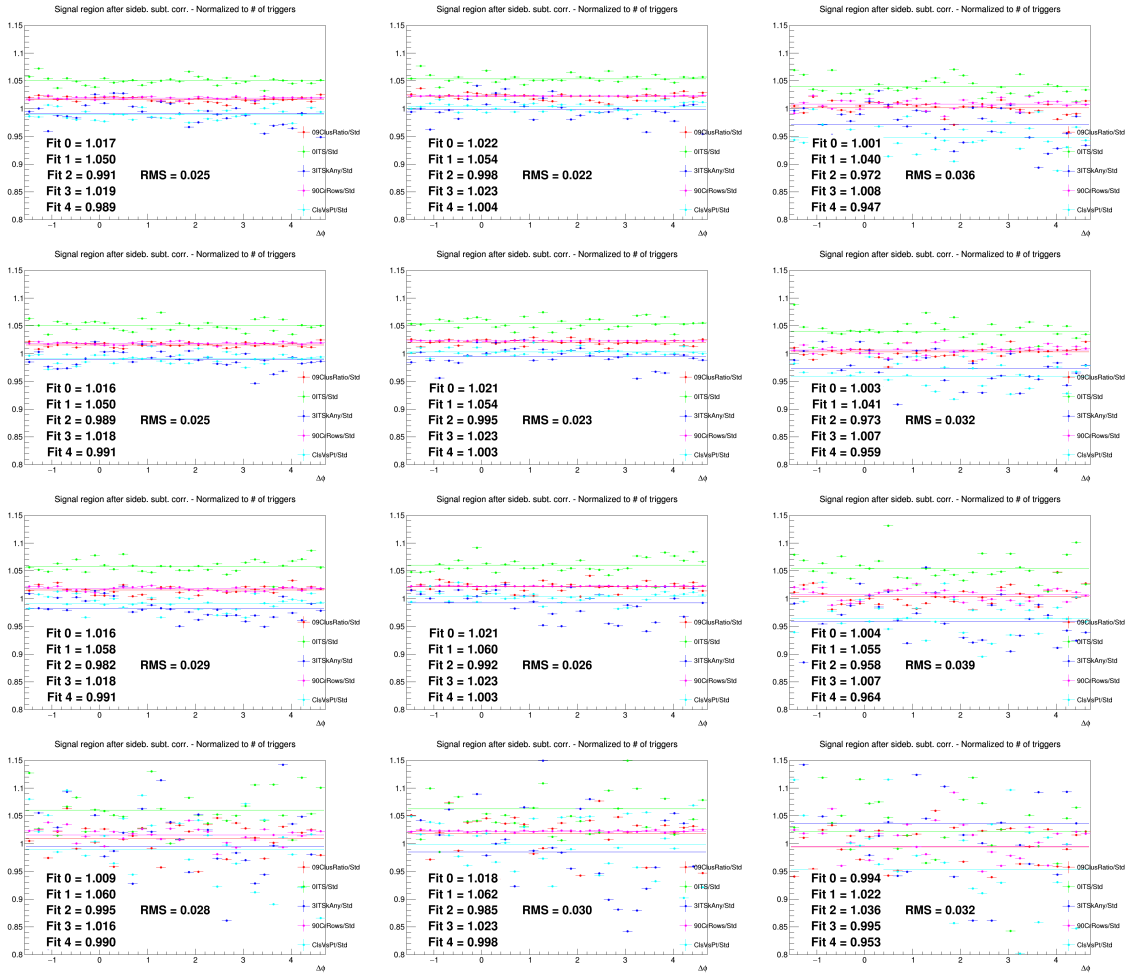


Figure 34: Ratios of D⁺-h correlation plots obtained with alternate associated track selection over those obtained with the standard cuts. Rows: $p_T(D^+)$ 3-5, 5-8, 8-16, 16-24 GeV/c. In each row, the panels show the associated track p_T ranges > 0.3, 0.3-1, > 1 GeV/c, respectively.

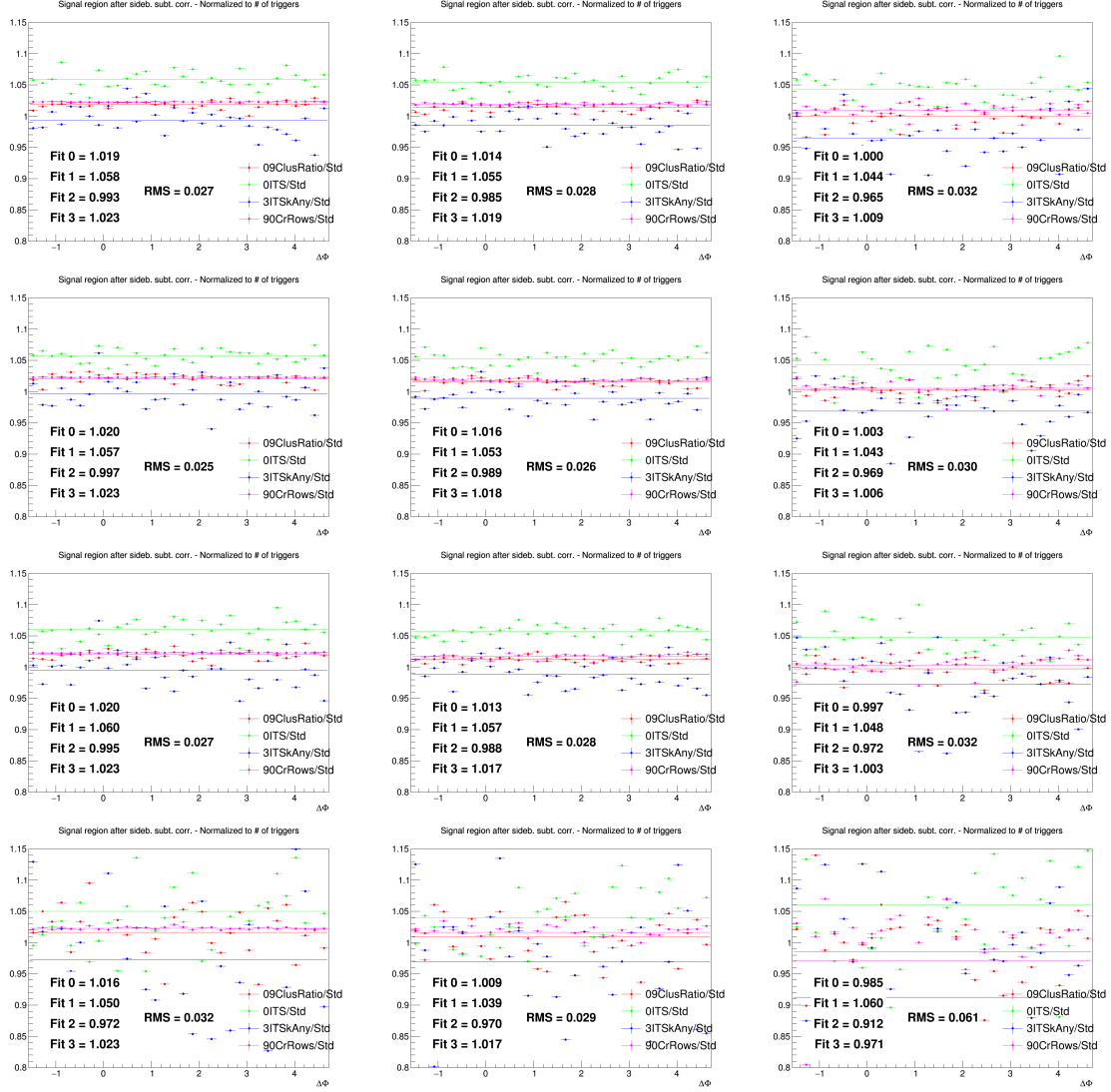


Figure 35: Ratios of D^{*+} - h correlation plots obtained with alternate associated track selection over those obtained with the standard cuts. Rows: $p_T(D^{*+})$ 3-5, 5-8, 8-16, 16-24 GeV/c . In each row, the panels show the associated track p_T ranges > 0.3 , $0.3-1$, $> 1 \text{ GeV}/c$, respectively.

values of the DCA selection, and the correlation distributions for the various cases were evaluated. The variations were done in the xy direction, where the DCA resolution is better, and the following cases were tried (in addition to the default 1 cm cut): 0.1 cm, 0.25 cm, 0.5 cm, filtering DCA cut (i.e. 2.4 cm).

Figure 36 shows the amount of secondary tracks which are accepted by the DCA cut, over the total number of tracks (primary and secondary) accepted by the selection, for the various DCA selections that were tried. This is shown for the exemplary case of $5 < p_T < 8 \text{ GeV}/c$ (there's no $p_T(D)$ dependence) and as a function of the associated track p_T ranges. Hence, this quantity represents the residual contamination of secondary tracks in our reconstructed track sample. From these values, the corresponding primary track purities (1-contamination) were extracted, in each of the momentum ranges. It was also verified that, for all the cut selections, the $\Delta\phi$ distributions of the residual contaminations were rather flattish (anyway, a bin-by-bin dependent purity correction value was evaluated, as for the standard analysis).

As a second step of the procedure to verify the DCA cut stability, the D^0 -h data analysis was performed with all the different DCA selection (each time with the proper tracking efficiency map). After having extracted the correlation distributions, these were rescaled (bin-by-bin) for the corresponding purities and compared with the purity-corrected correlation distributions obtained with the standard DCA selection. The ratios of the alternate selections over the standard selection, after the purity correction of both, are shown in Figures 37 and 38.

The ratios show a flat trend along the $\Delta\phi$ axis and, in general, a discrepancy from the value of 1 of no more than 3% (the worst case being the 0.3-1 GeV/c range for the associated track). Hence, a flat and symmetric 2% systematical uncertainty on the evaluation of the secondary contamination was assigned on the base of this check in 0.3-1 GeV/c , reduced to 1% in 2 – 3 0.3 GeV/c and to 1.5% for the other ranges.

4.6 Uncertainty on feed-down subtraction

As described in Sect. 3.3.5, the feed-down subtraction from the data distributions is performed by means of simulation templates of $B \rightarrow D$ -h correlation distributions from PYTHIA6 generator, with Perugia2011 tune, and considering the central value of f_{prompt} to extract the feed-down D-meson contribution. In order to evaluate a systematic uncertainty on this procedure, the feed-down subtraction procedure was repeated considering, together with PYTHIA6+Perugia2011 templates, also PYTHIA6+Perugia2010 and PYTHIA8 simulations. In each case, not only the central value of the measured f_{prompt} was considered to rescale the distributions, but also the maximum and minimum values of its total uncertainty.

Then, the envelope of nine the different cases obtained by varying the templates and the f_{prompt} assumption was considered, and a value of the systematics defined as the envelope spread divided by $\sqrt{3}$ was taken as systematic uncertainty. This uncertainty was assumed uncorrelated among the different $\Delta\phi$ points.

4.7 Uncertainty on correction for the bias on B to D decay topologies

The evaluation of this systematic uncertainty was already explained in Section 3.3.3. For each of the five data points close to the center of the near-side peak, which are affected by the bias, a bilateral and symmetric uncertainty of amplitude $|C(\Delta\phi)_{\text{corr}} - C(\Delta\phi)_{\text{raw}}|/\sqrt{12}$ was assigned.

This because the uncorrected data points are expected to be the extreme (with the current D-meson selection, the bias is always upwards at the centre of the peak, and always upwards on its sides). We then assume that, if the correction is properly evaluated, the corrected data points are at the centre of the possible spread of the true unbiased results. In this case, the span of the possible true results (in case of underestimation/overestimation of the bias) goes from the uncorrected data points to its symmetric value, with respect to the corrected data point, on the other direction. If this distribution is uniform, and constrained by these two values, the 1σ confidence region for the position of the true value of the

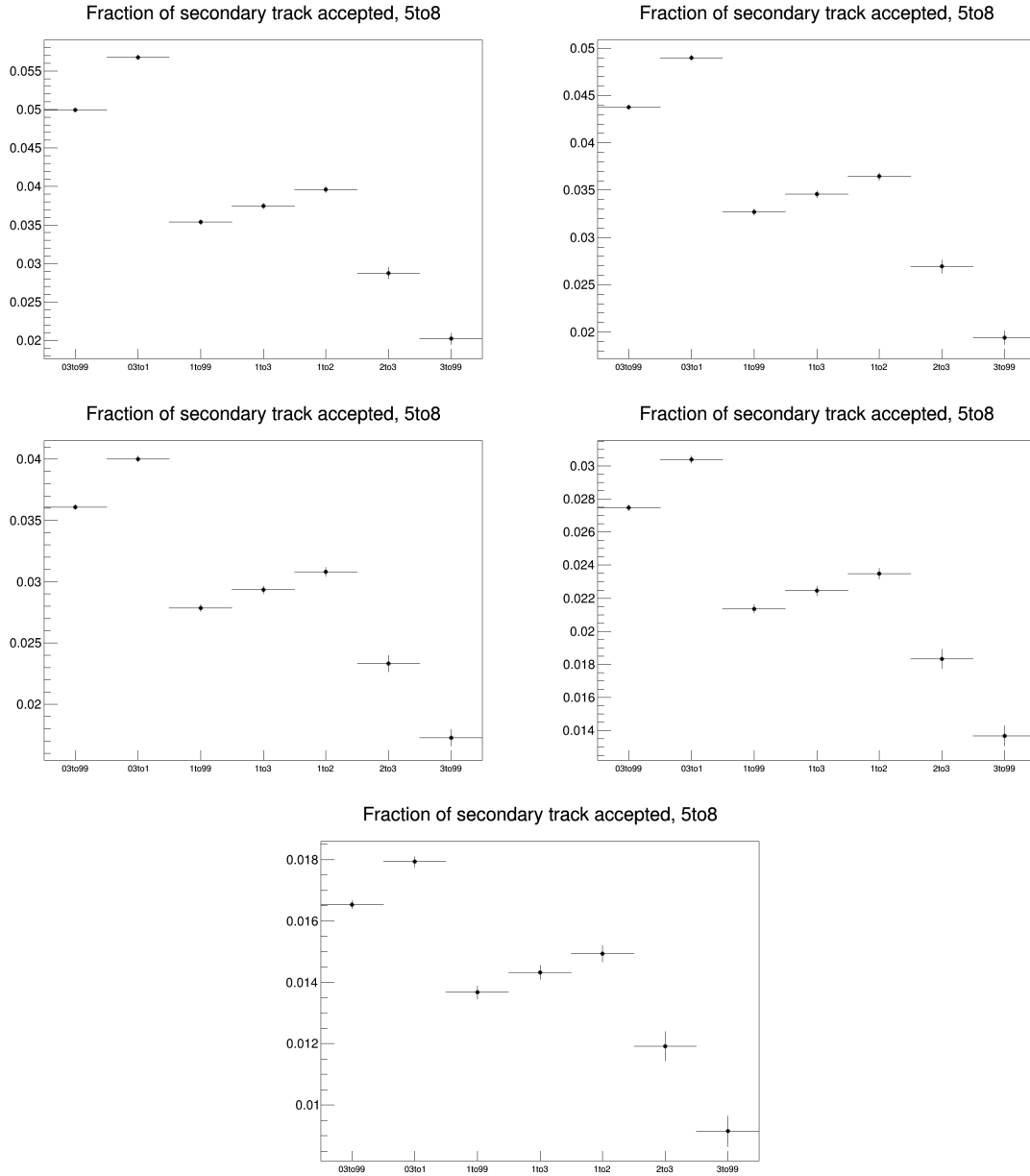


Figure 36: Secondary track contamination as a function of the associated track p_T , for the various DCA selections tried. The plots are ordered from the loosest to the tightest selection, i.e.: DCA(xy) < 2.4 cm, < 1 cm, < 0.5 cm, < 0.25 cm, < 0.1 cm.

596 unbiased points is in a bilateral $|C(\Delta\phi)_{\text{corr}} - C(\Delta\phi)_{\text{raw}}|/\sqrt{12}$ window, centered on the $C(\Delta\phi)_{\text{corr}}$ points.

597 This source of uncertainty was assumed uncorrelated among the $\Delta\phi$ points.

598 4.8 Summary table

599 A summary of the $\Delta\phi$ -correlated uncertainties affecting the correlation distributions is shown in Figure
600 39. They are the S and B extraction uncertainty, the background shape uncertainty, the cut variation
601 uncertainty, the tracking efficiency uncertainty and the secondary particle contamination uncertainty.

602 The overall amount of $\Delta\phi$ -correlated uncertainties is lower than 6% (depending on the p_T bin) for the
603 single D-meson cases; when evaluating the averages of the distributions (see next section), this uncer-
604 tainty shrinks to a maximum of about 5%. This uncertainty is a global scale factor of the distributions,

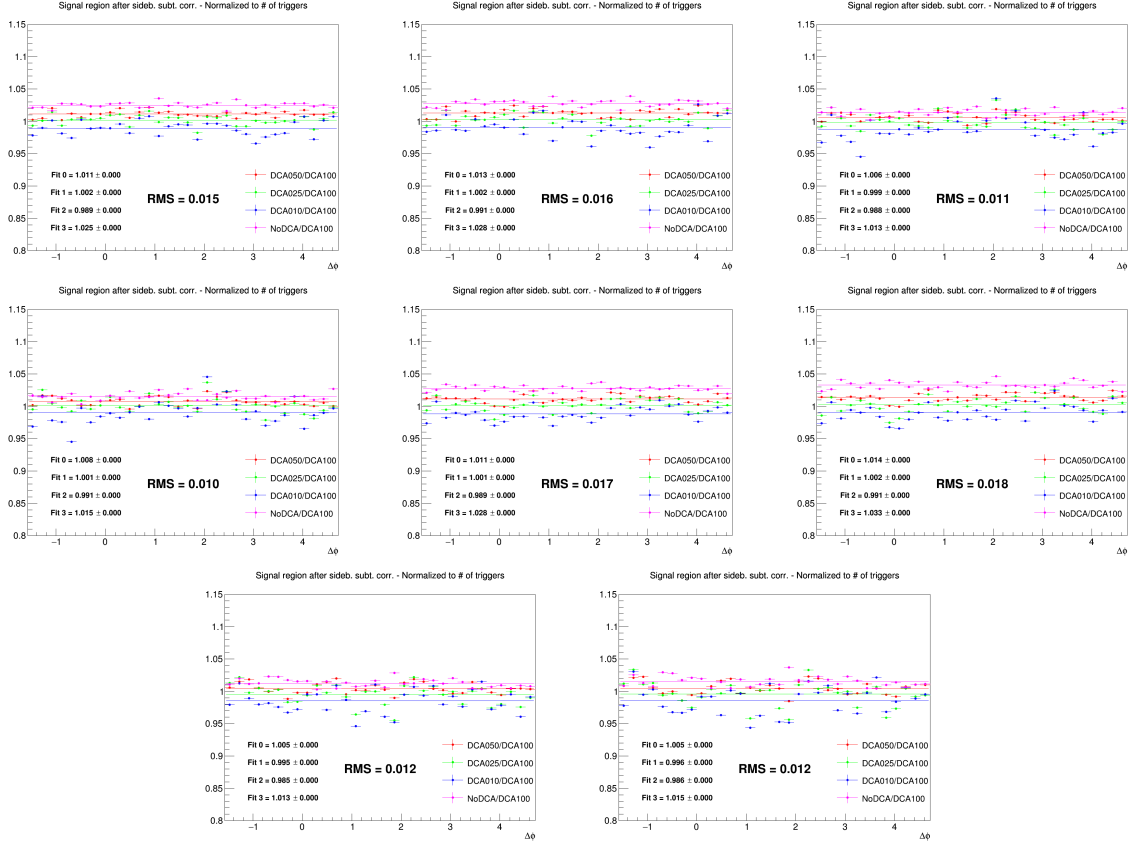


Figure 37: Ratios of correlation plots (with D^0 as trigger meson) obtained with different associated DCA selections, after purity correction. First 4 plots: $p_T(D)$ 3-5 GeV/c , next 4 plots: $p_T(D)$ 5-8 GeV/c . Each bunch of 4 plots has $p_T(\text{assoc})$ of >0.3 , $0.3-1$, >1 , $1-2 \text{ GeV}/c$, respectively.

and is quoted as a label in the plots.

The systematics uncertainties from feed-down subtraction and $B \rightarrow D$ decay topology bias, instead are $\Delta\phi$ dependent, and are hence reported as uncorrelated boxes in the plots. They do not amount to more than 4%, in every bin of all the kinematic ranges studied.

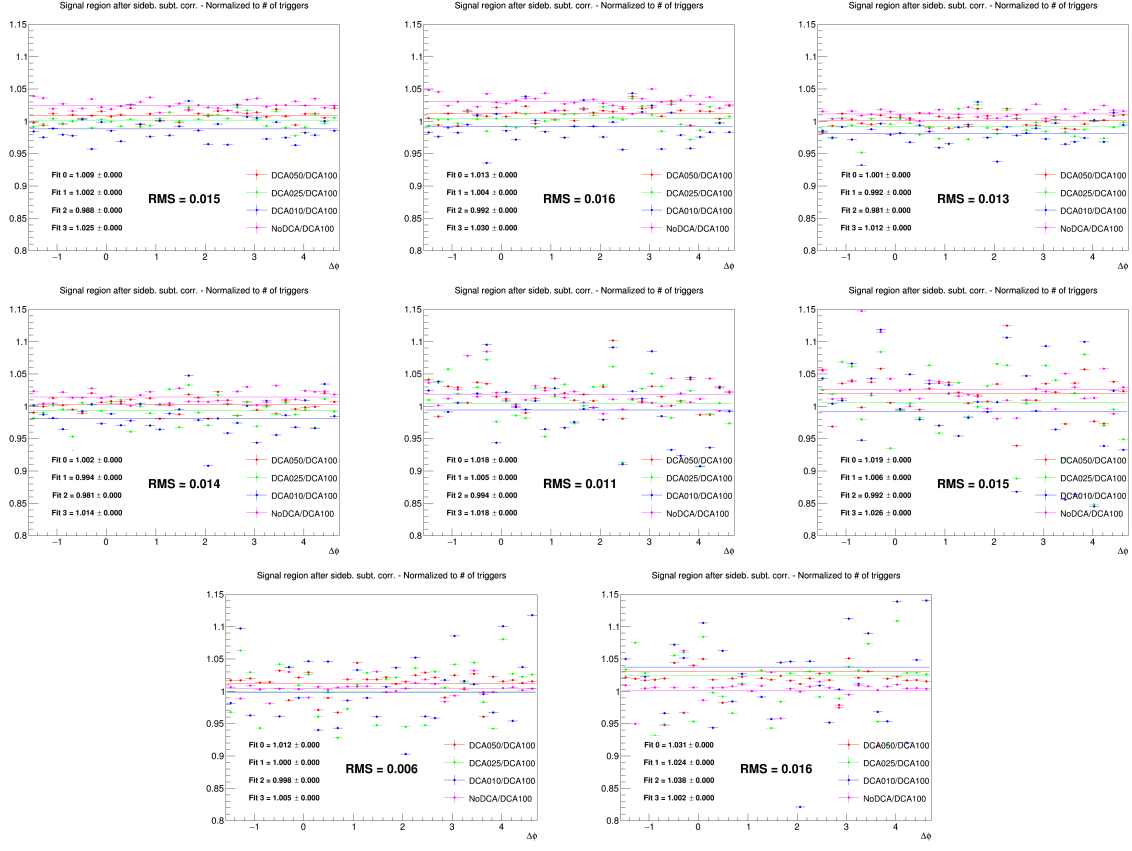


Figure 38: Ratios of correlation plots (with D^0 as trigger meson) obtained with different associated DCA selections, after purity correction. First 4 plots: $p_T(D)$ 8-16 GeV/c , next 4 plots: $p_T(D)$ 16-24 GeV/c . Each bunch of 4 plots has $p_T(\text{assoc})$ of >0.3 , $0.3-1$, >1 , $1-2 \text{ GeV}/c$, respectively.

609 5 Results

610 5.1 Comparing the three D meson correlation distributions

611 To check the compatibility of three D meson analyses, Figures 40, 41, 42, 43 show the corrected az-
 612 imuthal correlation distributions (except for the feed-down subtraction and the secondary contamination
 613 removal) for D^0 -h, D^{*+} -h and D^+ -h, in each column, on the data sample used in the analysis. Results are
 614 shown for $3 < D p_T < 5 \text{ GeV}/c$, $5 < D p_T < 8 \text{ GeV}/c$, $8 < D p_T < 16 \text{ GeV}/c$ and $16 < D p_T < 24 \text{ GeV}/c$
 615 with associated tracks $p_T > 0.3$, $p_T > 1$, $0.3 < p_T < 1 \text{ GeV}/c$, $1 < p_T < 2 \text{ GeV}/c$, $2 < p_T < 3 \text{ GeV}/c$ and
 616 $p_T > 3 \text{ GeV}/c$.

Uncertainty	$3 < p_T(D) < 5$			$5 < p_T(D) < 8$			$8 < p_T(D) < 16$			$16 < p_T(D) < 24$		
	D^0	D^+	D^*	D^0	D^+	D^*	D^0	D^+	D^*	D^0	D^+	D^*
S, B extraction	1%	1%	1.5%	1%	1%	2%	1%	1%	1.5%	1.5%	1%	3%
Bkg correl shape	1%	1%	1%	1%	1%	2%	1%	1%	1%	2%	1%	3%
D-cut stability	2.5%	1%	2%	1.5%	1%	1.5%	1.5%	2%	1%	2.5%	2%	1%

Uncertainty	$pT(\text{ass.}) > 0.3$			$0.3 < p_T < 1$			$p_T > 1$			$1 < p_T < 2$			$2 < p_T < 3$		
	D^0	D^+	D^*	D^0	D^+	D^*	D^0	D^+	D^*	D^0	D^+	D^*	D^0	D^+	D^*
Track effic.	3%	3.5%	3.5%	2.5%	2.5%	3%	4%	4%	4.5%	4%	4%	4%	4.5%	4.5%	5%
DCA stability	1.5%			2% 			1.5%			1.5%			1%		

Figure 39: Summary of the $\Delta\phi$ -correlated uncertainties associated to the correlation distributions, for three D-mesons, in the different kinematic ranges of D mesons and hadrons.

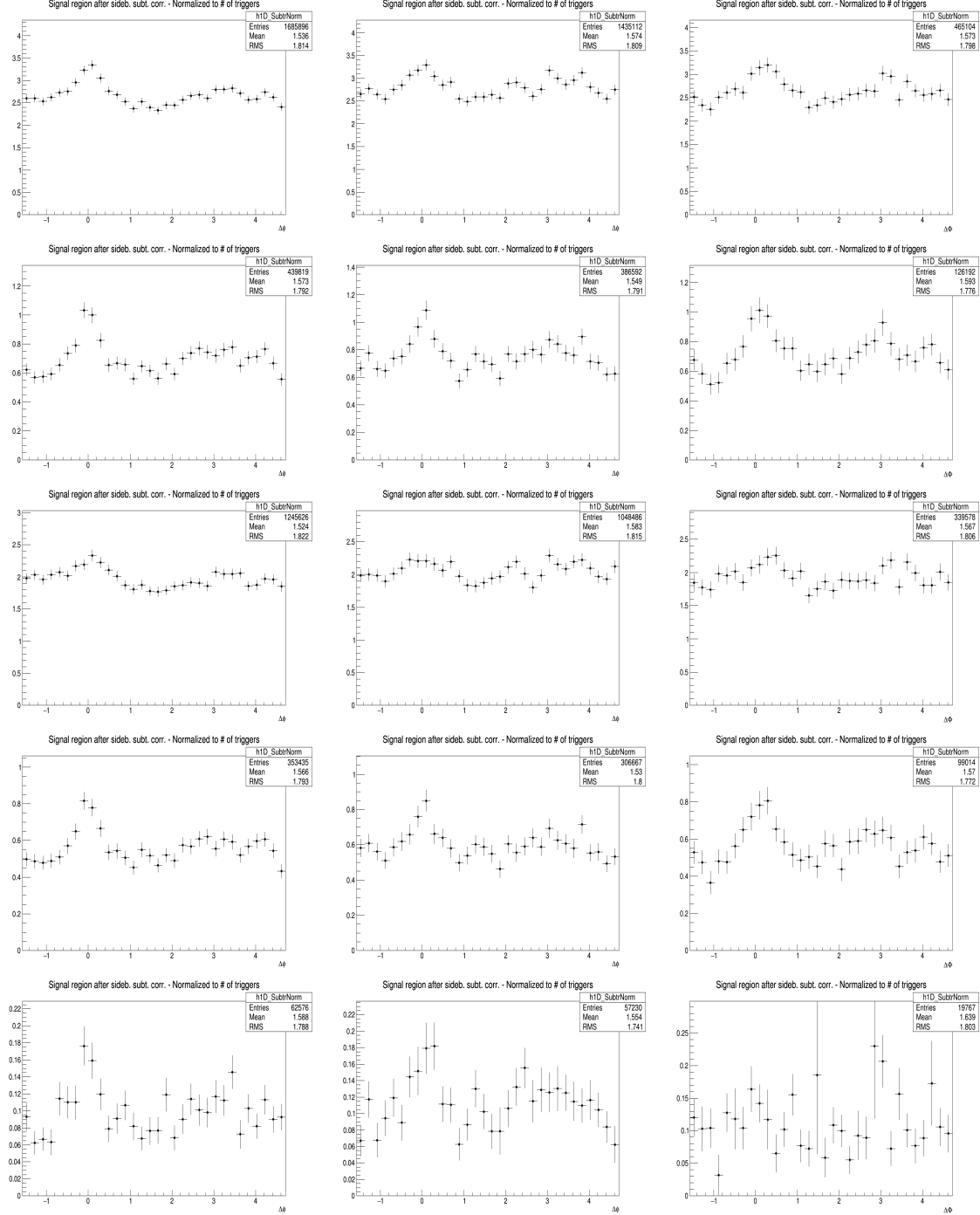


Figure 40: Corrected distribution of D-hadrons azimuthal correlations for the three species (apart from feed-down and purity), from analysis on the data sample, for the analyzed D-meson (**Column-Left:** D^0 , **Column-Middle:** D^+ and **Column-Right:** D^{*+}) and different associated tracks p_T ranges (**Row 1-5:** $3 < Dp_T < 5 \text{ GeV}/c$, $p_T(\text{Assoc}) > 0.3$, > 1.0 , $0.3-1.0$, $1.0-2.0$ and $2.0-3.0 \text{ GeV}/c$ respectively)

5.1 Comparing the three D meson correlation distributions

59

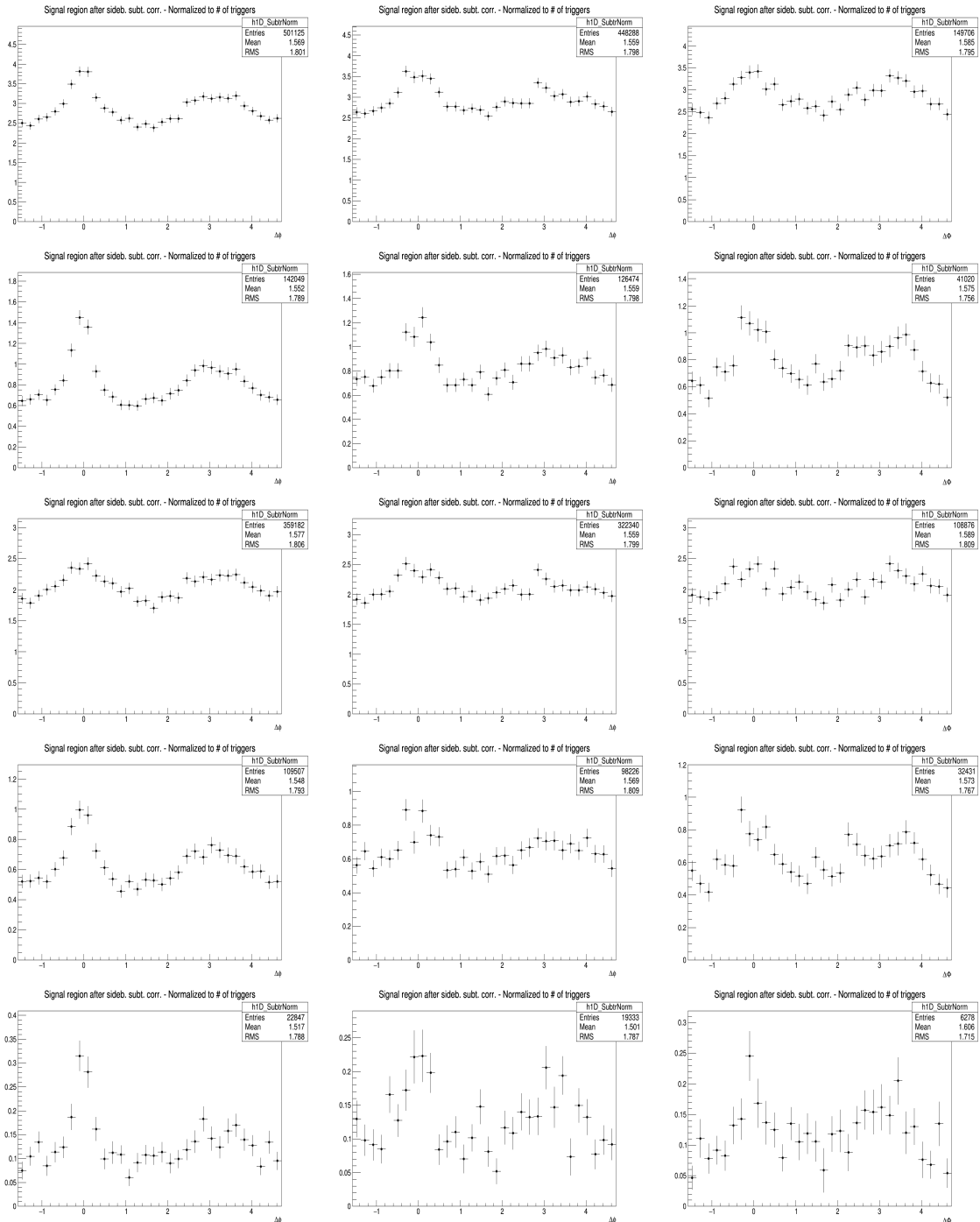


Figure 41: Corrected distribution of D-hadrons azimuthal correlations for the three species (apart from feed-down and purity), from analysis on the data sample, for the analyzed D-meson (**Column-Left: D^0 , Column-Middle: D^+ and Column-Right: D^{*+}**) and different associated tracks p_T ranges (**Row 1-5: $5 < Dp_T < 8 \text{ GeV}/c$, $p_T(\text{Assoc}) > 0.3, > 1.0, 0.3-1.0, 1.0-2.0$ and $2.0-3.0 \text{ GeV}/c$ respectively**)

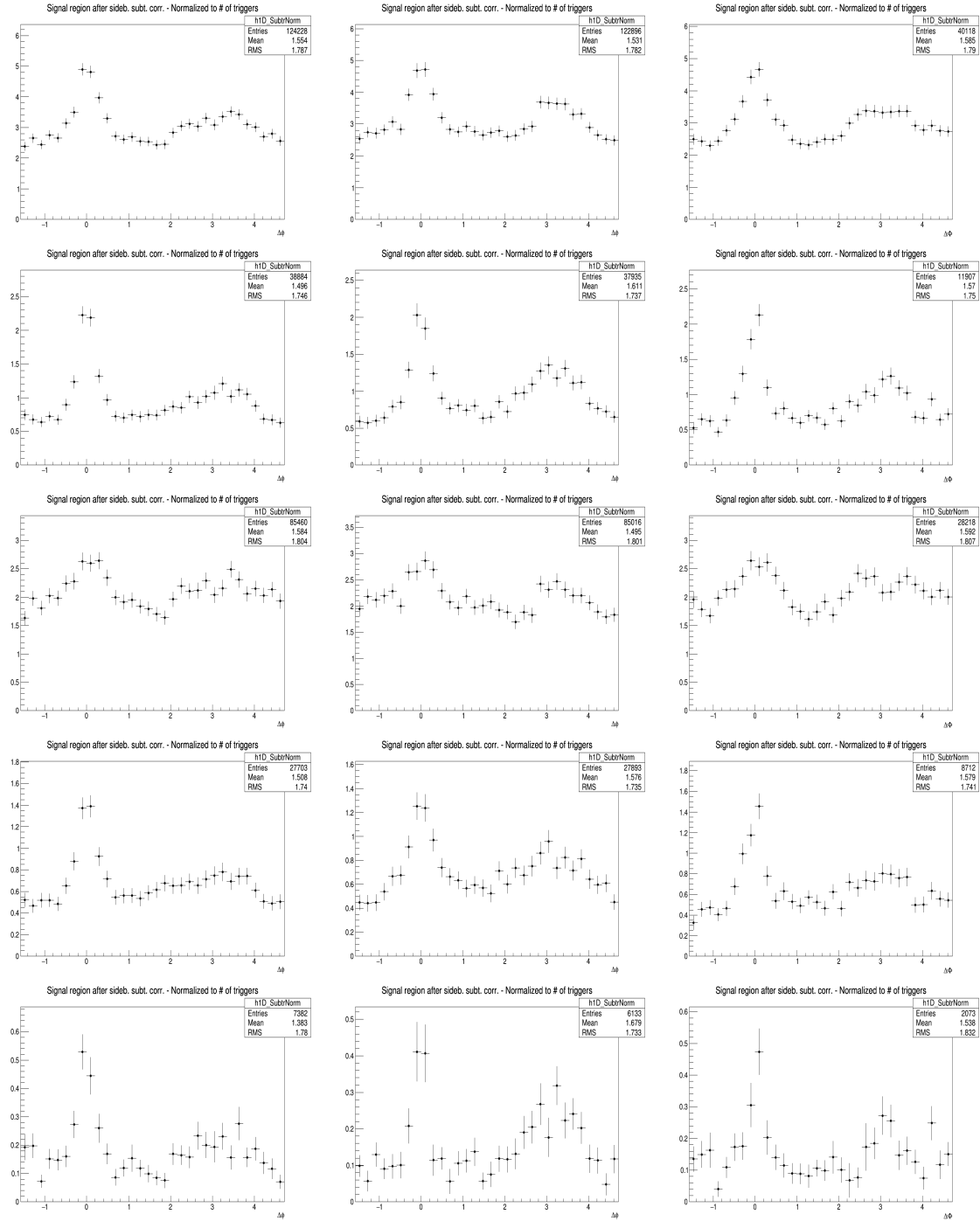


Figure 42: Corrected distribution of D-hadrons azimuthal correlations for the three species (apart from feed-down and purity), from analysis on the data sample, for the analyzed D-meson (**Column-Left:** D^0 , **Column-Middle:** D^+ and **Column-Right:** D^{*+}) and different associated tracks p_T ranges (**Row 1-5:** $8 < Dp_T < 16$ GeV/ c , p_T (Assoc) $> 0.3, > 1.0, 0.3-1.0, 1.0-2.0$ and $2.0-3.0$ GeV/ c respectively)

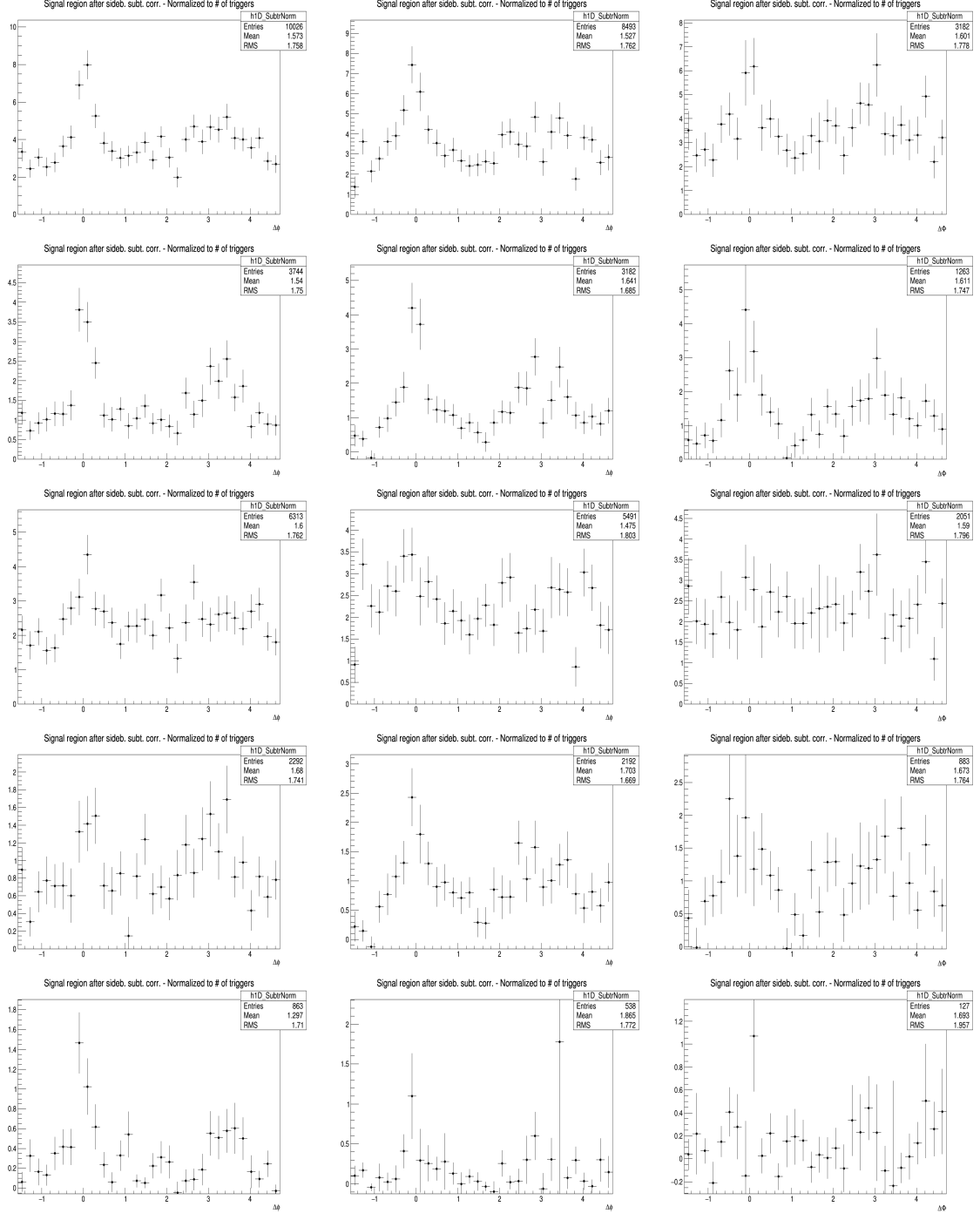


Figure 43: Corrected distribution of D-hadrons azimuthal correlations for the three species (apart from feed-down and purity), from analysis on the data sample, for the analyzed D-meson (**Column-Left:** D^0 , **Column-Middle:** D^+ and **Column-Right:** D^{*+}) and different associated tracks p_T ranges (**Row 1-5:** $16 < Dp_T < 24 \text{ GeV}/c$, $p_T(\text{Assoc}) > 0.3$, > 1.0 , $0.3-1.0$, $1.0-2.0$ and $2.0-3.0 \text{ GeV}/c$ respectively)

617 An agreement of the distributions from the three mesons within the uncertainties is found in all the
618 kinematic ranges.

619 Despite being evaluated in the full 2π range, the range of final results was then reduced to $[0, \pi]$ radians,
620 reflecting the points outside that range over the value of 0. This allowed to reduce the impact of statistical
621 fluctuations on the data points (supposing equal statistics for a pair of symmetric bins, after the reflection
622 the relative statistical uncertainty for the resulting bin is reduced by a factor $1/\sqrt{2}$).

623 5.2 Average of D^0 , D^+ and D^{*+} results

624 Given the compatibility within the uncertainties among the D^0 , D^+ and D^{*+} azimuthal correlations, and
625 since no large differences are visible in the correlation distributions observed in Monte Carlo simulations
626 based on Pythia with Perugia0, 2010 and 2011 tunes¹, it was possible to perform a weighted average
627 (eq. 5) of the azimuthal correlation distributions of D^0 , D^+ and D^{*+} , in order to reduce the overall
628 uncertainties. Although some correlation between the mesons could be present (about the 30% of the
629 D^0 , and also part of the D^+ , come from D^{*+} decays), the three selected D-meson samples can be treated
630 as uncorrelated. The sum of the statistical uncertainties; the systematics uncertainty on S and B extraction
631 and on background shape, are added in quadrature and the inverse of this sum was used as weight, w_i .

$$\left\langle \frac{1}{N_D} \frac{dN_{\text{assoc}}}{dp_T} \right\rangle_{D_{\text{mesons}}} = \frac{\sum_{i=\text{meson}} w_i \frac{1}{N_D} \frac{dN_i^{\text{assoc}}}{d\Delta\phi}}{\sum_{i=\text{meson}} w_i}, w_i = \frac{1}{\sigma_{i,\text{stat}}^2 + \sigma_{i,\text{uncorr.syst}}^2} \quad (5)$$

632 The statistical uncertainty and the uncertainties on S and B extraction and on background shape (those
633 used for the weights) on the average were then recalculated using the following formula:

$$\sigma^2 = \frac{1}{n_D} \frac{\sum_{i=\text{meson}} w_i \sigma_i^2}{\sum_{i=\text{meson}} w_i} \quad (6)$$

634 where n_D is the number of mesons considered in the average. It can be observed that for $\sigma_i^2 = 1/w_i$ the
635 formula coincides with the standard one giving the uncertainty on a weighted average. The contribution
636 to the average systematic uncertainty for those uncertainty sources not included in the weight definition,
637 was evaluated via error propagation on the formula of the weighted average (5), resulting in equation
638 (7) and (8) for sources considered uncorrelated and correlated among the mesons. In particular, the
639 uncertainties on the associated track reconstruction efficiency, on the contamination from secondary, on
640 the feed-down subtraction, and that resulting from the Monte Carlo closure test were considered fully
641 correlated among the mesons, while those deriving from the yield extraction (included in the weight
642 definition) and on the D meson reconstruction and selection efficiency were treated as uncorrelated.

$$\sigma^2 = \frac{\sum_{i=\text{meson}} w_i^2 \sigma_i^2}{(\sum_{i=\text{meson}} w_i)^2} \quad (7)$$

$$\sigma = \frac{\sum_{i=\text{meson}} w_i \sigma_i}{\sum_{i=\text{meson}} w_i} \quad (8)$$

643 Figures 44, 45, 46, 47 show the averages of the azimuthal correlation distributions of D^0 , D^+ and D^{*+}
644 and charged particles with $p_T > 0.3 \text{ GeV}/c$, $0.3 < p_T < 1 \text{ GeV}/c$, $p_T > 1 \text{ GeV}/c$, $1 < p_T < 2 \text{ GeV}/c$, $2 <$
645 $p_T < 3 \text{ GeV}/c$ in the D meson p_T ranges $3 < p_T < 5 \text{ GeV}/c$, $5 < p_T < 8 \text{ GeV}/c$, $8 < p_T < 16 \text{ GeV}/c$ and
646 $16 < p_T < 24 \text{ GeV}/c$. As expected, a rising trend of the height of the near-side peak with increasing D-
647 meson p_T is observed, together with a decrease of the baseline level with increasing p_T of the associated

¹A slight near side hierarchy is present among the three meson results, with D^{*+} meson having a lower peak amplitude than D^0 and D^+ . It was verified that this is induced by the presence of D^0 and D^+ mesons coming from D^{*+} , the latter having on average a larger p_T and coming, hence, on average, from a larger p_T quark parton, which fragments in slightly more tracks in the near-side.

648 tracks. To further increase the statistical precision on the averaged correlation distributions, given the
649 symmetry around 0 on the azimuthal axis, the distributions were reflected and shown in the range $[0, \pi]$.
650 This reduces the statistical uncertainty on the points by, approximately, a factor of $1/\sqrt{2}$.

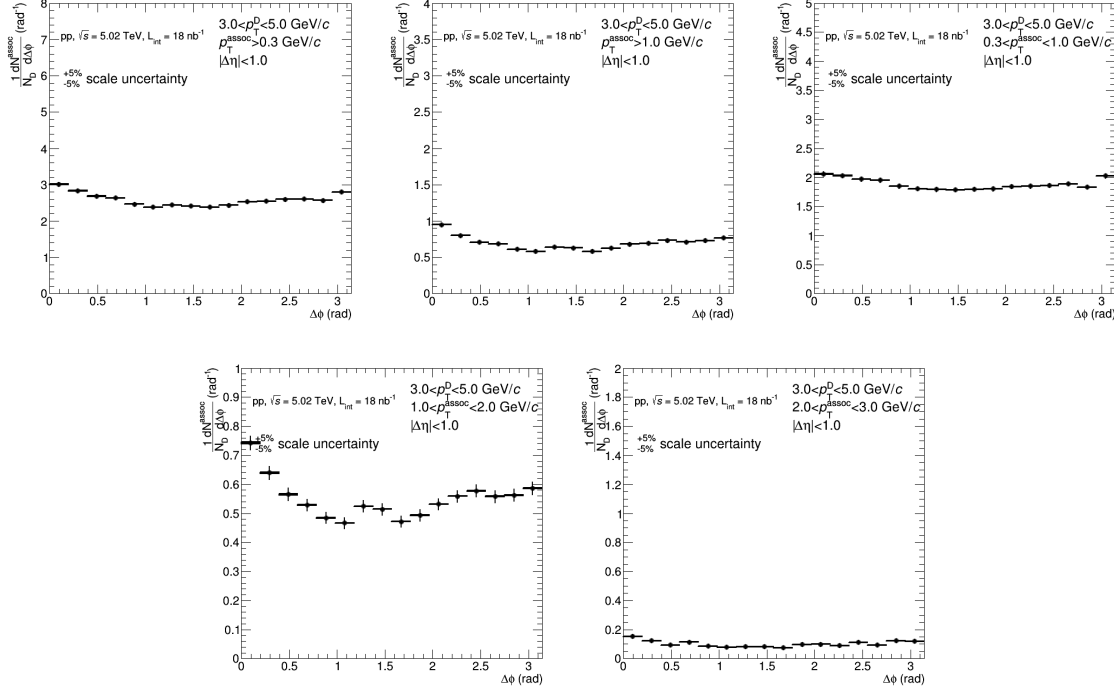


Figure 44: Average of D^0 , D^+ and D^{*+} azimuthal correlation distributions, in the D meson p_T range $3 < p_T < 5$ GeV/ c with associated tracks with $p_T > 0.3$ GeV/ c , $p_T > 1$ GeV/ c , $0.3 < p_T < 1$ GeV/ c , $1 < p_T < 2$ GeV/ c and $2 < p_T < 3$ GeV/ c

651 The usage of weighted average requires, as an underlying assumption, identical results expected for
 652 different species (or, at least, compatible within the uncertainties). Anyway, it was also verified that the
 653 usage of the arithmetic average instead of the weighted average increases the uncertainties on the points,
 654 but produces a negligible shift of their central values.

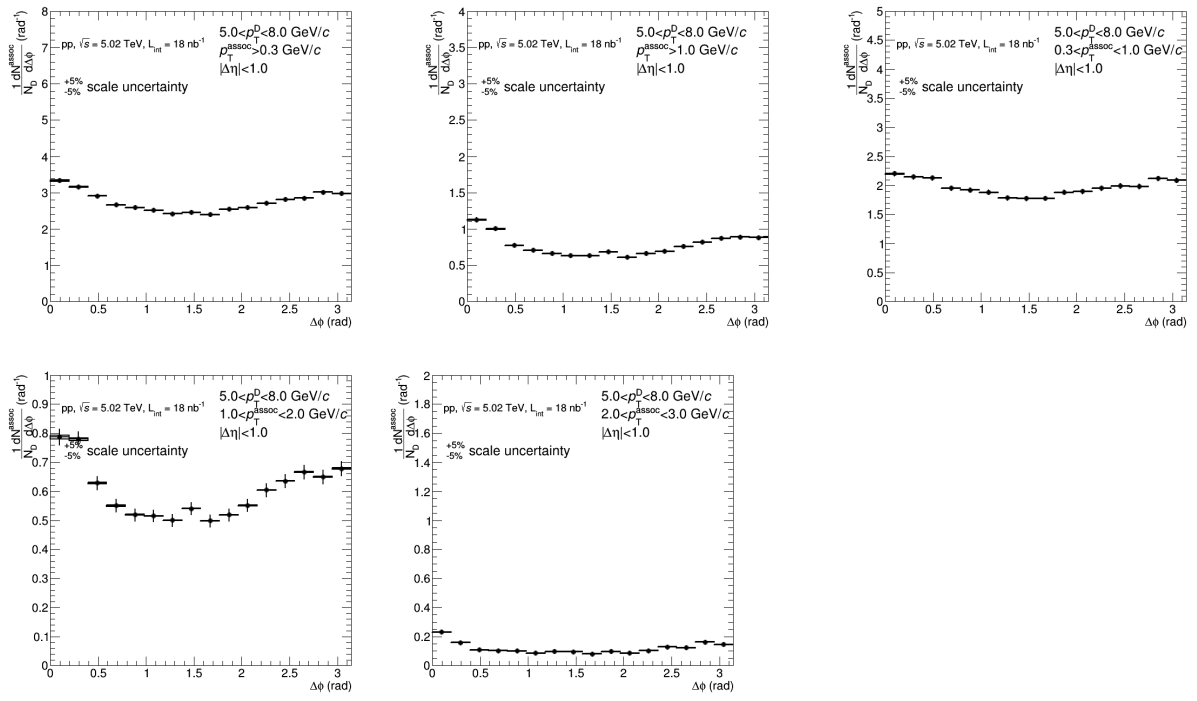


Figure 45: Average of D^0 , D^+ and D^{*+} azimuthal correlation distributions, in the D meson p_T range $5 < p_T < 8 \text{ GeV}/c$ with associated tracks with $p_T > 0.3 \text{ GeV}/c$, $p_T > 1 \text{ GeV}/c$, $0.3 < p_T < 1 \text{ GeV}/c$, $1 < p_T < 2 \text{ GeV}/c$ and $2 < p_T < 3 \text{ GeV}/c$

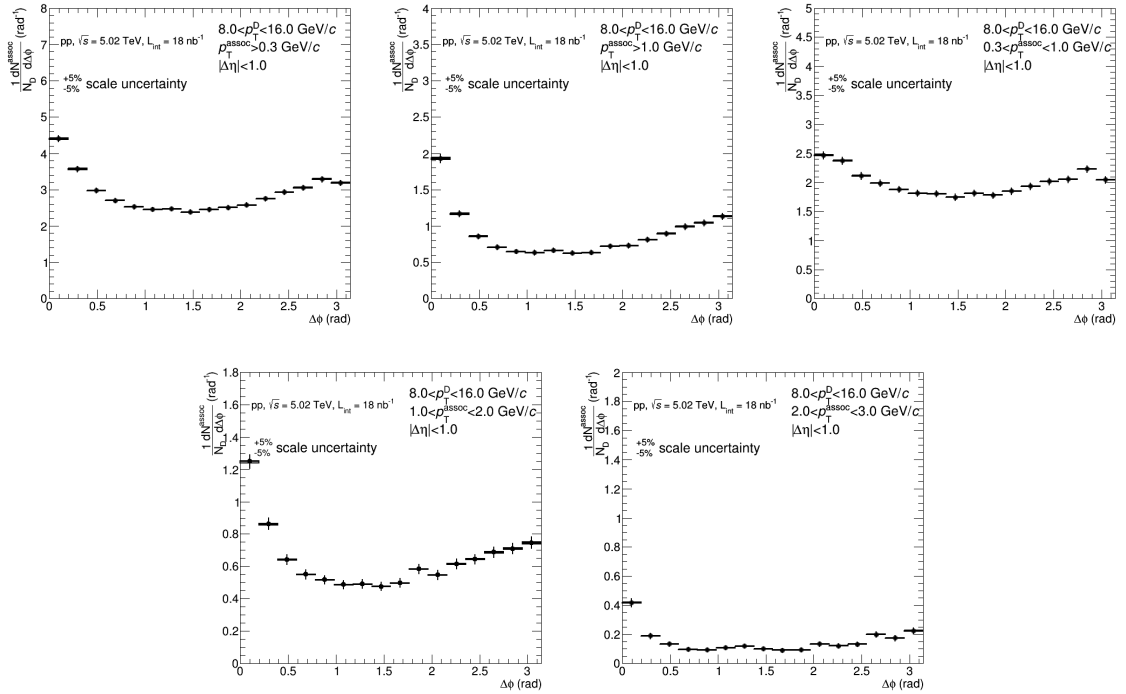


Figure 46: Average of D^0 , D^+ and D^{*+} azimuthal correlation distributions, in the D meson p_T range $8 < p_T < 16 \text{ GeV}/c$ with associated tracks with $p_T > 0.3 \text{ GeV}/c$, $p_T > 1 \text{ GeV}/c$, $0.3 < p_T < 1 \text{ GeV}/c$, $1 < p_T < 2 \text{ GeV}/c$ and $2 < p_T < 3 \text{ GeV}/c$

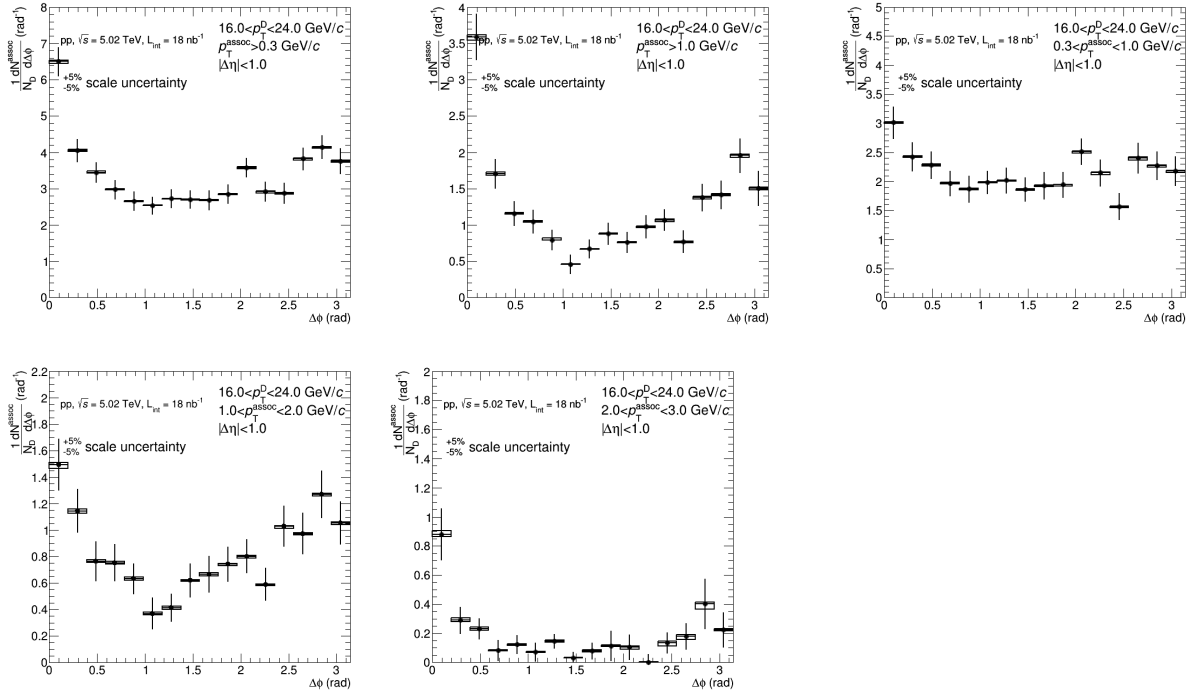


Figure 47: Average of D^0 , D^+ and D^{*+} azimuthal correlation distributions, in the D meson p_T range $16 < p_T < 24 \text{ GeV}/c$, with associated tracks with $p_T > 0.3 \text{ GeV}/c$, $p_T > 1 \text{ GeV}/c$, $0.3 < p_T < 1 \text{ GeV}/c$, $1 < p_T < 2 \text{ GeV}/c$ and $2 < p_T < 3 \text{ GeV}/c$

655 **5.3 Fit of correlation distributions and observables**

656 In order to extract quantitative and physical information from the data correlation patterns, the averaged
 657 D-h correlation distributions are fitted with two Gaussian functions (with means fixed at $\Delta\varphi=0$ and $\Delta\varphi=\pi$
 658 values), plus a constant term (baseline). A periodicity condition is also applied to the fit function to obtain
 659 the same value at the bounds of 2π range. The expression of the fit function is reported below (equation
 660 9):

$$f(\Delta\varphi) = c + \frac{Y_{NS}}{\sqrt{2\pi}\sigma_{NS}} e^{-\frac{(\Delta\varphi-\mu_{NS})^2}{2\sigma_{NS}^2}} + \frac{Y_{AS}}{\sqrt{2\pi}\sigma_{AS}} e^{-\frac{(\Delta\varphi-\mu_{AS})^2}{2\sigma_{AS}^2}} \quad (9)$$

661 where baseline is calculated as the weighted average of the points lying in the so-called "transverse
 662 region", i.e. the interval $\frac{\pi}{4} < |\Delta\varphi| < \frac{\pi}{2}$.

663 Results from the fit for the studied kinematical regions are shown in Figures 48, 49, 50, 51, 52, displaying
 664 also the values of near-side and away-side peak yields (the Gaussian integrals) and widths (the σ of the
 665 two Gaussians).

666 From the fit outcome, it is possible to retrieve the near-side and away-side yield and widths (integral
 667 and sigma of the Gaussian functions, respectively), as well as the baseline height of the correlation
 668 distribution. The near-side observables give information on the multiplicity and angular spread of the
 669 tracks from the fragmentation of the charm jet which gave birth to the D-meson trigger. At first order,
 670 instead, the away-side observables are related to the hadronization of the charm parton produced in the
 671 opposite direction (though the presence of NLO processes for charm production breaks the full validity
 672 of this assumption). The baseline value is a rough indicator of the underlying event multiplicity, though
 673 below the baseline level also charm and beauty-related pairs are contained (especially in cases of NLO
 674 production for the heavy quarks).

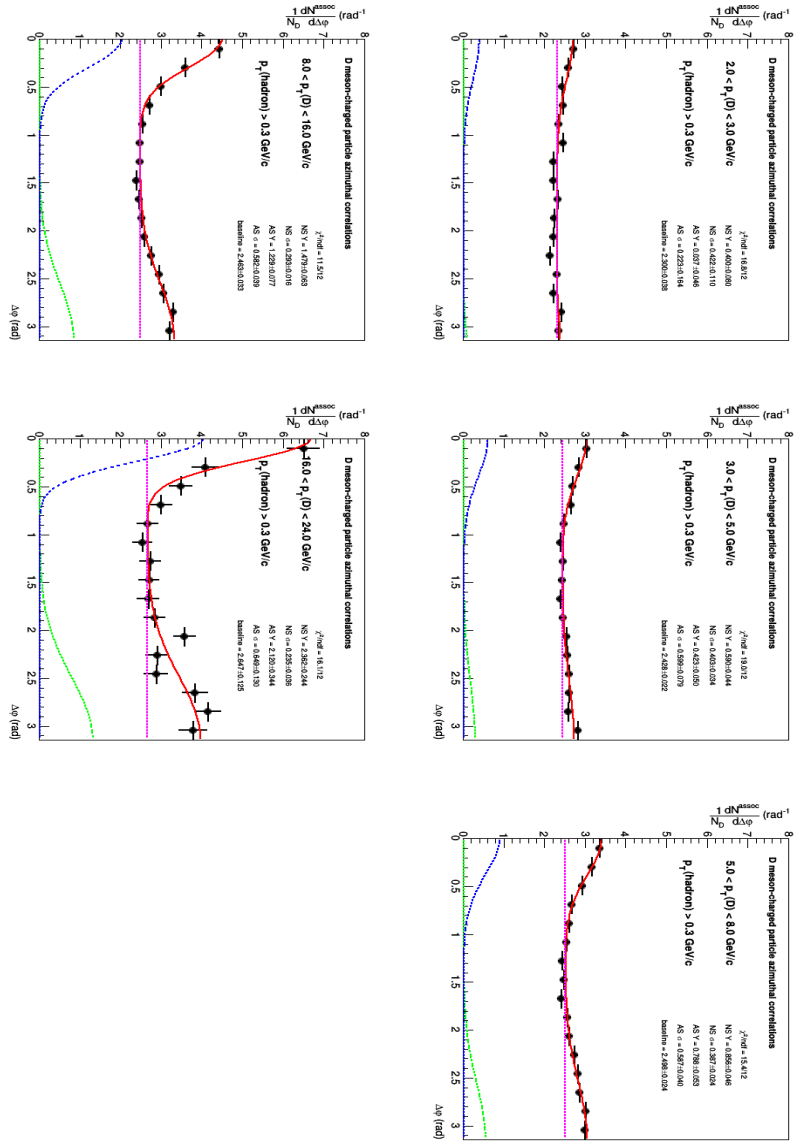


Figure 48: Fits to azimuthal correlation distributions and baseline estimation. The set of five panels is for $p_T > 0.3 \text{ GeV}/c$. The corresponding p_T ranges of D-mesons are reported in each panel.

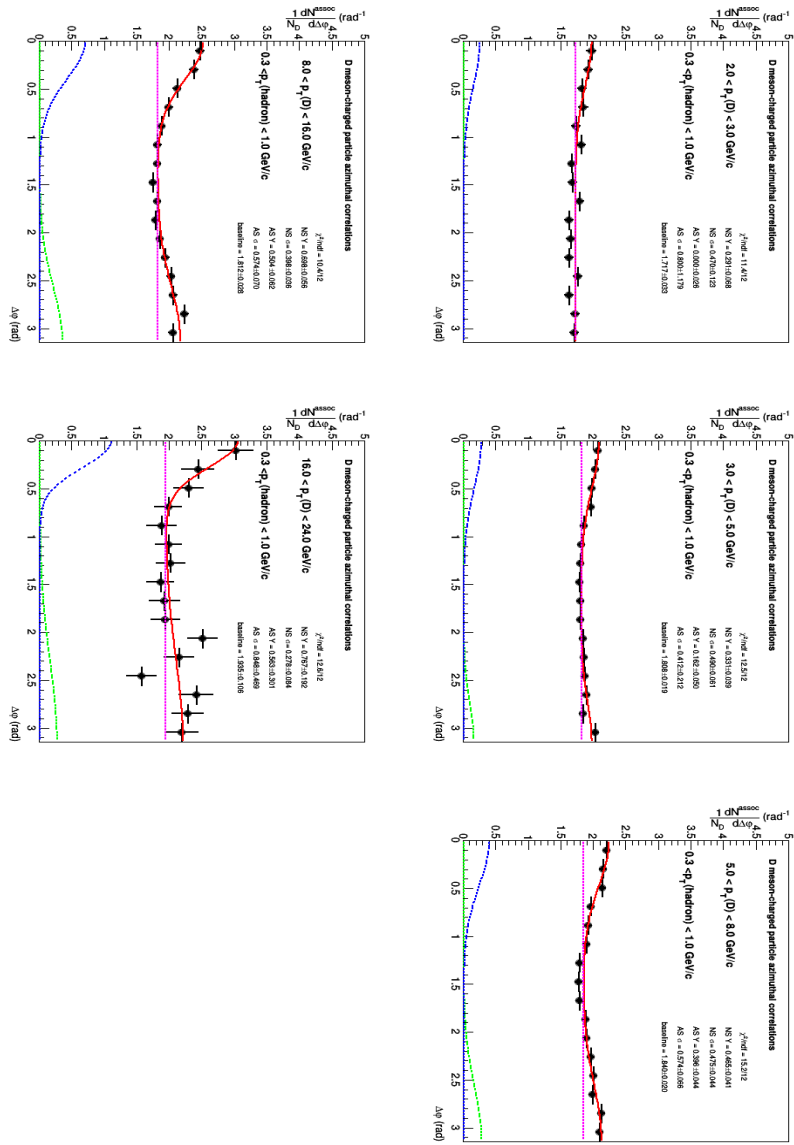


Figure 49: Fits to azimuthal correlation distributions and baseline estimation. The set of five panels is for $0.3 < p_T < 1 \text{ GeV}/c$. The corresponding p_T ranges of D-mesons are reported in each panel.

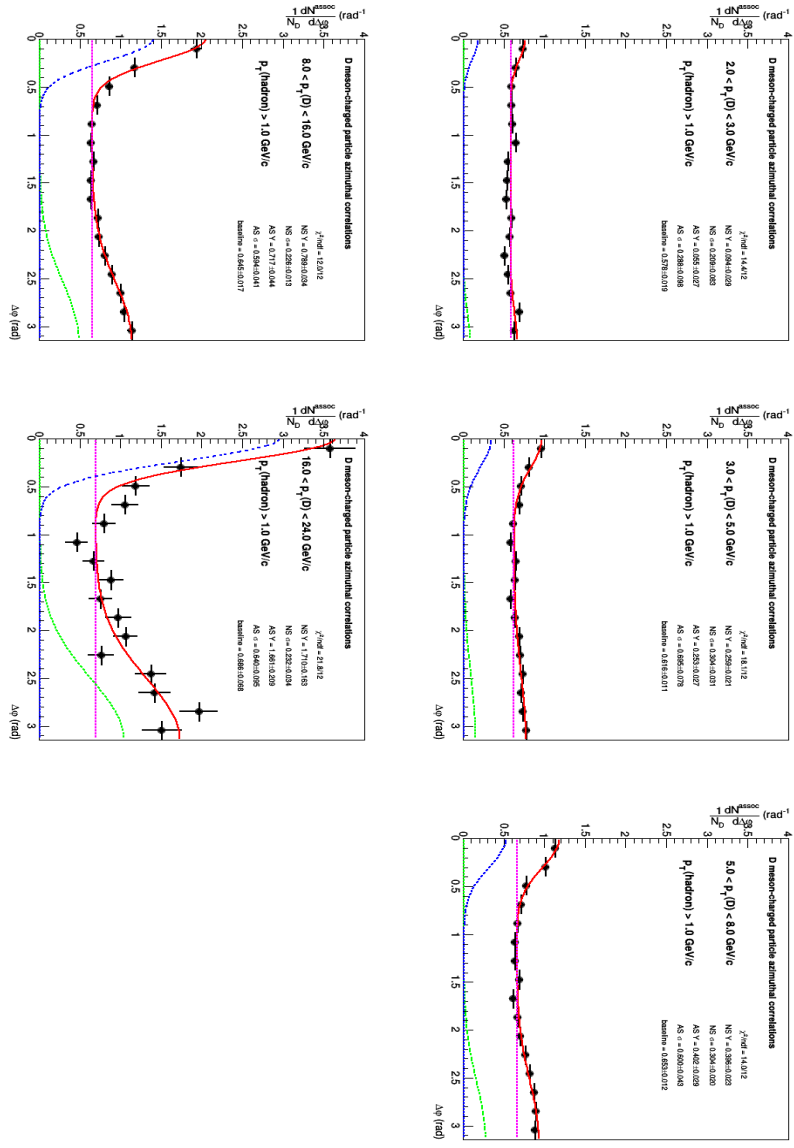


Figure 50: Fits to azimuthal correlation distributions and baseline estimation. The set of five panels is for $p_T > 1$ GeV/c. The corresponding p_T ranges of D-mesons are reported in each panel.

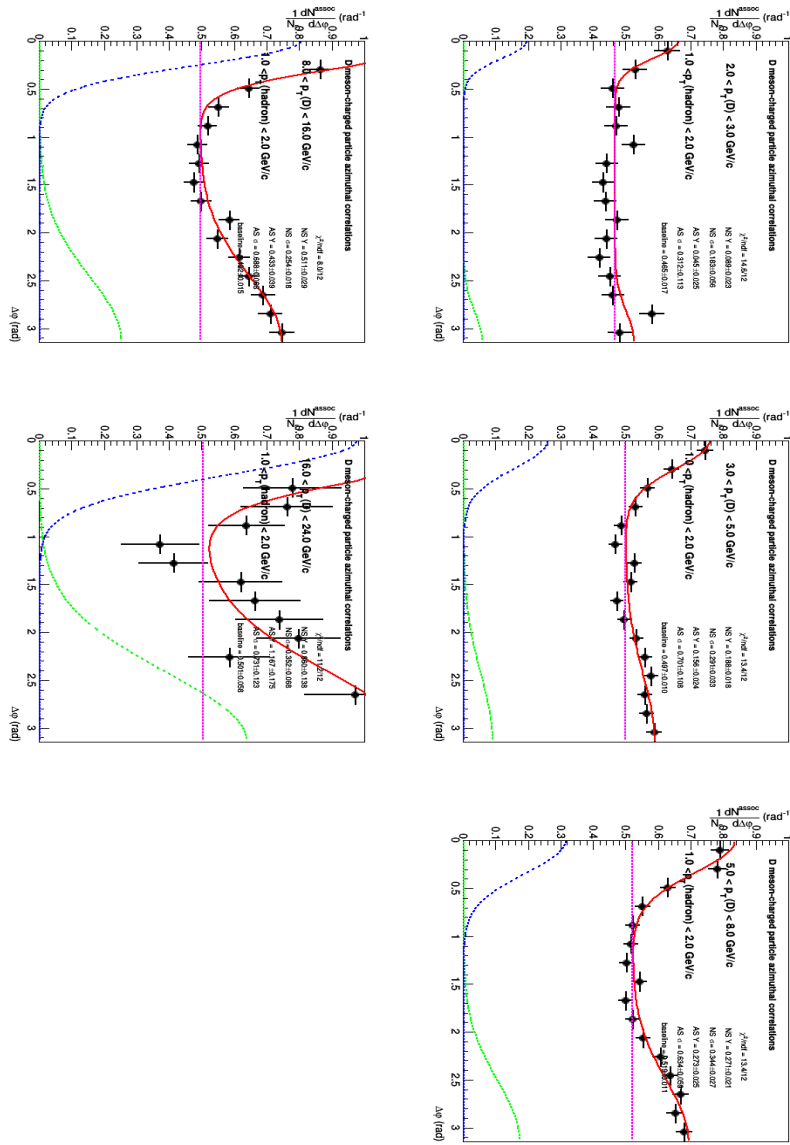


Figure 51: Fits to azimuthal correlation distributions and baseline estimation. The set of five panels is for $1 < p_T < 2 \text{ GeV}/c$. The corresponding p_T ranges of D-mesons are reported in each panel.

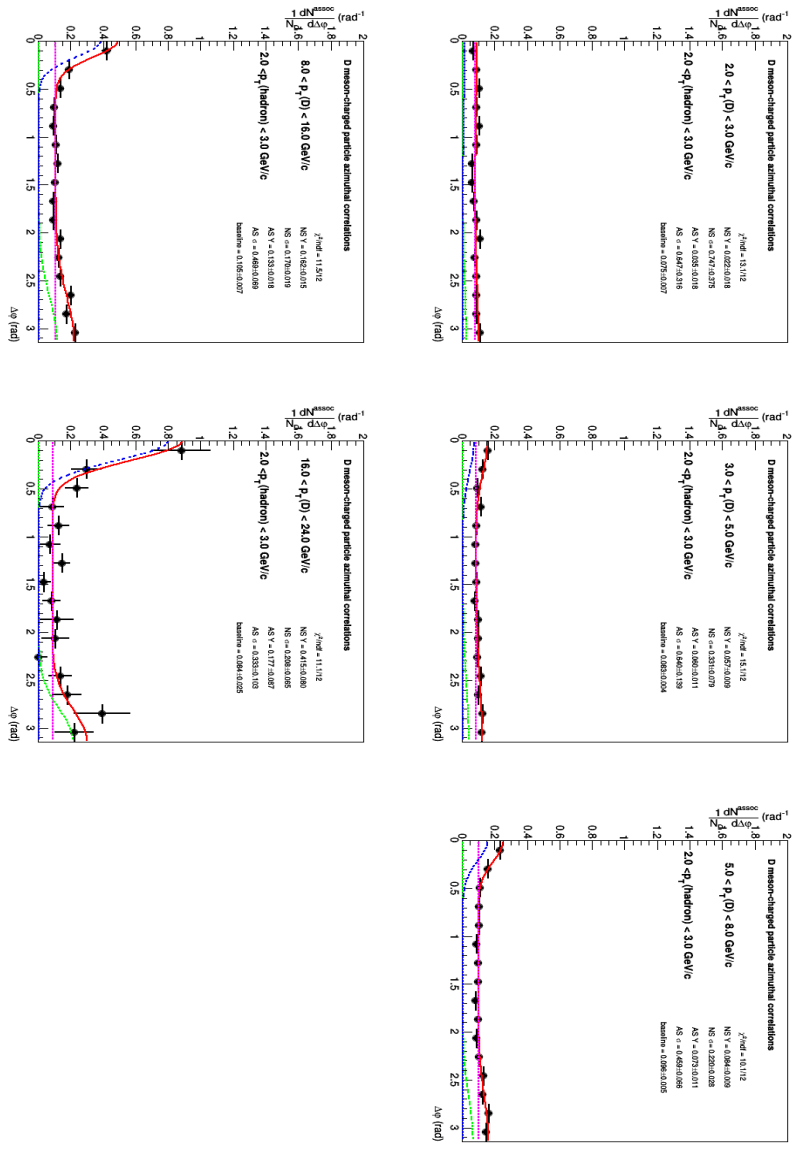


Figure 52: Fits to azimuthal correlation distributions and baseline estimation. The set of five panels is for $2 < p_T < 3$ GeV/ c . The corresponding p_T ranges of D-mesons are reported in each panel.

675 **5.3.1 Generalized Gaussian for near-side peak**

676 As it can be observed in Figures 48, 49, 50, 51, 52, at high transverse momentum of the D-meson and of
 677 the associated track the tails of the near-side peak are always underestimated by the fitting function, if a
 678 standard Gaussian is employed for fitting the near-side (and, in general, the shape of the peak seems not
 679 well described by a Gaussian).

680 To dig into this issue, an alternate fitting function was adopted for the near-side peak fitting, i.e. the
 681 generalized Gaussian function 53, with PDF:

$$f(\Delta\phi) = \frac{\beta}{2\alpha\Gamma(1/\beta)} \cdot e^{-(|x-\mu|/\alpha)^\beta} \quad (10)$$

682 and having as variance $\frac{\alpha\Gamma(3/\beta)}{\Gamma(1/\beta)}$. The square root of the variance was used as near-side width fit observable
 683 instead of the Gaussian σ , together with the integral of the fitting function, which defines the near-side
 684 yield.

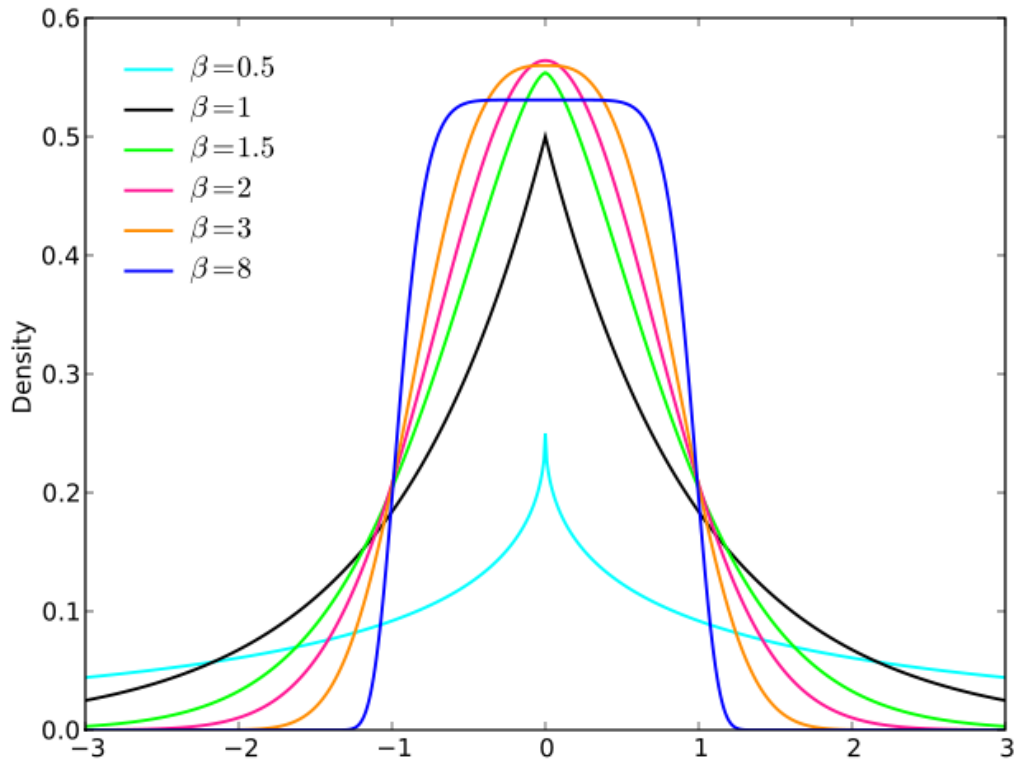


Figure 53: Generalized Gaussian function for different β parameter values.

685 In Figs 54, 55, 56, 57, 58, the fit of all the kinematic regions using the generalized Gaussian in the near-
 686 side region are reported (to be compared with Figs. 48, 49, 50, 51, 52). As it can be seen, the near-side
 687 yields remain very similar in the two approaches, apart from an increase of the yields up to 10% in 16-24
 688 GeV/c. The widths are generally comparable at low p_T of the D-meson, then increase in the generalized
 689 Gaussian case from 8 GeV/c onwards, up to about a 20% difference. Anyway, one shall consider that
 690 the width has not the same interpretation for the two fitting functions (there's no probabilistic meaning
 691 for the width in the case of generalized Gaussian).

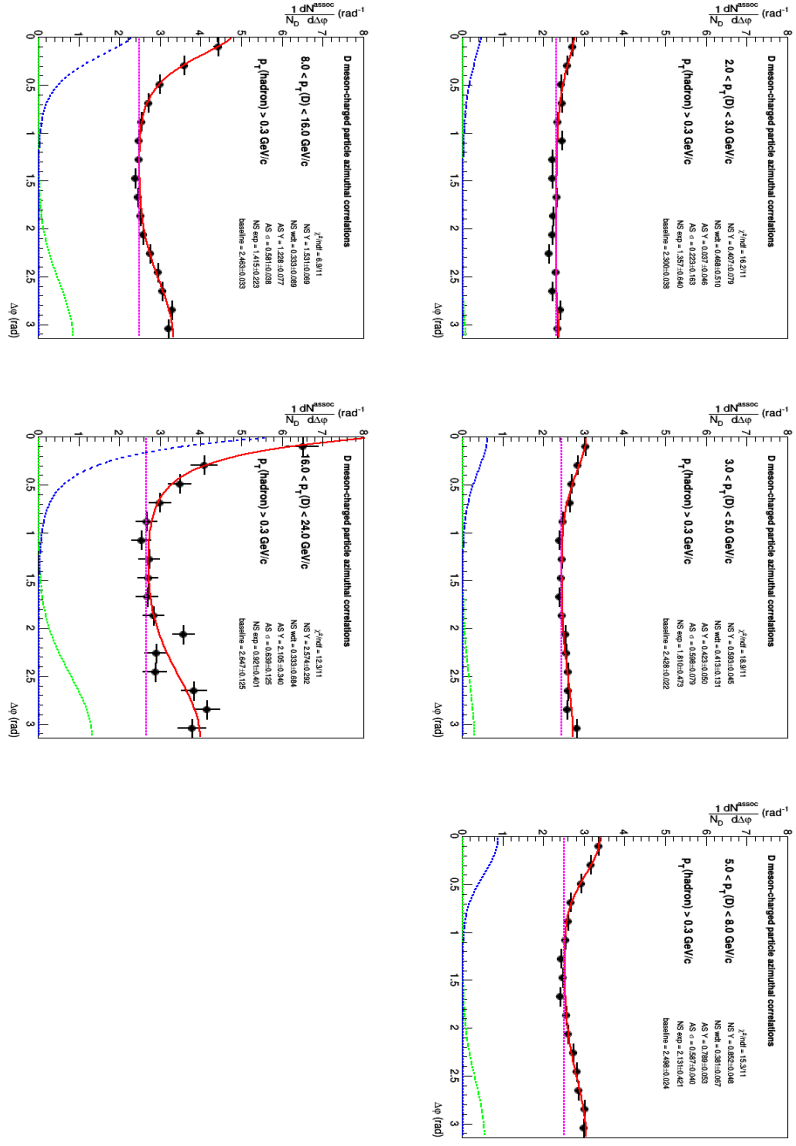


Figure 54: Fits to azimuthal correlation distributions and baseline estimation, with the generalized Gaussian for the near-side peak. The set of five panels is for $p_T > 0.3 \text{ GeV}/c$. The corresponding p_T ranges of D-mesons are reported in each panel.

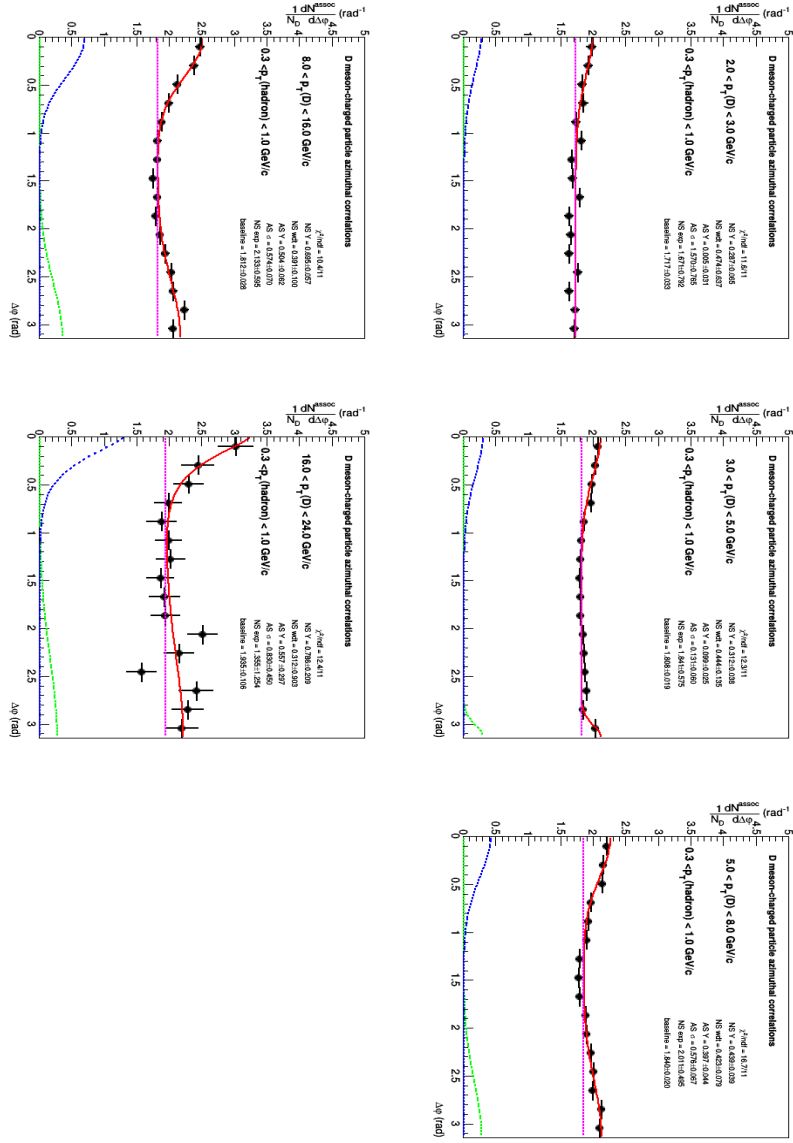


Figure 55: Fits to azimuthal correlation distributions and baseline estimation, with the generalized Gaussian for the near-side peak. The set of five panels is for $0.3 < p_T < 1$ GeV/c. The corresponding p_T ranges of D-mesons are reported in each panel.

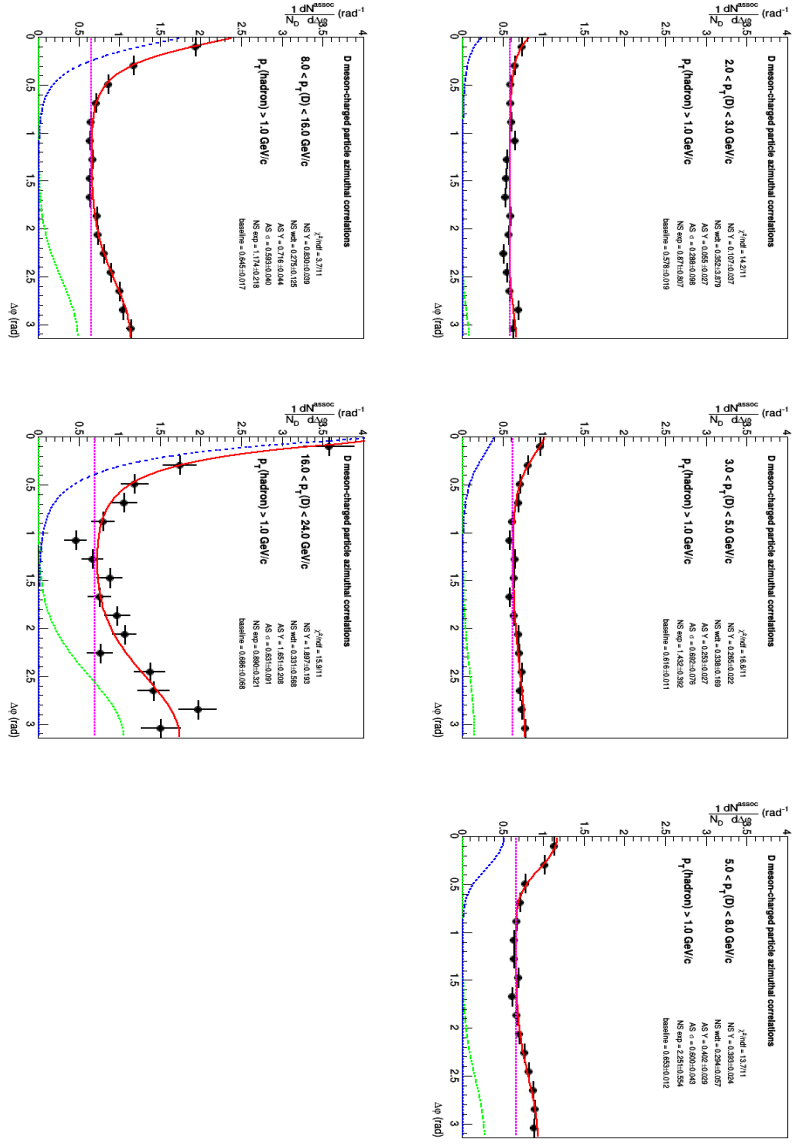


Figure 56: Fits to azimuthal correlation distributions and baseline estimation, with the generalized Gaussian for the near-side peak. The set of five panels is for $p_T > 1$ GeV/c. The corresponding p_T ranges of D-mesons are reported in each panel.

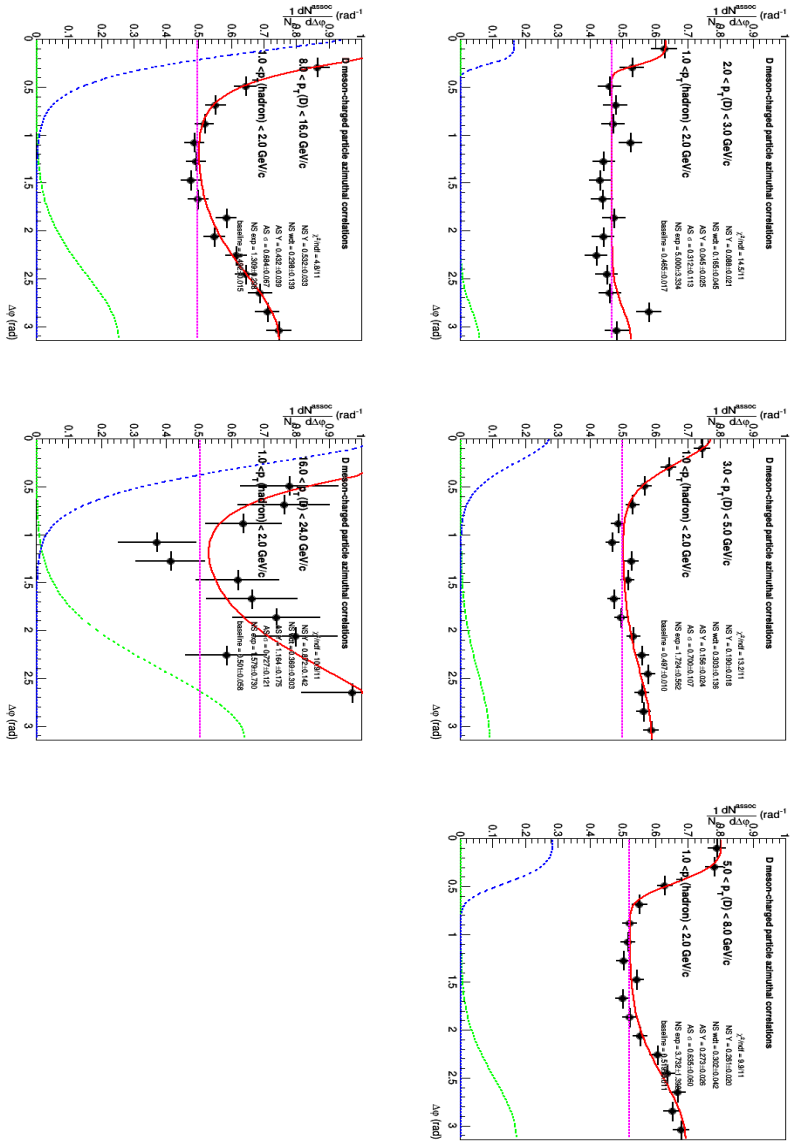


Figure 57: Fits to azimuthal correlation distributions and baseline estimation, with the generalized Gaussian for the near-side peak. The set of five panels is for $1 < p_T < 2 \text{ GeV}/c$. The corresponding p_T ranges of D-mesons are reported in each panel.

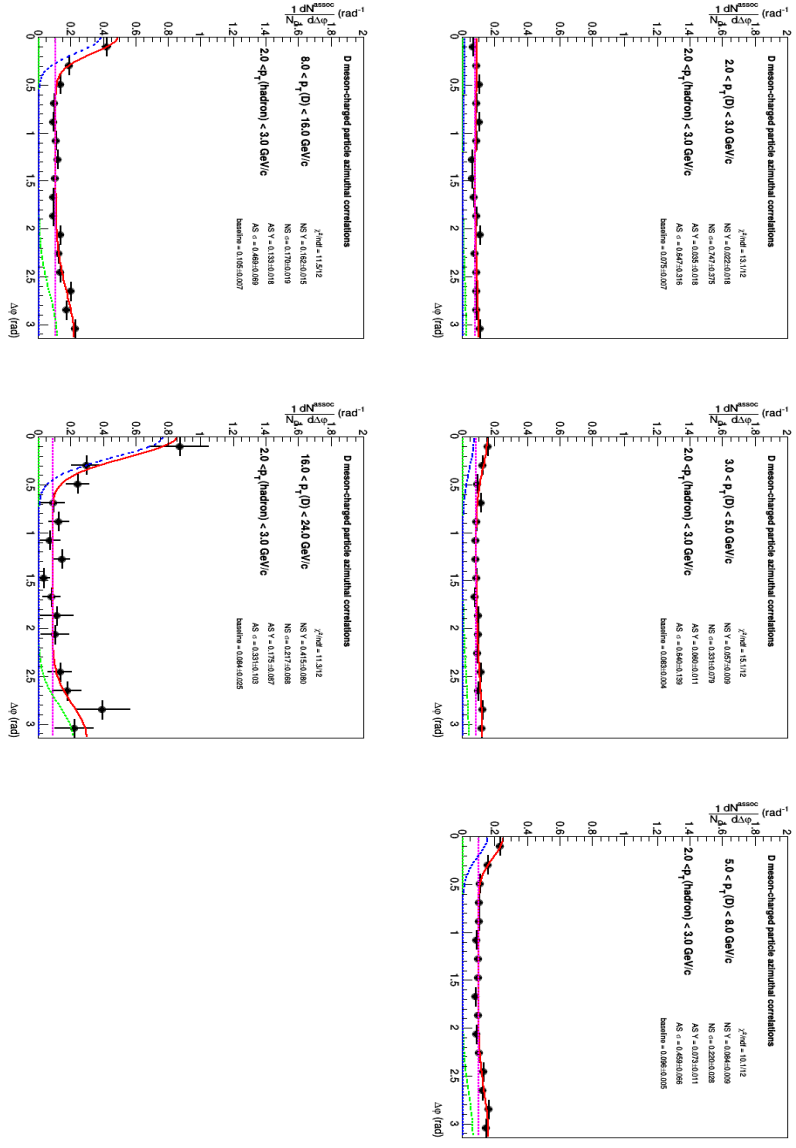


Figure 58: Fits to azimuthal correlation distributions and baseline estimation, with the generalized Gaussian for the near-side peak. The set of five panels is for $2 < p_T < 3$ GeV/c. The corresponding p_T ranges of D-mesons are reported in each panel.

Further information can be obtained comparing the fits with the two function for Monte Carlo templates, where the statistical precision is much better than on data, allowing us to check which function has effectively the compatibility with the points - by visually comparing fit and distribution, looking at the χ^2/ndf and comparing the values of the yields with the bin-counting extracted yields.

This comparison is performed in Figs. 59, 60, 61, 62, for two low and two high p_T ranges. While at low p_T the two fit outcomes are rather similar, as the β parameter is pretty close to 2 (the standard Gaussian value), at high p_T the two fit results are much more differentiated, β is sensibly smaller than 2, the shape of the generalized Gaussian has much thinner core and higher tails, and catches much better the peak tails (having also a better χ^2 and a better agreement with bin-counting yields).

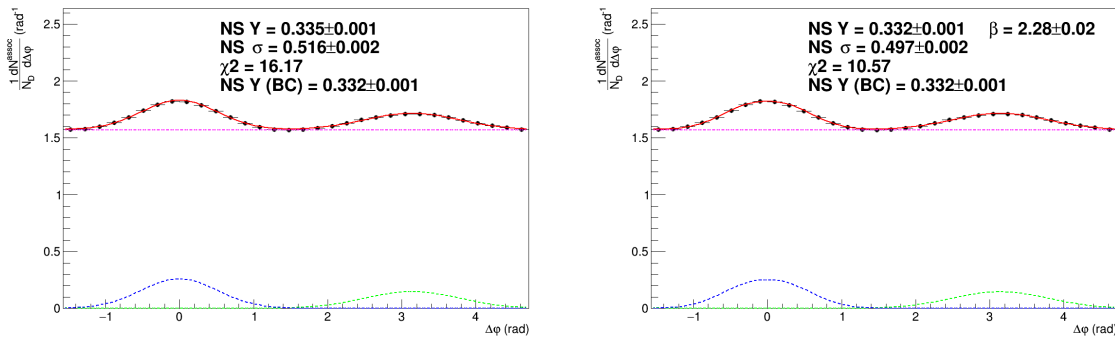


Figure 59: Comparison of fit outcome for POWHEG+PYTHIA templates for standard (left) and generalized Gaussian (right) for the near-side, for $p_T(\text{D})$ 3-5 GeV/ c and $p_T(\text{assoc})$ 0.3 – 1.

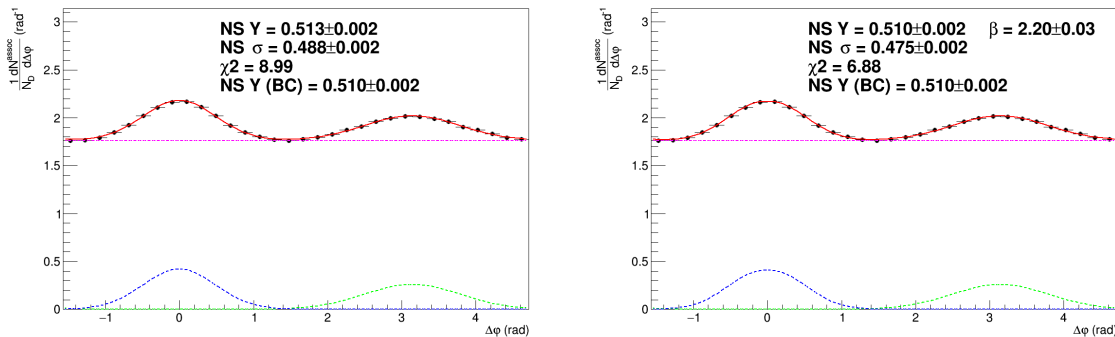


Figure 60: Comparison of fit outcome for POWHEG+PYTHIA templates for standard (left) and generalized Gaussian (right) for the near-side, for $p_T(\text{D})$ 5-8 GeV/ c and $p_T(\text{assoc})$ 0.3 – 1.

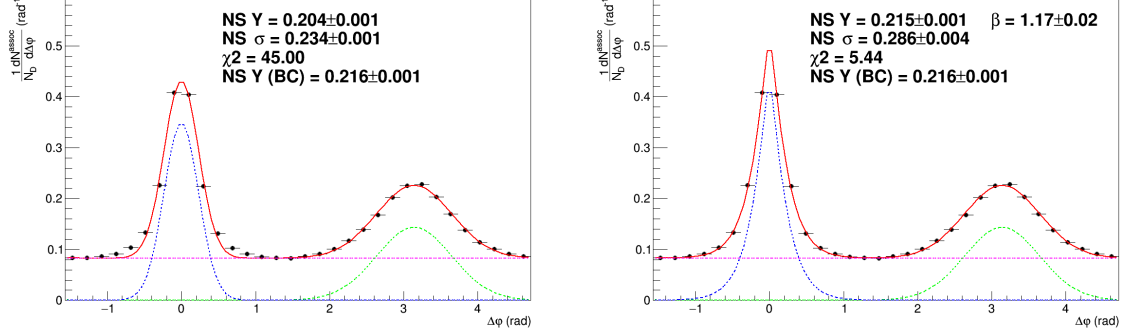


Figure 61: Comparison of fit outcome for POWHEG+PYTHIA templates for standard (left) and generalized Gaussian (right) for the near-side, for $p_T(\text{D})$ 8-16 GeV/ c and $p_T(\text{assoc})$ 2 – 3.

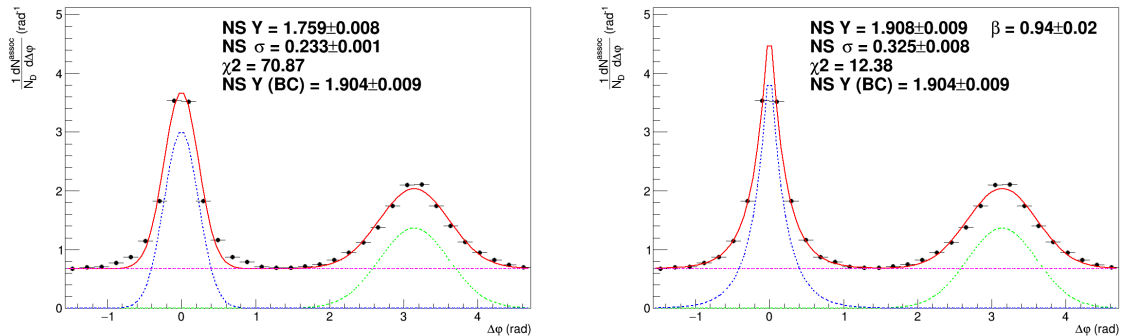


Figure 62: Comparison of fit outcome for POWHEG+PYTHIA templates for standard (left) and generalized Gaussian (right) for the near-side, for $p_T(\text{D})$ 16-24 GeV/ c and $p_T(\text{D}) > 1$.

701 **5.4 Systematic uncertainties on fit observables**

702 The evaluation of the systematic uncertainties on the observables obtained from the fits is performed as
 703 follows:

- 704 – The fits are repeated by changing the range of the transverse region in which the baseline is eval-
 705 uated. Alternate definitions of $\frac{\pi}{4} < |\Delta\phi| < \frac{3\pi}{8}$, $\frac{3\pi}{8} < |\Delta\phi| < \frac{\pi}{2}$ and $\frac{\pi}{4} < |\Delta\phi| < \frac{5\pi}{8}$ are considered.
- 706 – This is performed both with the standard Gaussian function, and for the generalized Gaussian
 707 function (for the near-side description). Hence, 4 variations for each fitting function are considered.
- 708 – In addition, $\Delta\phi$ correlation points are shifted to the upper and lower bounds of their uncorrelated
 709 systematic boxes, and refitted (with the standard Gaussian).
- 710 – The fits are also repeated by moving the baseline value from its default value (i.e. with the default
 711 transverse region) on top and on bottom of its statistic uncertainty before fitting with the default
 712 function. This helps to account, though in a systematic uncertainty, for the statistical uncertainty
 713 on the baseline position (since in the fit the baseline is constrained, and its error is not propagated
 714 to the other observables).
- 715 – The envelope between (i) the RMS of the relative variations of the parameters between the fit
 716 outcomes defined in the first three points, and (ii) the relative variations of the parameters from the
 717 fit outcomes defined in the fourth point, is considered as systematic uncertainty for the near-side
 718 and away-side widths.
- 719 – For the estimation of the baseline and of the near-side and away-side yields, instead, the previous
 720 value is added in quadrature with the $\Delta\phi$ -correlated systematics in the correlation distributions,
 721 since these values are affected by a change in the global normalization of the distributions.

$$\sigma^{syst} = \sqrt{(Max(\Delta par^{ped.mode,fit funct}, \Delta par^{\Delta\phi point}))^2 + (\sigma_{Syst}^{corr})^2} \quad (11)$$

722 **5.5 Results for near-side yield and width, away-side yield and width, and baseline**

723 Figures 63, 64, 65, 66 and 67 show the near-side associated yield, width (the sigma of the Gaussian part
 724 of the fit functions), away-side associated yield, width and the height of the baseline, for the average
 725 correlation distributions, in the kinematic ranges studied in the analysis, together with their statistical
 726 and systematic uncertainties. For each kinematic range, the correspondent plot showing the systematic
 727 uncertainty of the considered observable from the variation of the fit procedure is reported as well (which
 728 is the full systematic uncertainty for the widths).

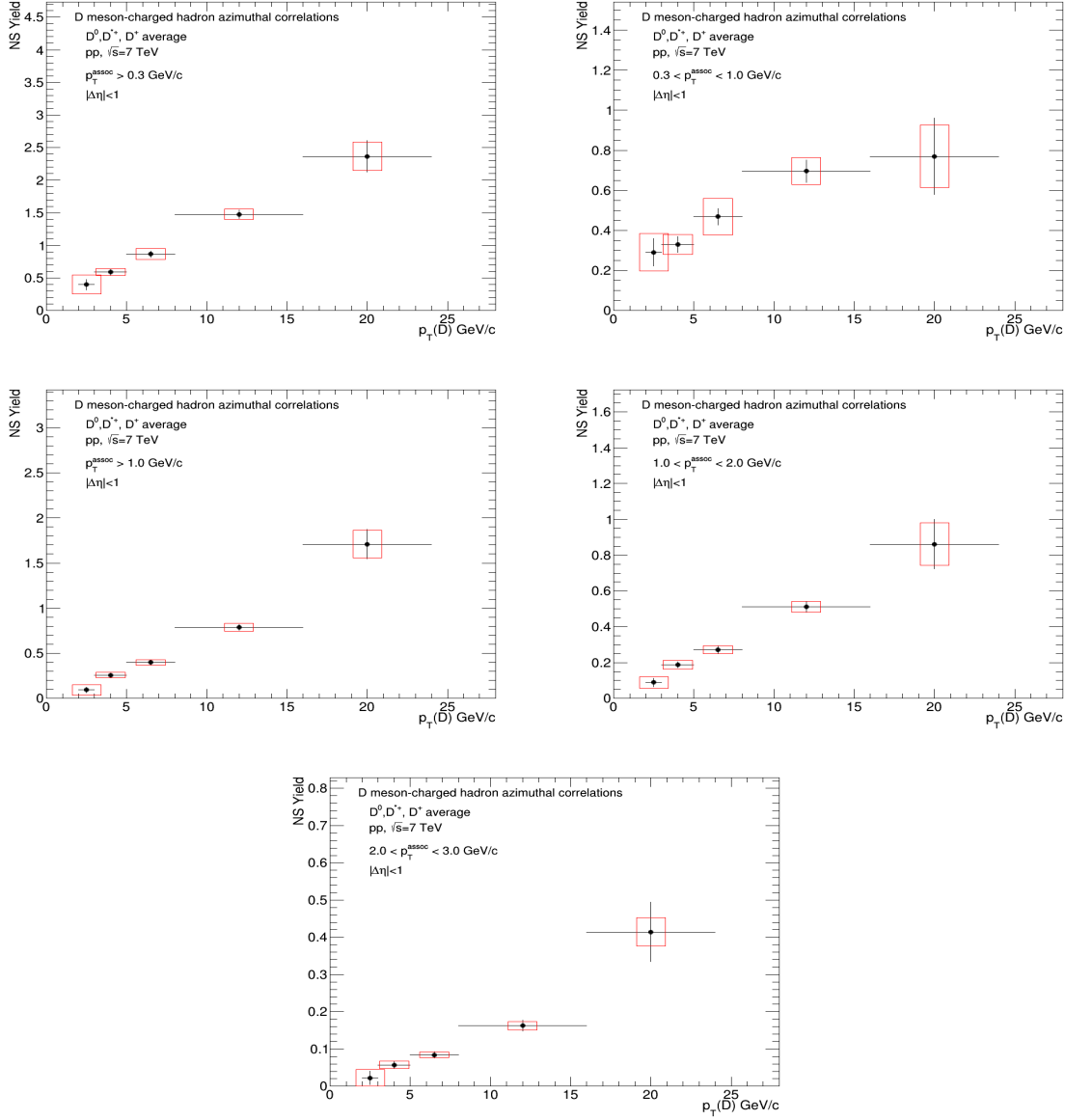


Figure 63: D-meson p_T trend of near-side yield, for the various associated track p_T ranges, with statistical and systematic uncertainties. Note: do not consider the first bin of each panel (excluded from the results).

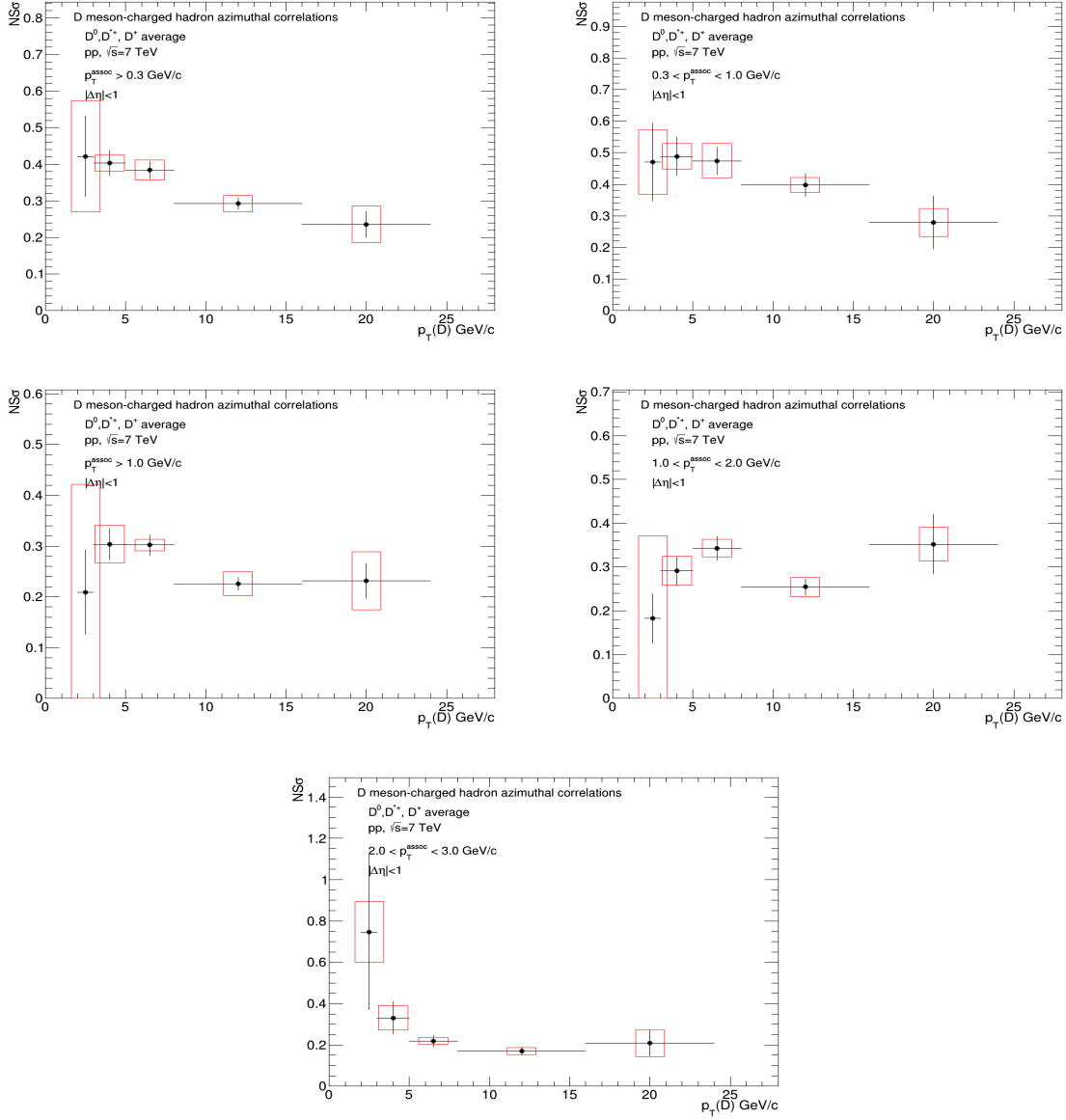


Figure 64: D-meson p_T trend of near-side width, for the various associated track p_T ranges, with statistical and systematic uncertainties. Note: do not consider the first bin of each panel (excluded from the results).

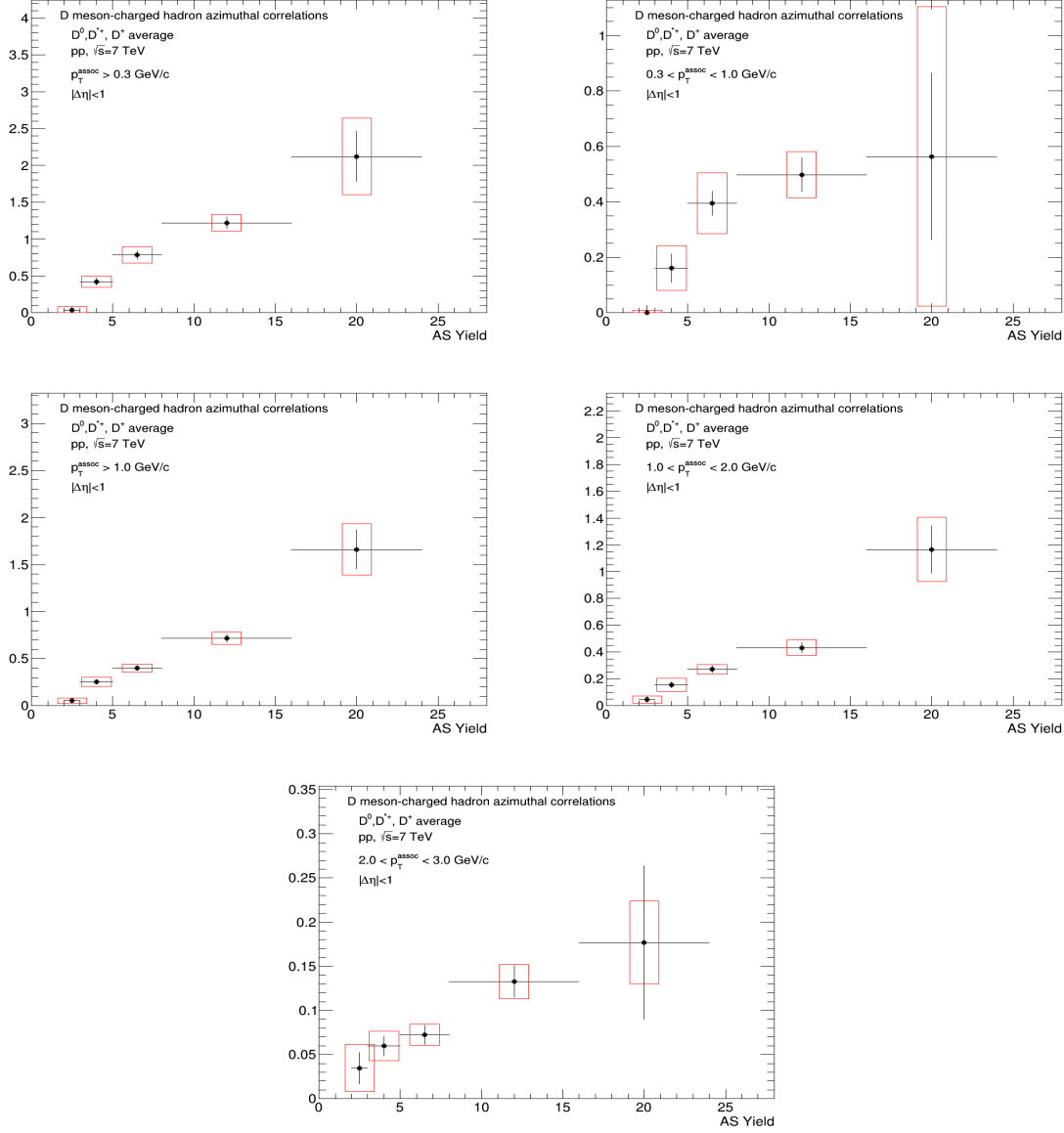


Figure 65: D-meson p_T trend of away-side yield, for the various associated track p_T ranges, with statistical and systematic uncertainties. Note: do not consider the first bin of each panel (excluded from the results).

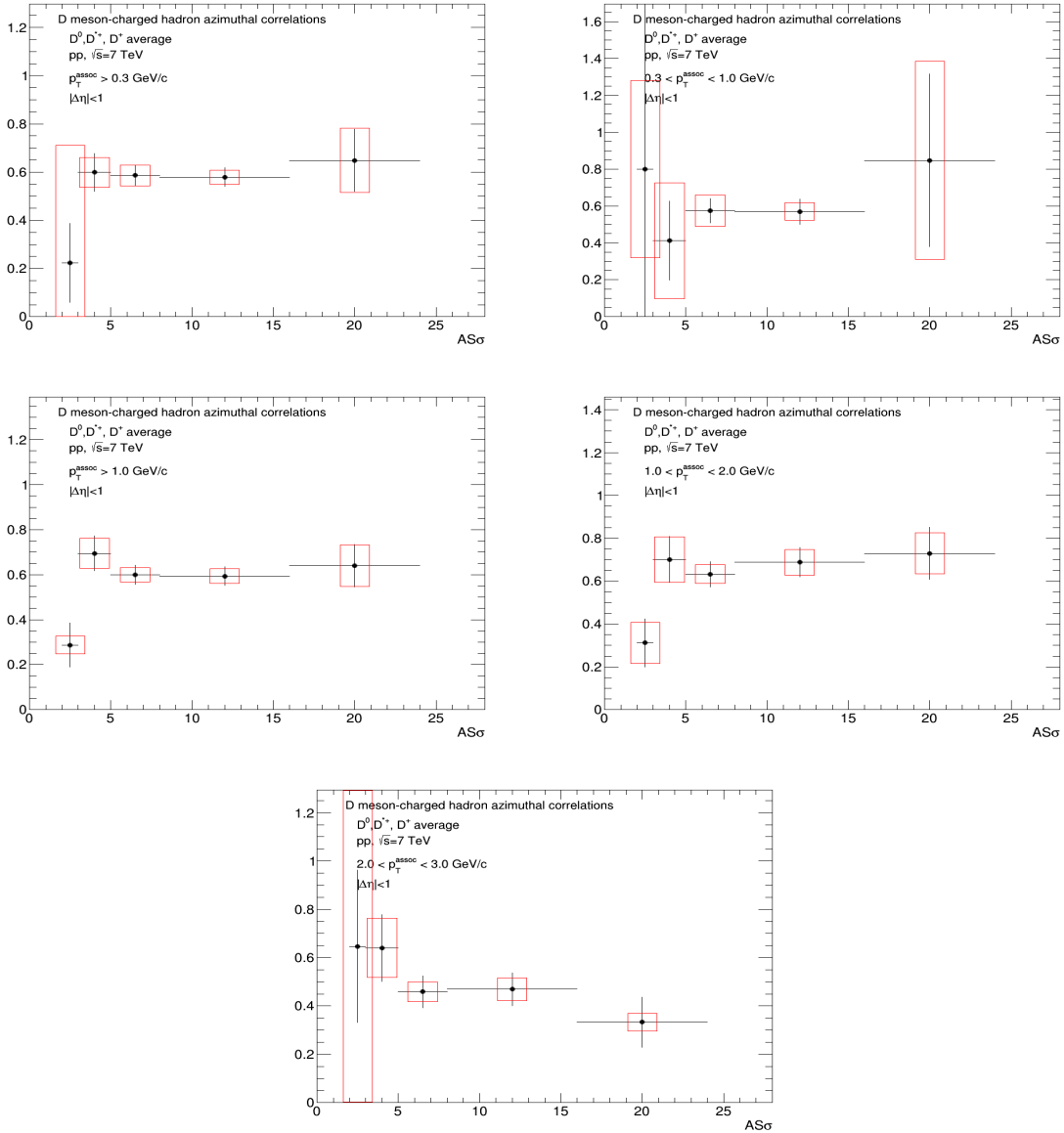


Figure 66: D-meson p_T trend of away-side width, for the various associated track p_T ranges, with statistical and systematic uncertainties. Note: do not consider the first bin of each panel (excluded from the results).

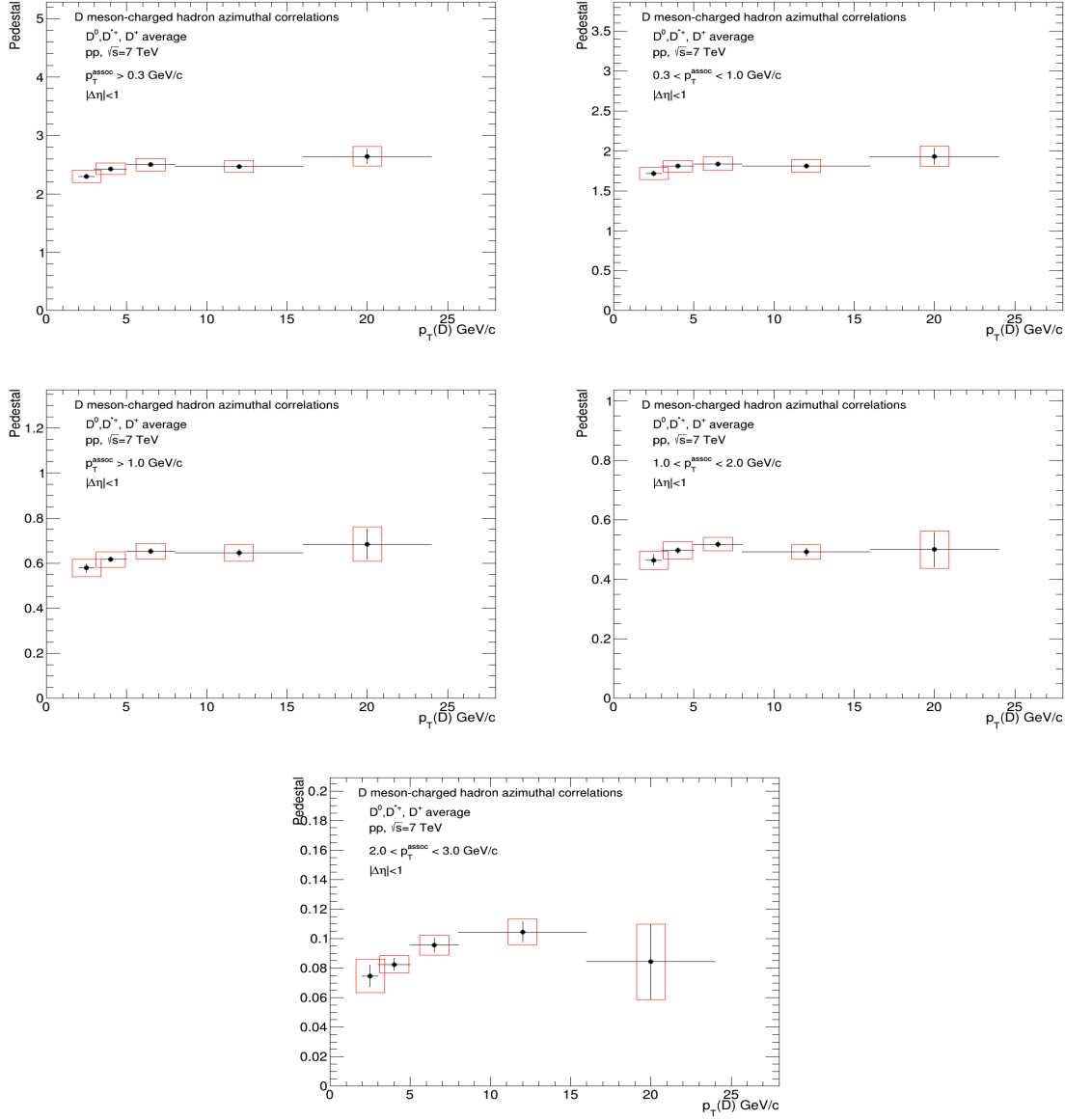


Figure 67: D-meson p_T trend of baseline, for the various associated track p_T ranges, with statistical and systematic uncertainties. Note: do not consider the first bin of each panel (excluded from the results).

Figures 72, 73, 74, 75 show the systematic uncertainties for near side yield and width, away side yield and width due to the alternate fit approaches, with the breakdown for each of the contributions. The green line is the RMS of the first three kind of variations, the black the envelope between this RMS and fourth kind of variations (baseline shifted by 1σ stat) - see the previous section for details.

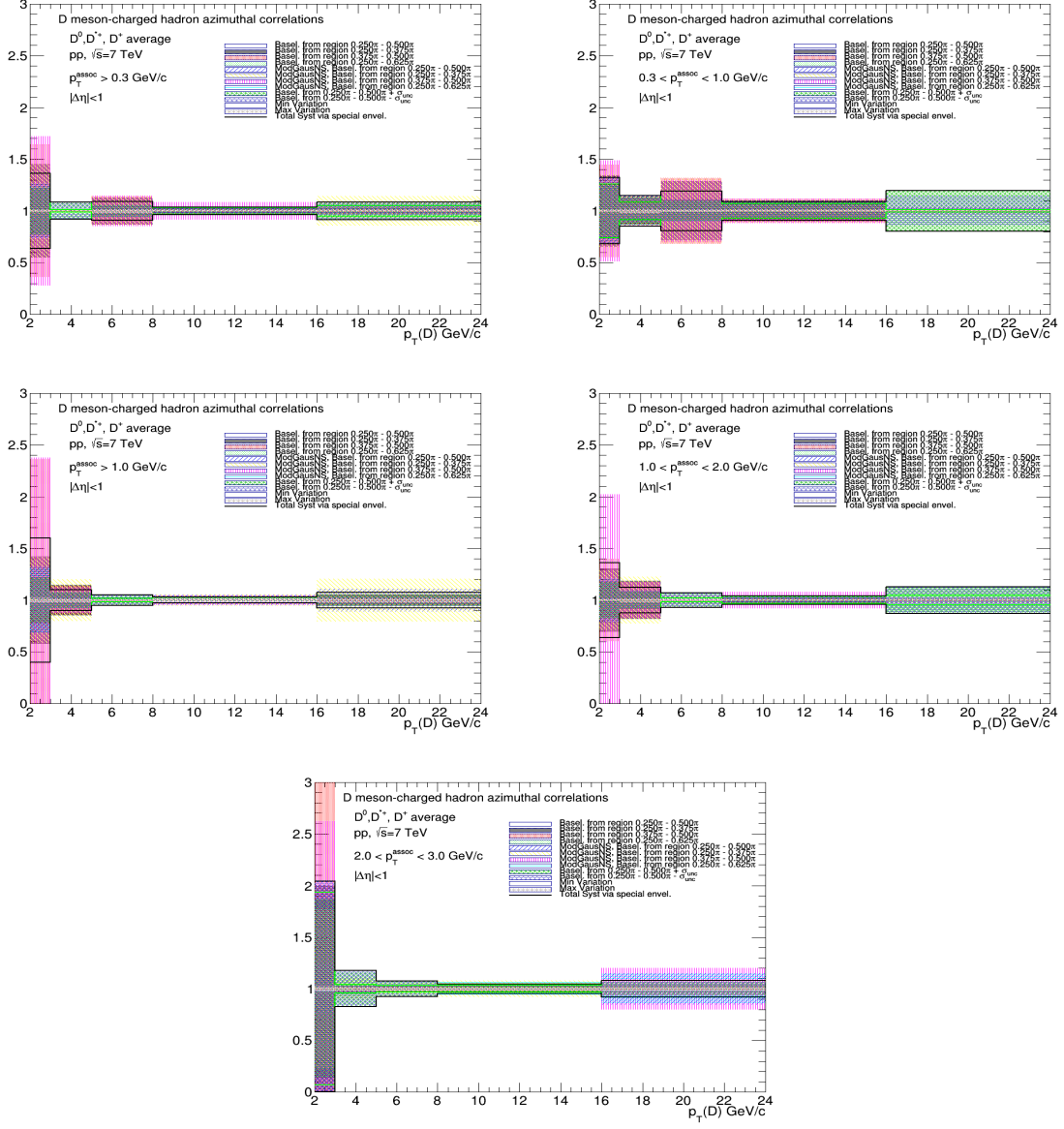


Figure 68: D-meson p_T trend of uncertainties from fit variations for near-side yield, for the various associated track p_T ranges. Note: do not consider the first bin of each panel (excluded from the results).

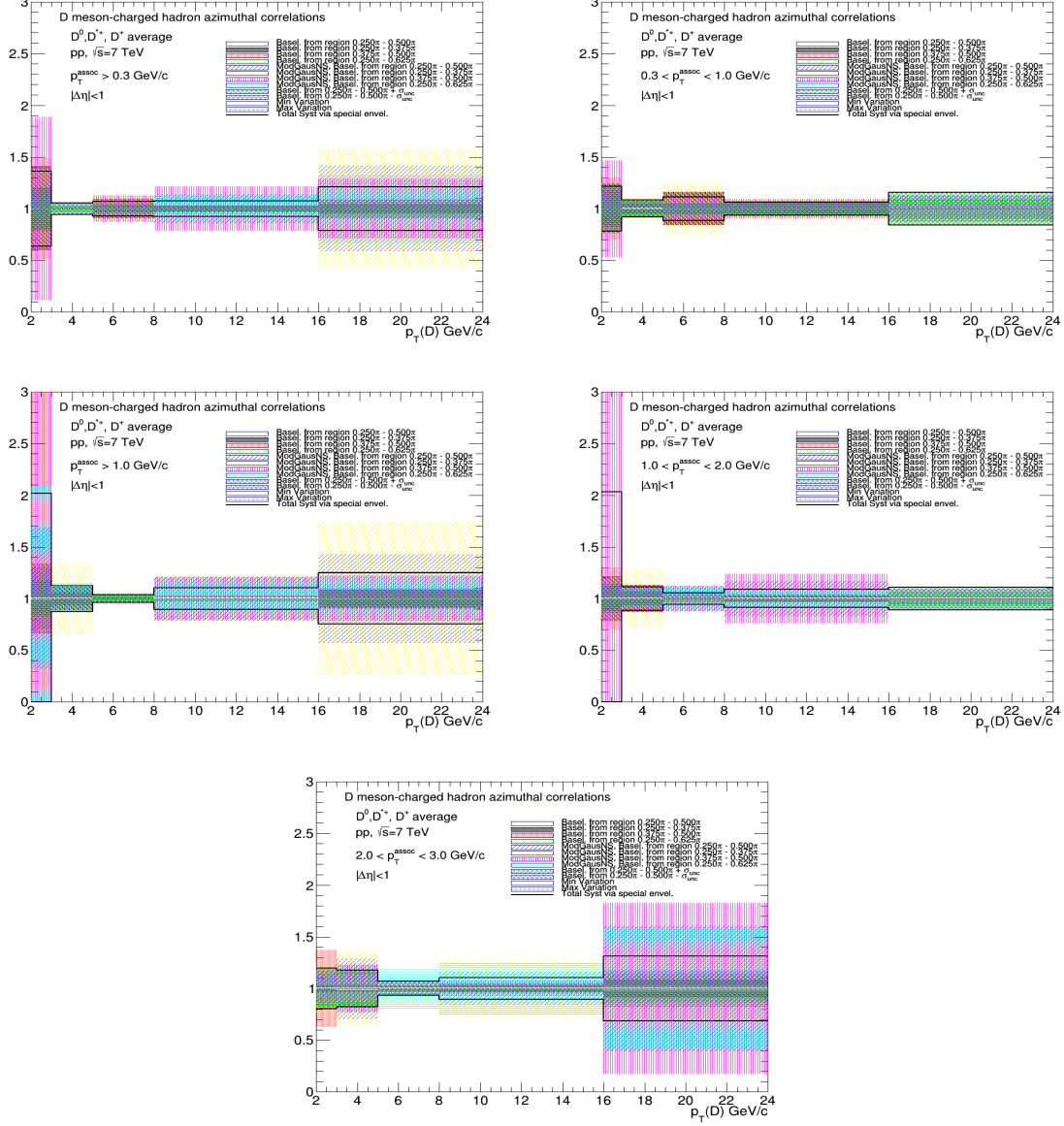


Figure 69: D-meson p_T trend of uncertainties from fit variations for near-side width, for the various associated track p_T ranges. Note: do not consider the first bin of each panel (excluded from the results).

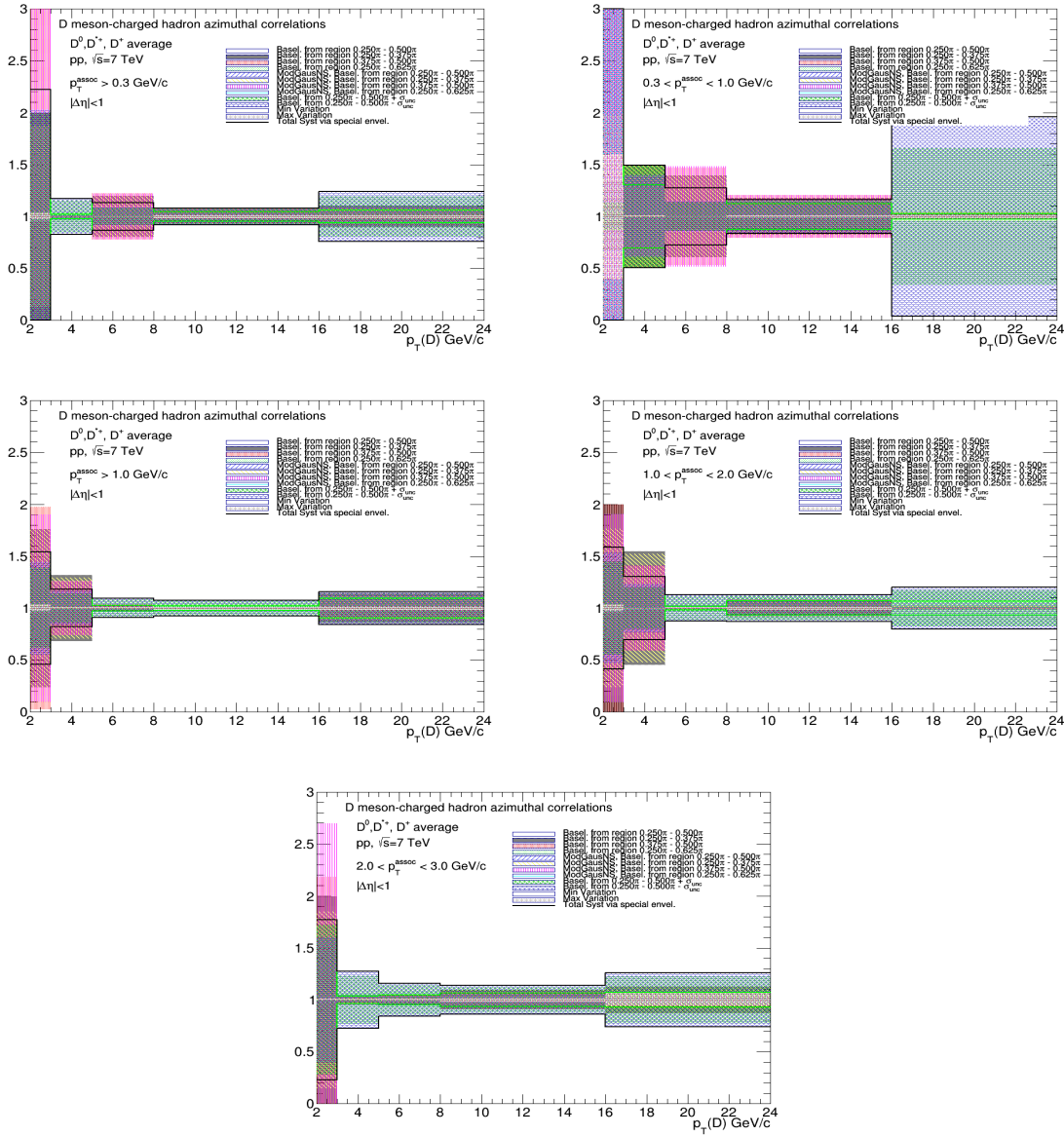


Figure 70: D-meson p_T trend of uncertainties from fit variations for away-side yield, for the various associated track p_T ranges. Note: do not consider the first bin of each panel (excluded from the results).

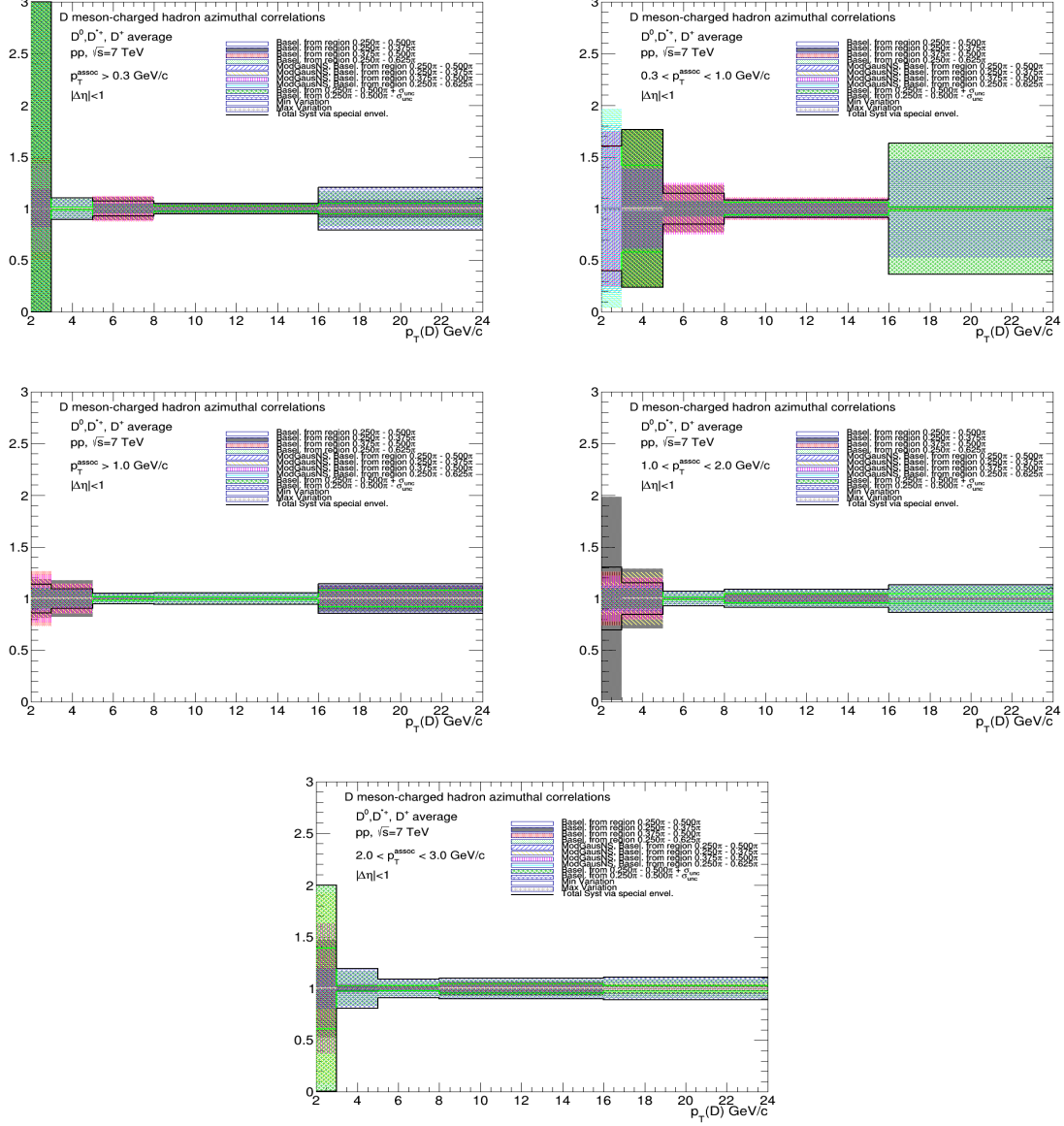


Figure 71: D-meson p_T trend of uncertainties from fit variations for away-side width, for the various associated track p_T ranges. Note: do not consider the first bin of each panel (excluded from the results).

Figures 72, 73, 74, 75 and 76 show the full systematic uncertainties for near side yield and width, away side yield and width, and baseline, with the breakdown of fit variation and $\Delta\phi$ correlated systematic uncertainties.

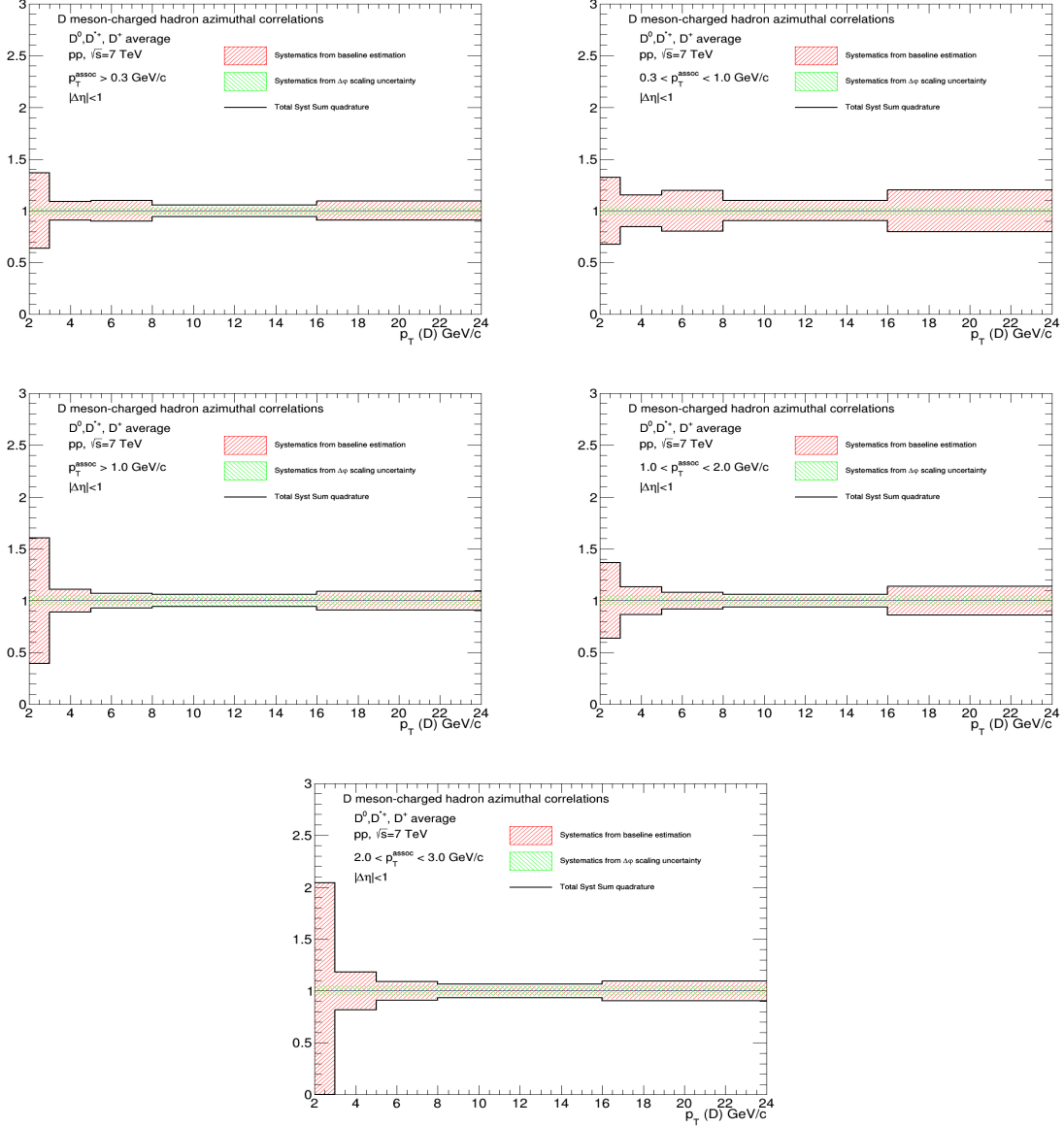


Figure 72: D-meson p_T trend of total systematic uncertainties for near-side yield, for the various associated track p_T ranges. Note: do not consider the first bin of each panel (excluded from the results).

5.6 Final plots and comparisons

5.6.1 Comparisons of pp and p-Pb at 5 TeV

Figure 77 (two pages) shows the average of D^0 , D^+ and D^{*+} azimuthal correlations for 2017 pp and 2016 p-Pb for all the kinematic ranges of trigger and associated particles p_T . Overall, compatibility within uncertainties between the two collision systems is found for all the common kinematic ranges analyzed, and a similar evolution of the correlation pattern with transverse momentum holds for the two systems. Focusing on the peak regions, while one can appreciate a full near-side compatibility, for some kinematic regions the away-side region seems to be enhanced in p-Pb with respect to pp. As it could be

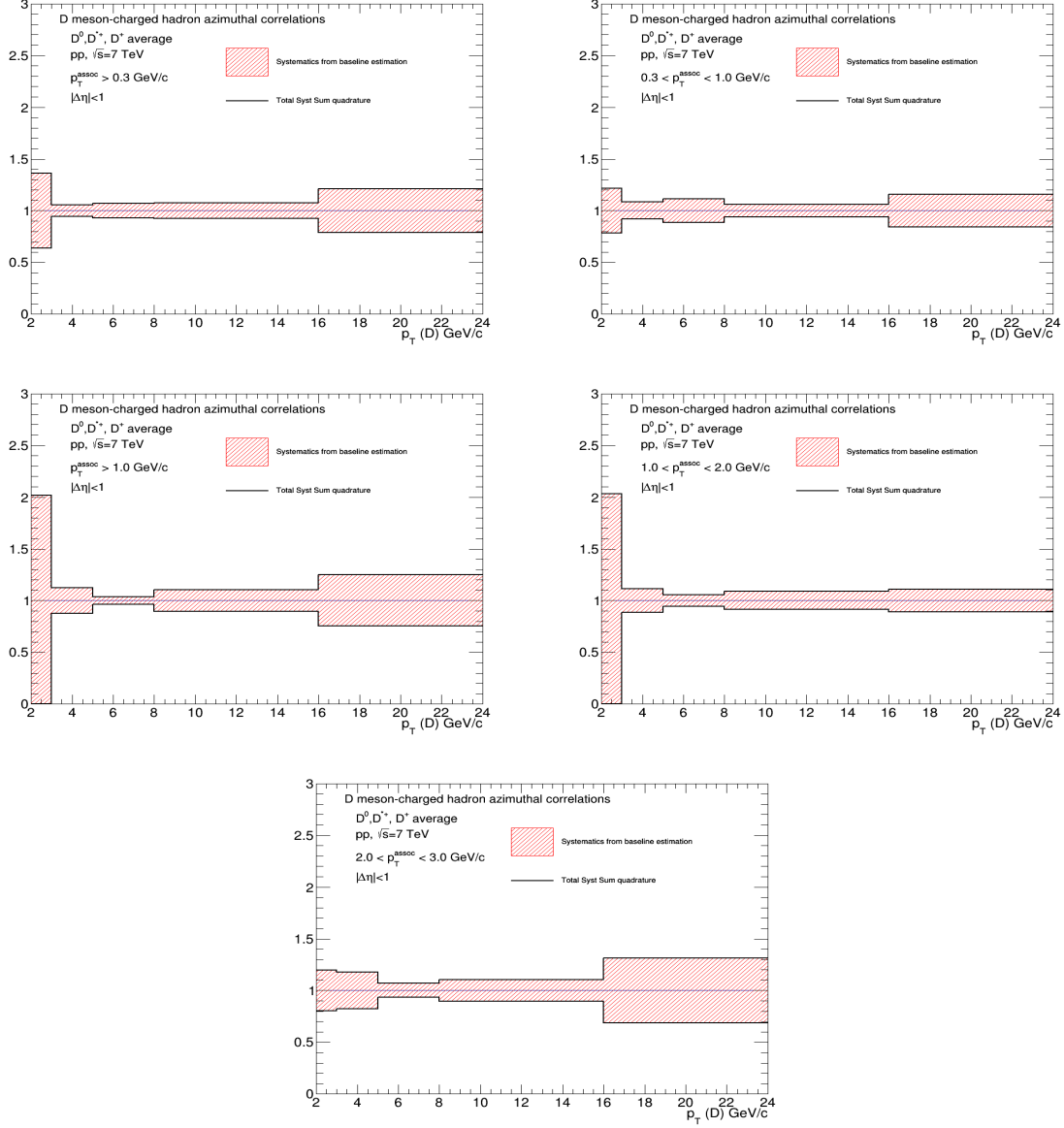


Figure 73: D-meson p_T trend of total systematic uncertainties for near-side width, for the various associated track p_T ranges. Note: do not consider the first bin of each panel (excluded from the results).

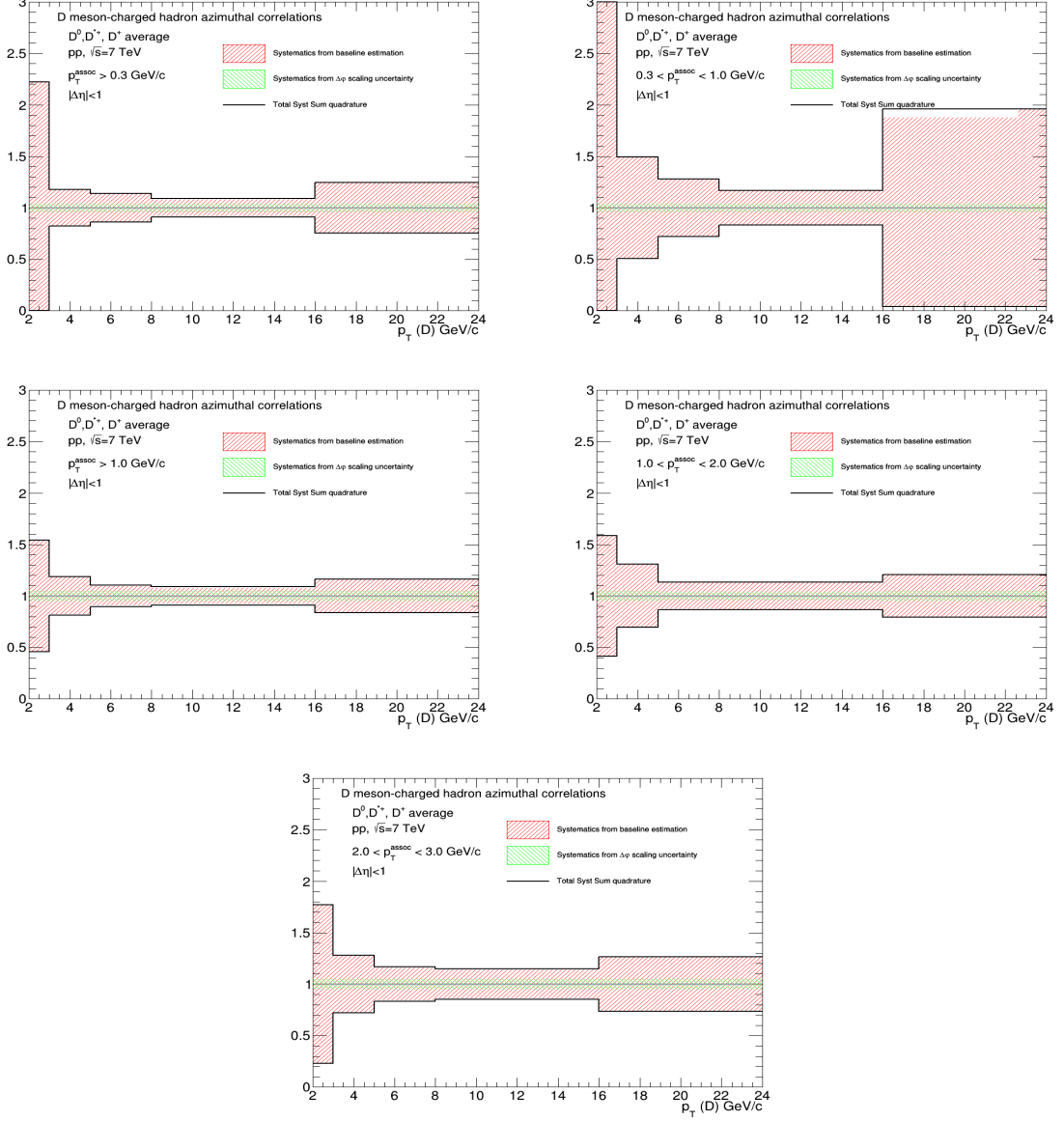


Figure 74: D-meson p_T trend of total systematic uncertainties for away-side yield, for the various associated track p_T ranges. Note: do not consider the first bin of each panel (excluded from the results).

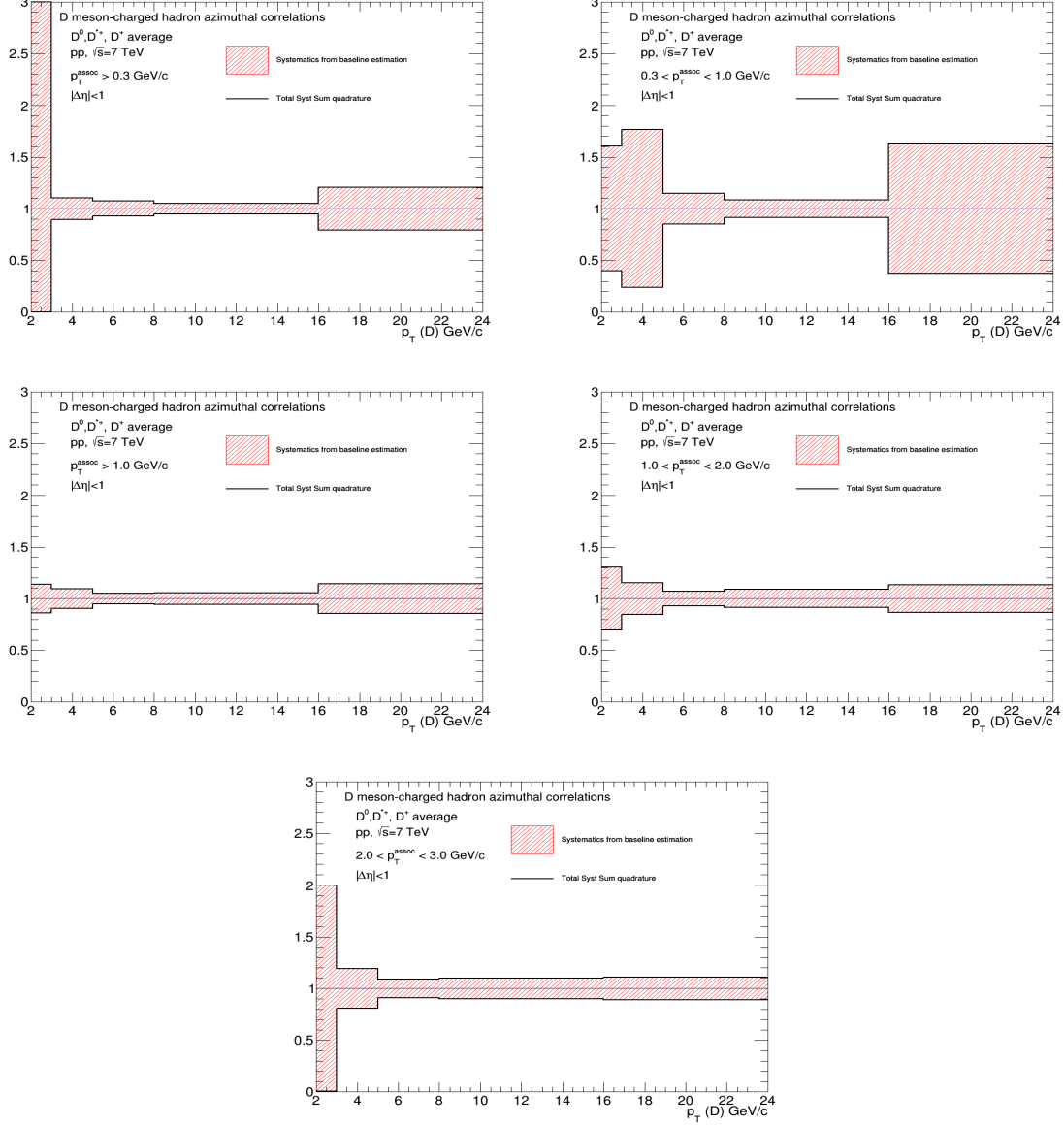


Figure 75: D-meson p_T trend of total systematic uncertainties for away-side width, for the various associated track p_T ranges. Note: do not consider the first bin of each panel (excluded from the results).

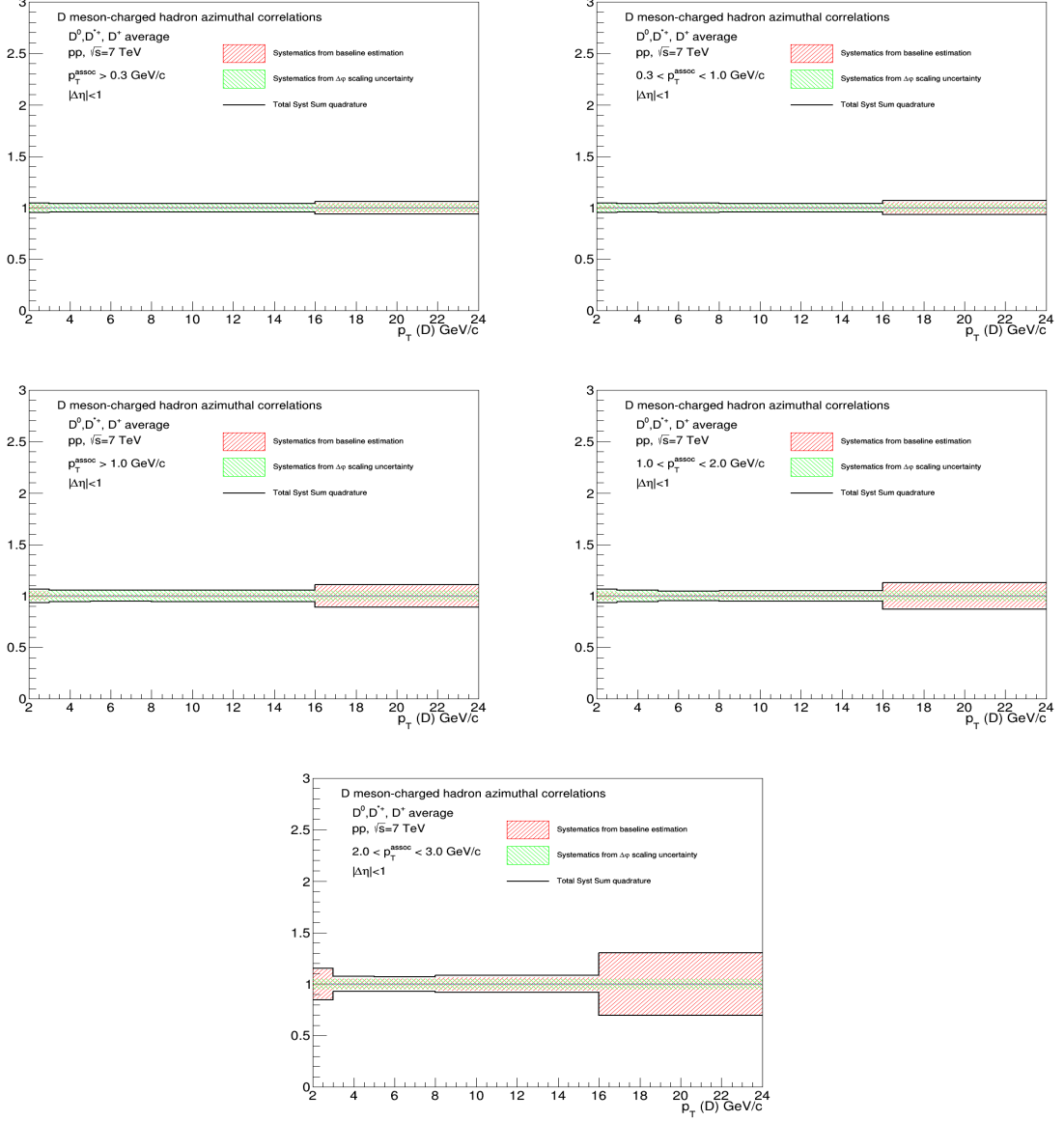


Figure 76: D-meson p_T trend of total systematic uncertainties for baseline, for the various associated track p_T ranges. Note: do not consider the first bin of each panel (excluded from the results).

already noticed from the comparison of the distributions, near-side observables are fully consistent. For the away-side region, instead, the peak widths are roughly compatible (within rather large uncertainties), while a hint of larger yields in p-Pb can be observed, especially from 5 to 16 GeV/c for the D-meson p_T , generally in all the associated track p_T regions. In Figs. 78,79 the comparison of the observables extracted from the fits (near-side yield and width) is also presented.

5.6.2 Comparisons of pp at 5, 7 and 13 TeV

Figure 80 shows the average of D^0 , D^+ and D^{*+} azimuthal correlations for pp at 5 TeV compared with pp at 7 TeV and 13 TeV for all the common kinematic ranges of trigger and associated particles p_T analysed. The data distribution of pp at 5 TeV have much better uncertainties than 7 TeV and also quite better than 13 TeV. Compatibility within uncertainties between the three energy systems is found for all the common kinematic ranges analyzed.

In Figs. 81 and 82, the comparison of the observables extracted from the fits (near-side yield and width for first page, away-side yield and width for second page) is also presented.

The near-side observables do not show difference above the uncertainties, which are not small (especially for past results), not allowing to quantitatively appreciate any energy dependence of the yields, expected to be of the order of 5-6% for 5 vs 7 TeV and of 10-12% for 5 vs 13 TeV results from Pythia8 and POWHEG+PYTHIA simulations. Qualitatively, anyway, it can be observed that yield values at 13 TeV are generally larger than yields at 5 TeV, following the expectations of some mild energy scaling of this observable.

Nothing can be said, instead, for the away-side observables, where the precision is not enough to draw any conclusion, even qualitatively - also because model expectations for away-side observables at different energies predict much similar results at the three energies, much smaller than the current uncertainties. Indeed, away-side results at 7 and 13 TeV were not approved in the past (and this comparison plot is for internal use only, its approval will not be requested).

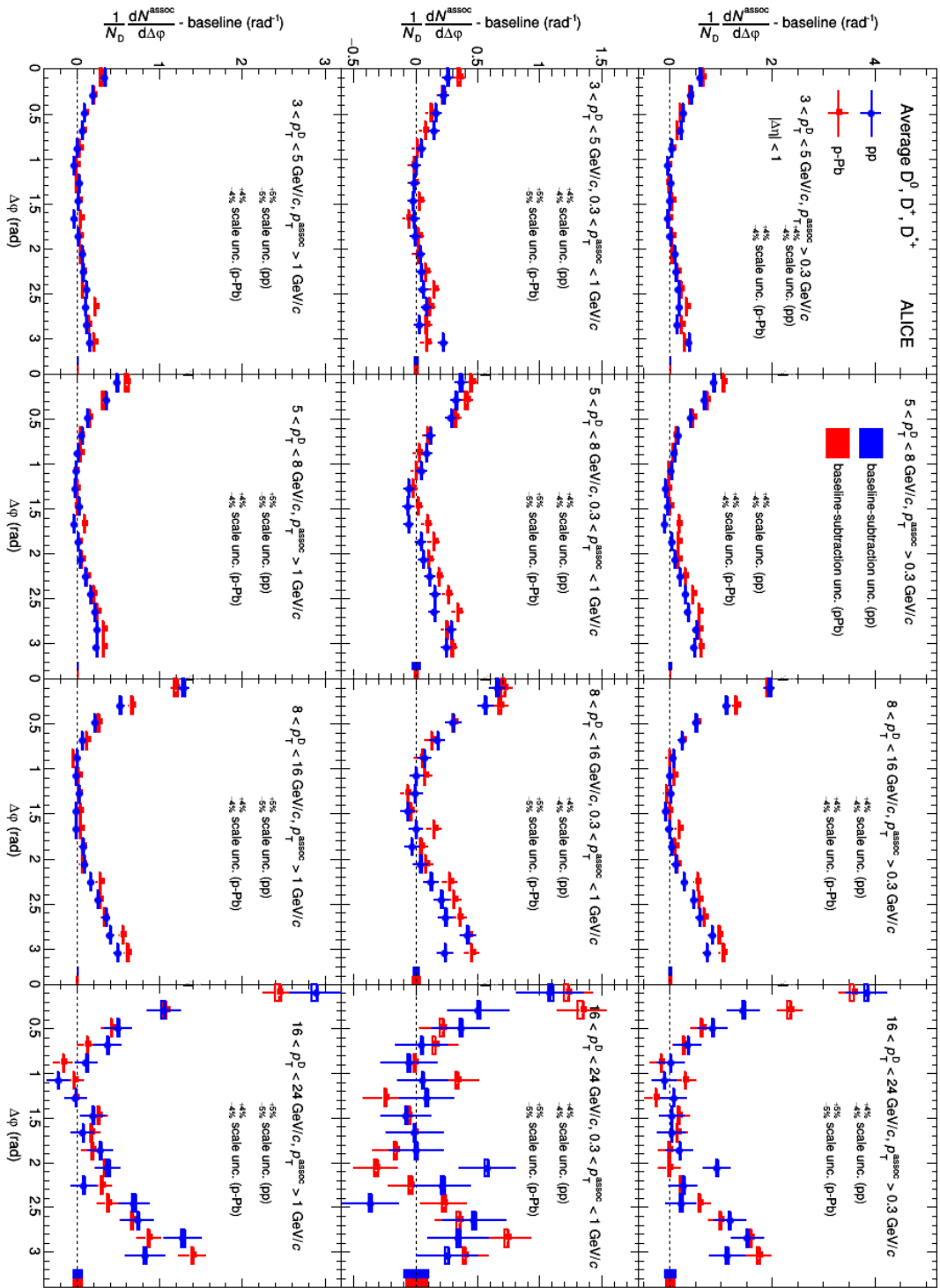
5.6.3 Comparisons of pp at 5 TeV and model predictions

Figure 83 (two pages) shows the average of D^0 , D^+ and D^{*+} azimuthal correlations for pp for several ranges of trigger and associated p_T , compared to different Pythia6 tunes (Perugia 0, 2010, 2011), Pythia 8 (tune 4C) and POWHEG+PYTHIA at the same collision energy. A substantial agreement in the overall momentum evolution of the correlation pattern is observed within uncertainties for what concerns the near-side region, apart from very high p_T of the D-meson, where the peak seems to be slightly underestimated, at least by PYTHIA predictions. For the away-side region, the models themselves differentiate in predicting the height of the peak, and generally the strength of the peak overestimate the data measurements, especially for the older Perugia tunes (PYTHIA6-Perugia0 and PYTHIA6-Perugia2010).

In Figs. 84 and 85 (two pages for each) the comparison of the extracted physical observables (near-side and away-side yield, width and baseline height) is presented.

For the near-side yields, POWHEG tends to predict larger values than PYTHIA6,8, in all associated track p_T regions. Data results seem to behave in-between of the two predictions, apart from $16 < p_T(D) < 24 \text{ GeV}/c$ range, where excluding the lowest associated p_T range, data are better described by POWHEG. For the near-side width, POWHEG also tends to predict wider peaks, in this case generally overpredicting the observed values, which are better matched by PYTHIA predictions (though no model can be ruled out with current uncertainties).

Focusing on the away-side region, POWHEG expectation foresee smaller peaks, with respect to all Pythia6 predictions, which is confirmed by data, especially for the yields, and in the intermediate D-meson p_T region (while Pythia6 predictions overestimate the data especially at mid-high p_T). Pythia8



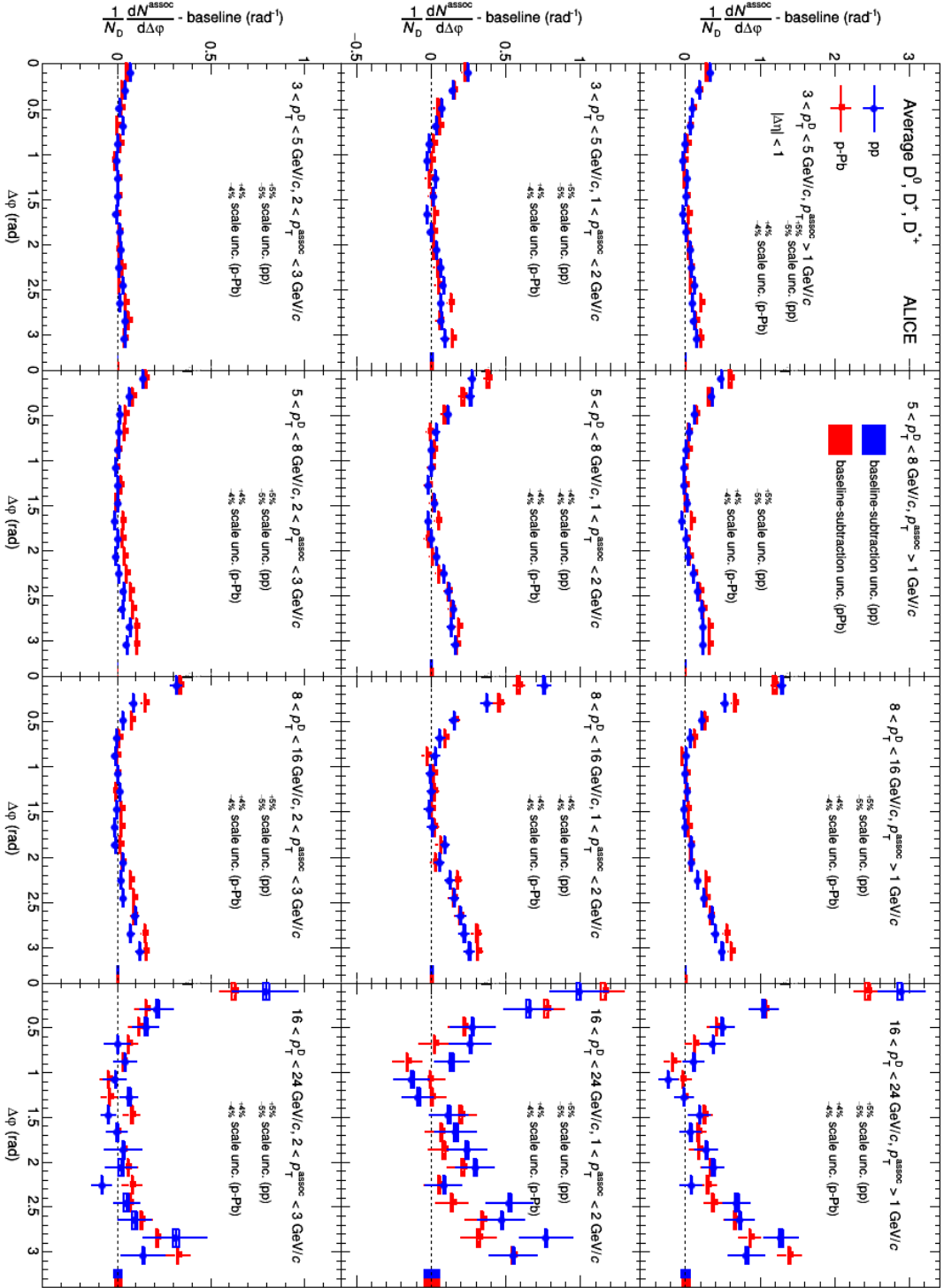


Figure 77: Average of D^0 , D^+ and D^{*+} azimuthal correlations in pp (blue) and p-Pb (red) in all the kinematic ranges of trigger and associated particles.

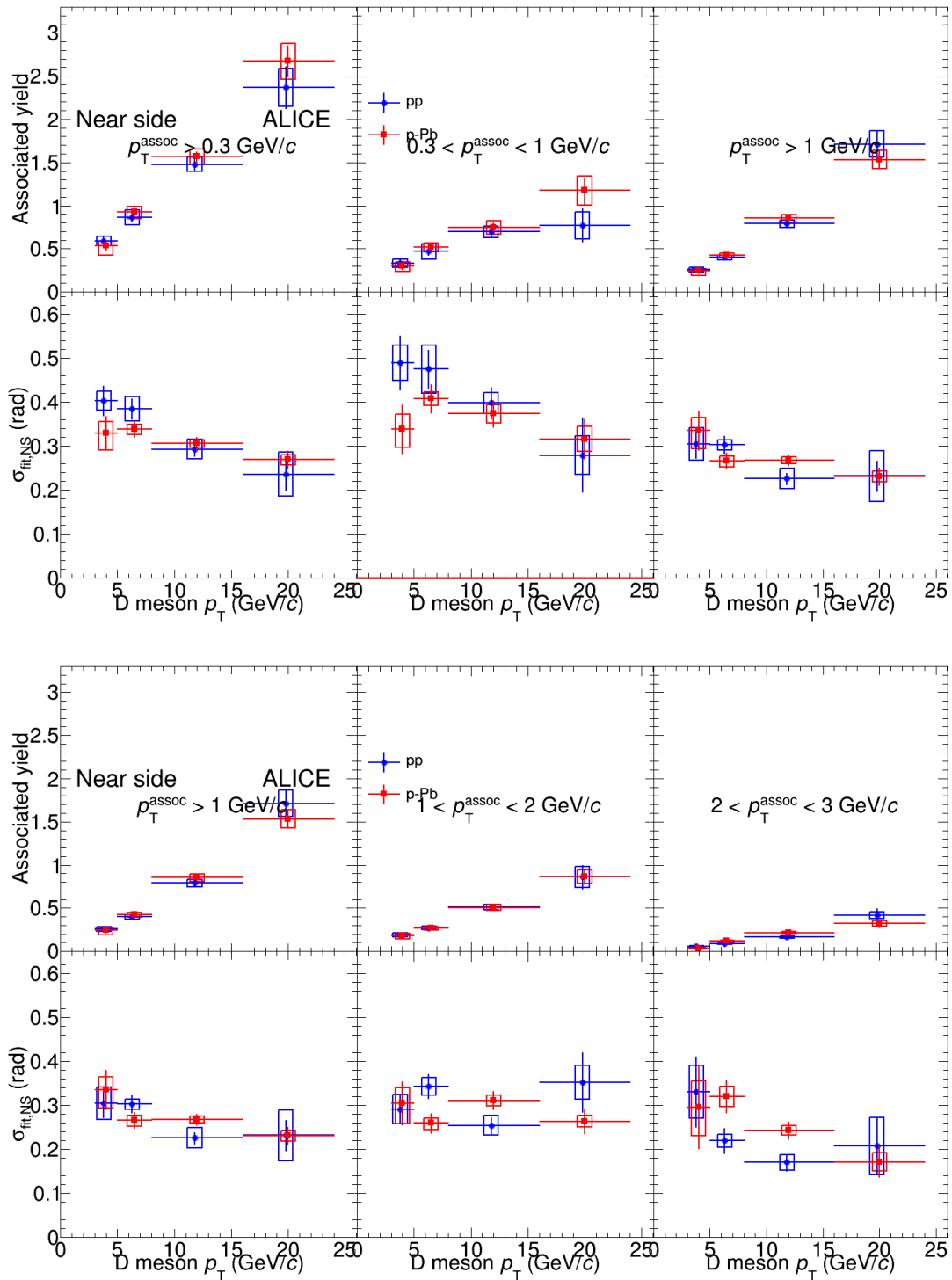


Figure 78: Near-side yield and sigmas for the average of D^0 , D^+ and D^{*+} azimuthal correlations in pp (red) and p-Pb (black) in all the kinematic regions of trigger and associated track.

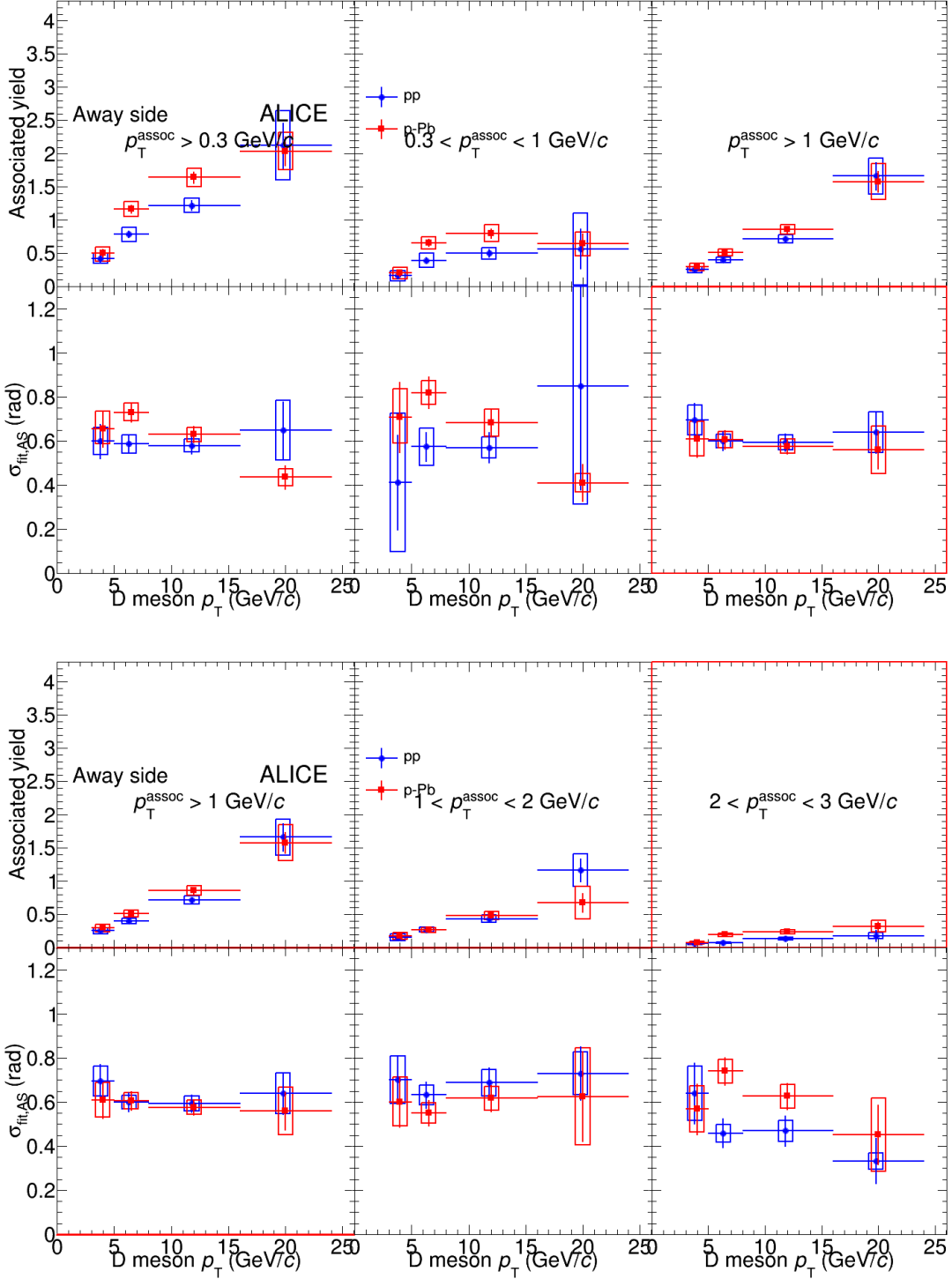


Figure 79: Away-side yield and sigmas for the average of D^0 , D^+ and D^{*+} azimuthal correlations in pp (red) and p-Pb (black) in all the kinematic regions of trigger and associated track.

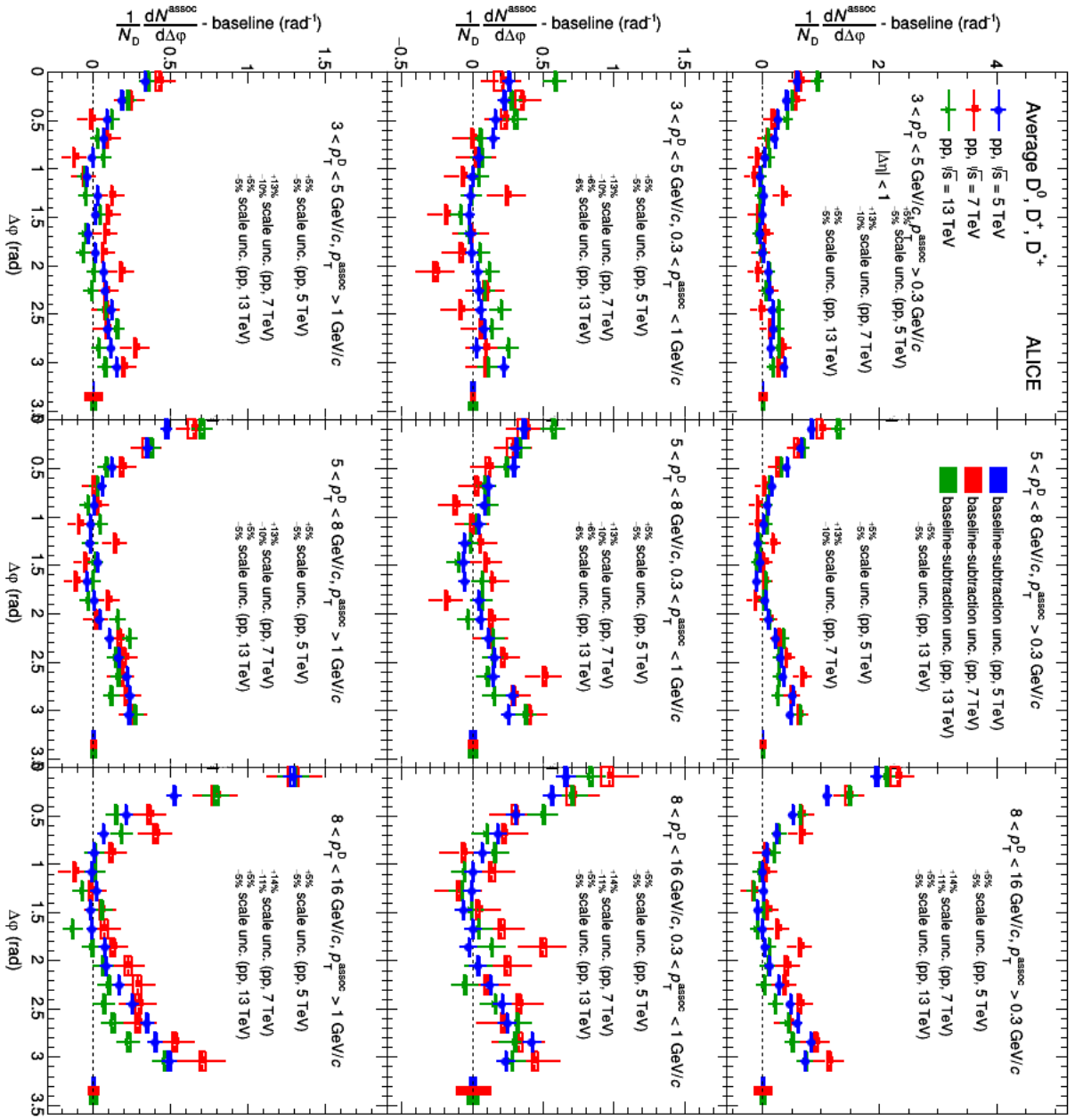


Figure 80: Average of D^0 , D^+ and D^{*+} azimuthal correlations in pp at 5 (blue), 7 (red) and 13 (green) TeV in all the common kinematic ranges of trigger and associated particles.

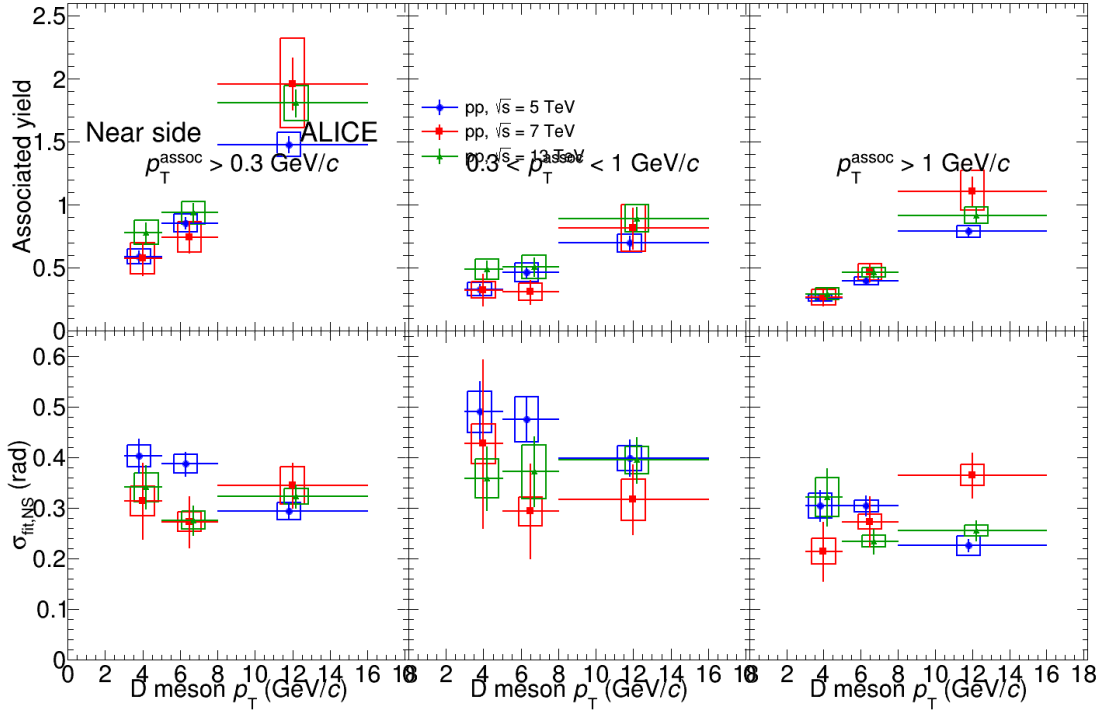


Figure 81: Near-side yield and width for the average of D^0 , D^+ and D^{*+} azimuthal correlations in pp at 5 (blue), 7 (red) and 13 (green) TeV in all the common kinematic regions of trigger and associated track.

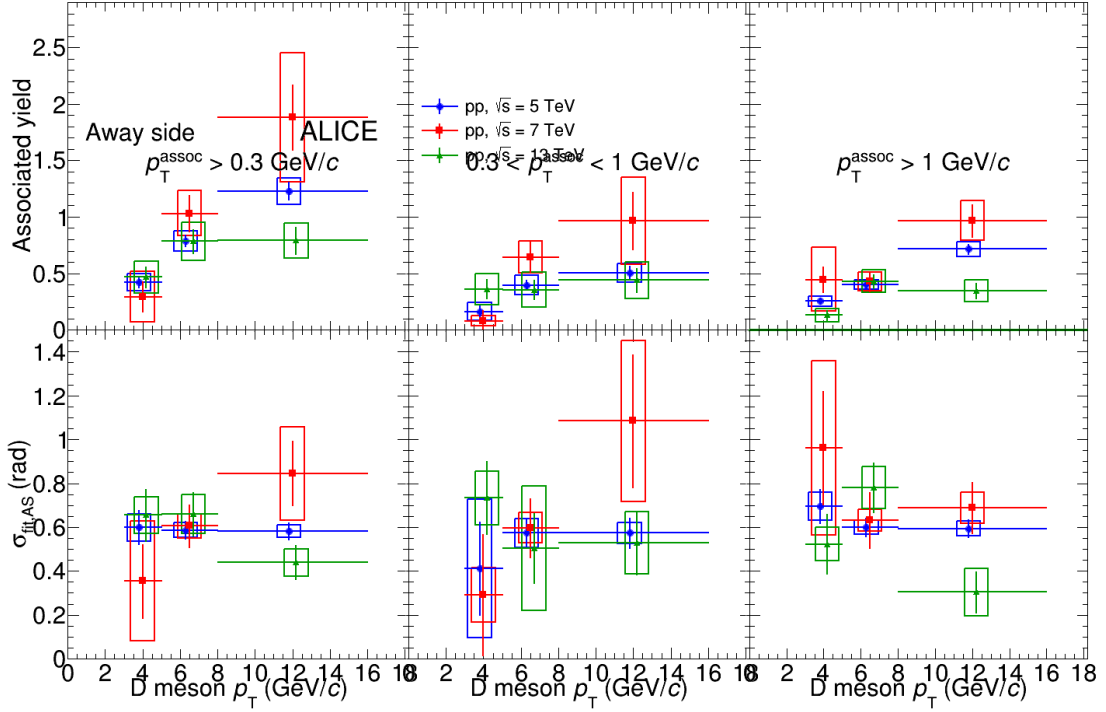
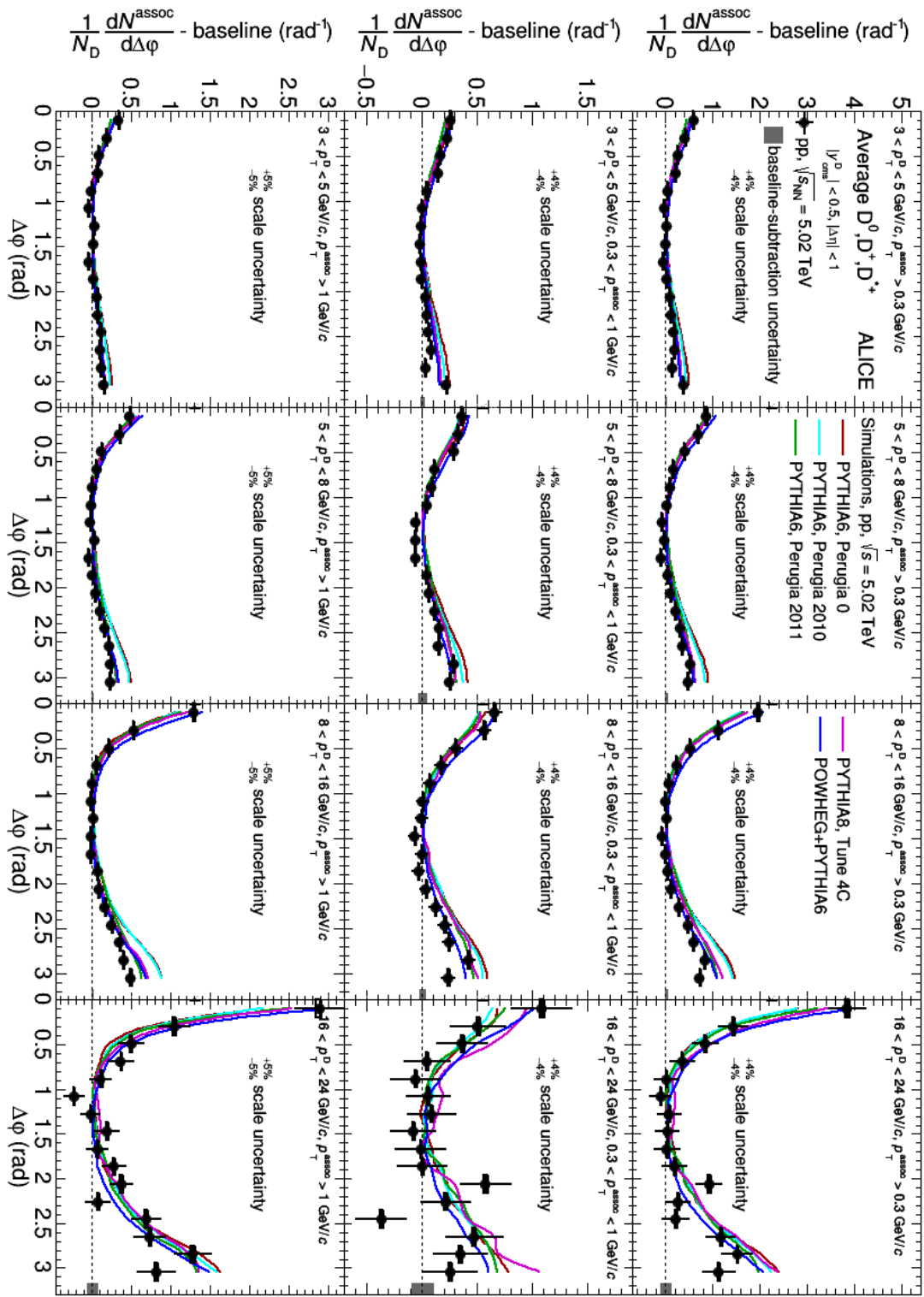


Figure 82: Away-side yield and width for the average of D^0 , D^+ and D^{*+} azimuthal correlations in pp at 5 (blue), 7 (red) and 13 (green) TeV in all the common kinematic regions of trigger and associated track. Note: this is only internal, not for approval.

788 predictions are in-between POWHEG and Pythia6. The values of the widths show a reversed model hi-
789 erarchy with respect to the near-dire predictions, but with small differences, and all models can generally
790 reproduce data. All the models, except possibly PYTHIA6-Perugia0 (which is the oldest), predict similar
791 baseline values, which generally describe well the data measurements.



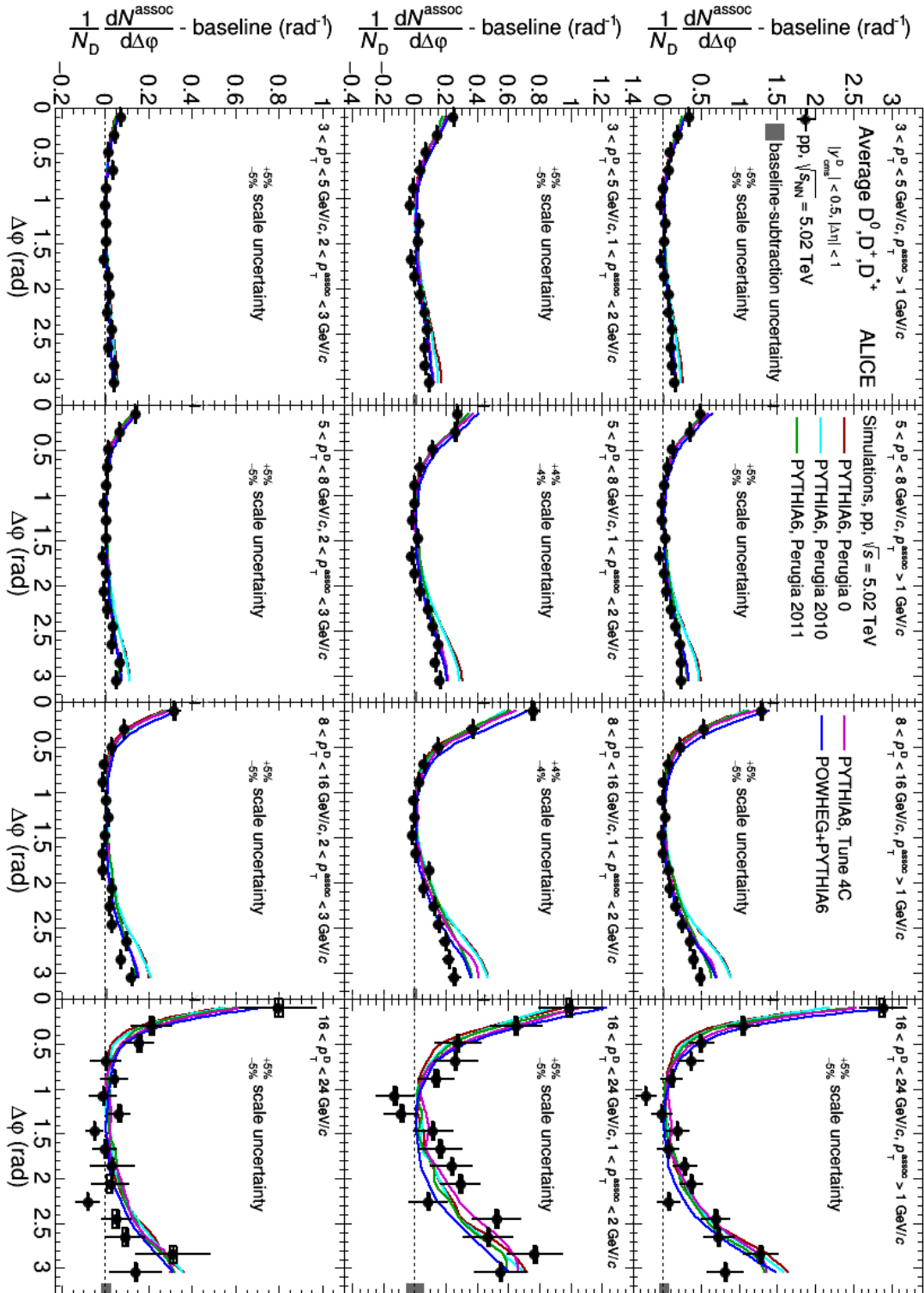
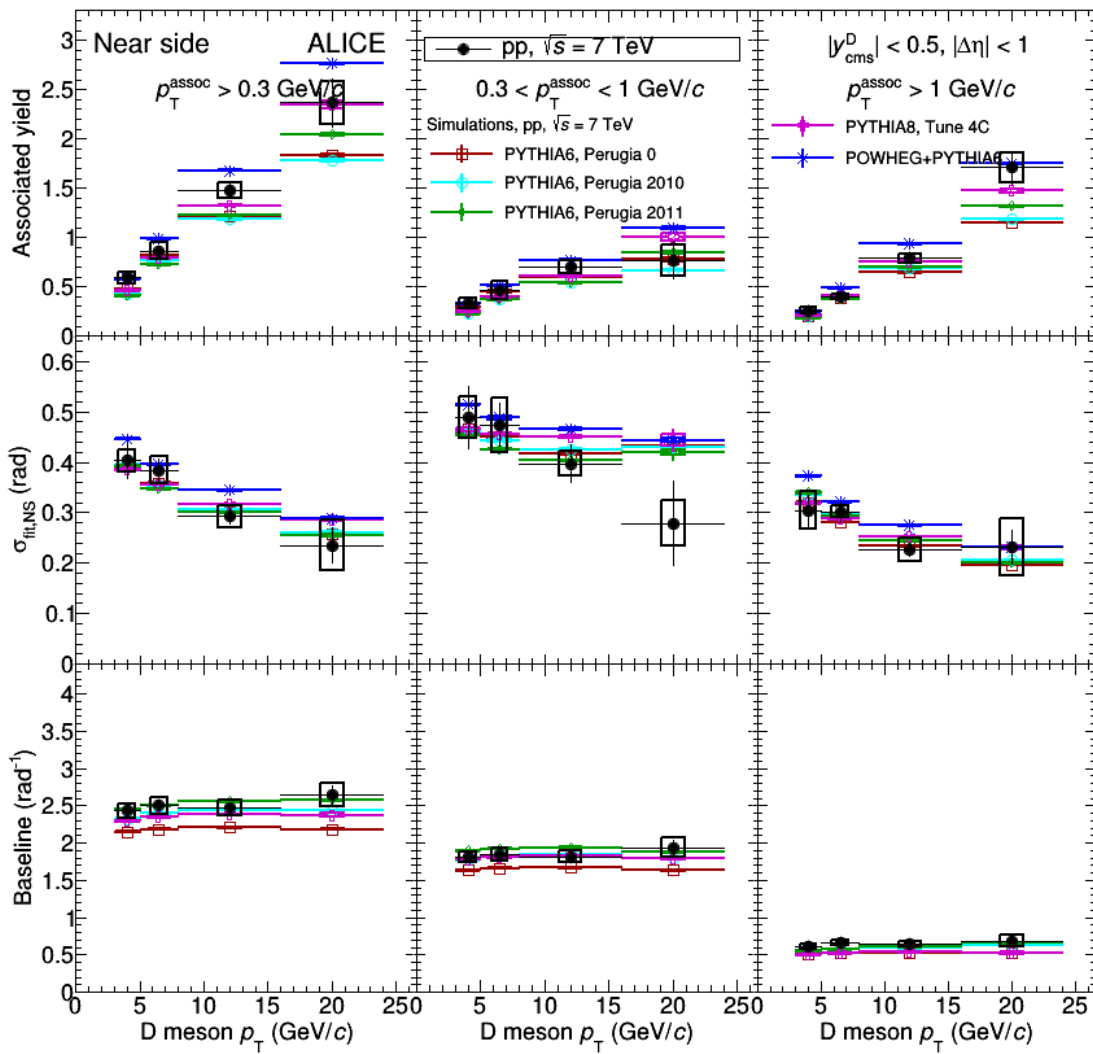


Figure 83: Comparison of $\Delta\phi$ azimuthal distribution for D-meson averages, obtained from data and simulations different event generators (PYTHIA, with three tunes, and POWHEG+PYTHIA), in the different kinematic ranges analyzed.



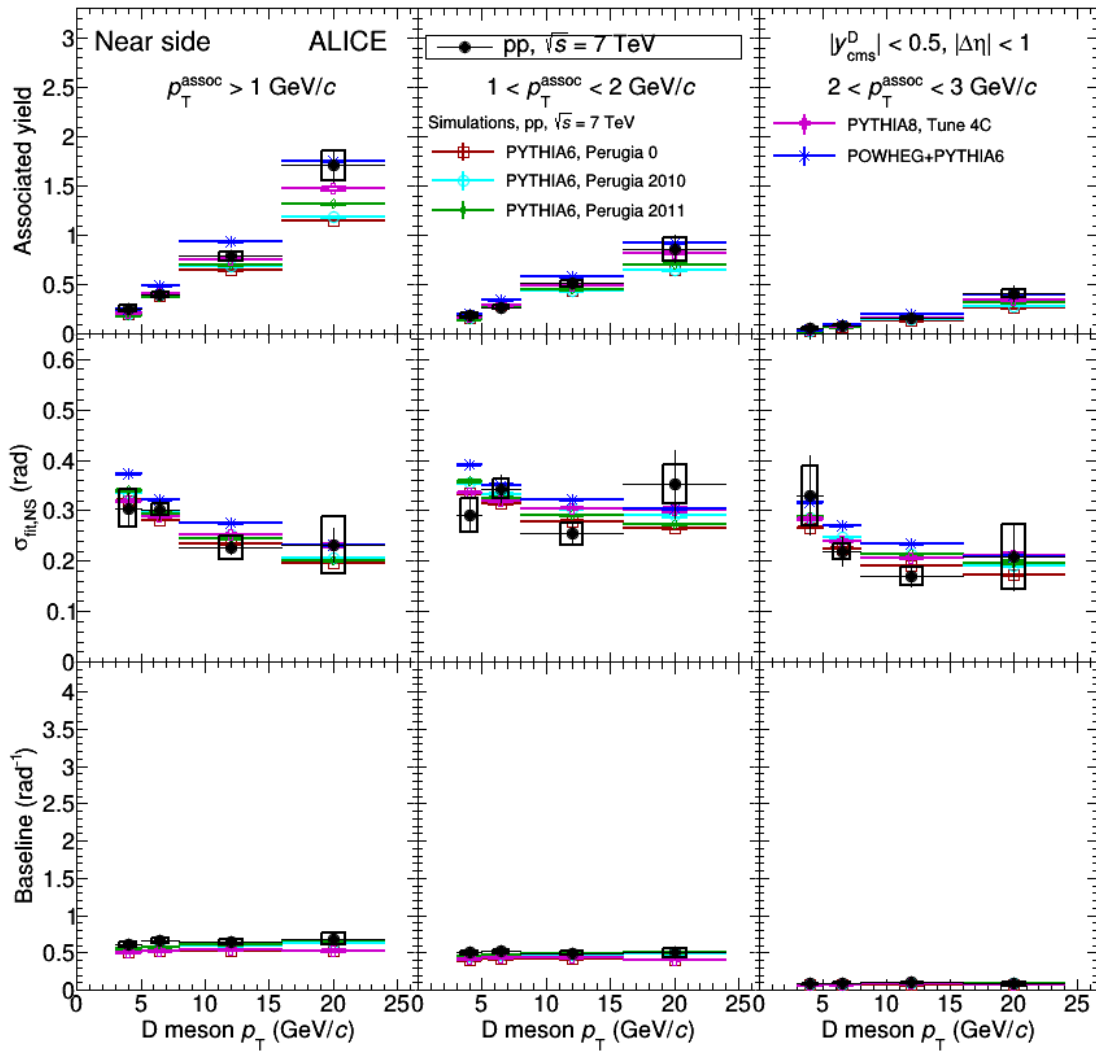
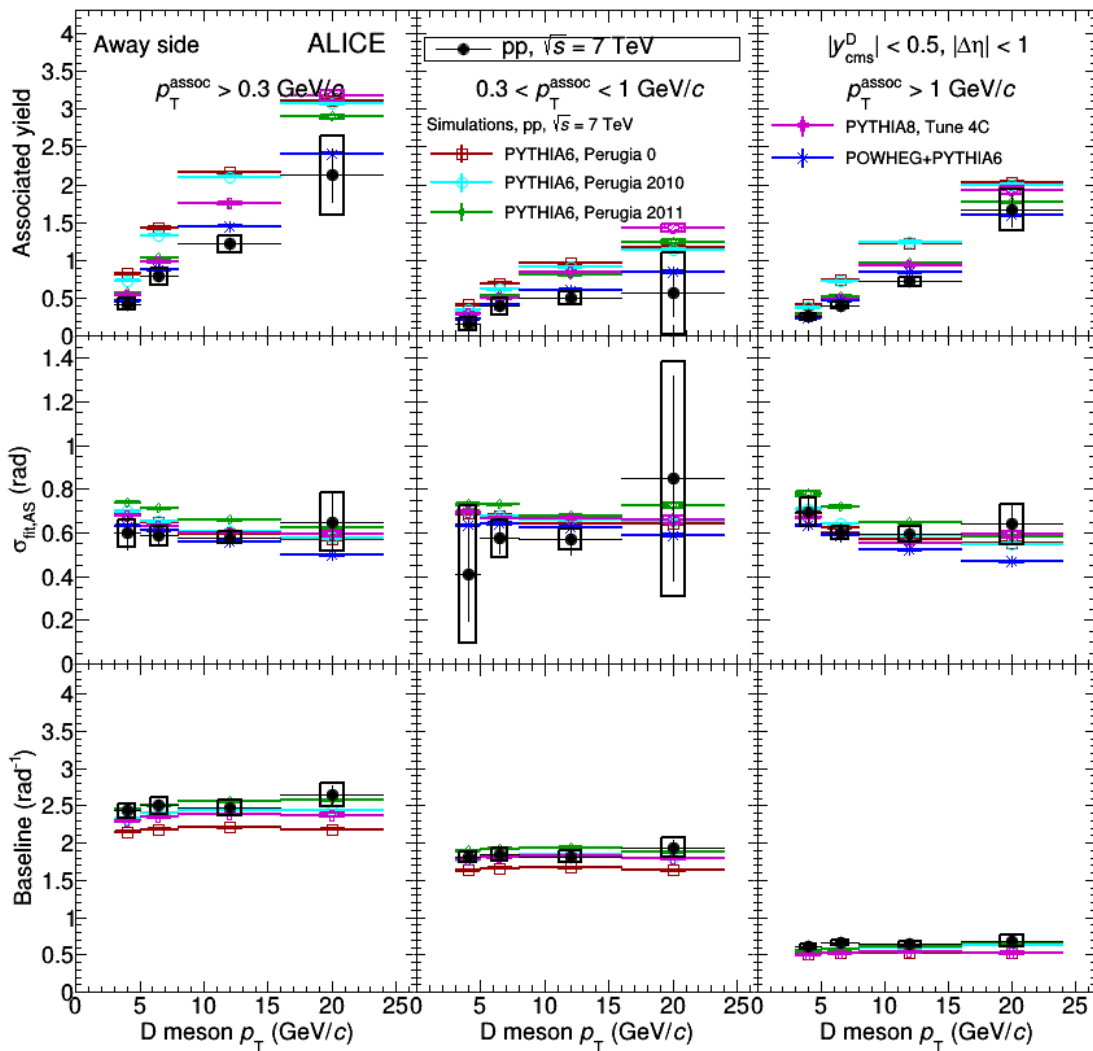


Figure 84: Near-side fit parameters obtained for D-meson averages, extracted from data and simulations different event generators (PYTHIA6 with three tunes, PYTHIA8 and POWHEG+PYTHIA), in the different kinematic ranges analyzed.



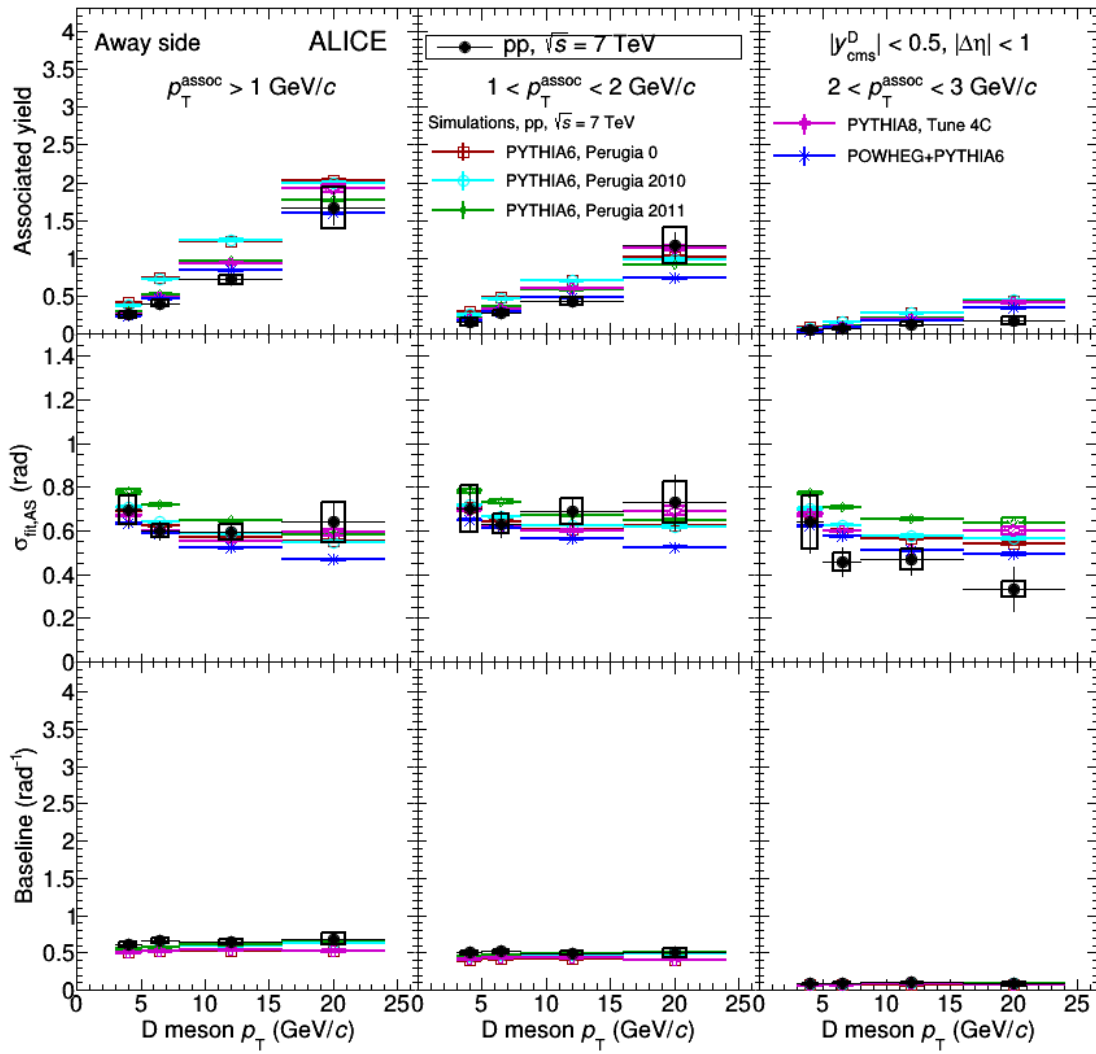


Figure 85: Near-side fit parameters obtained for D-meson averages, extracted from data and simulations different event generators (PYTHIA6, with three tunes, PYTHIA8 and POWHEG+PYTHIA), in the different kinematic ranges analyzed.

5.7 Planned results for HP approvals

We are planning to approve the following results, all shown in the previous figures (the final graphical style of the plots is still to be finalized):

- Average D-h correlation distributions, multipanel and in exemplary pT range
- Comparison of correlation distributions with expectations from models
- Comparison of fit observables with expectations from models (NS and AS)
- Comparison of correlation distributions with p-Pb results
- Comparison of fit observables with p-Pb results (NS and AS)
- Comparison of correlation distributions with p-Pb results
- Comparison of fit observables with p-Pb results (NS only)

802 **6 Bibliography**

803 **References**

- 804 [1] B. Abelev et al. [ALICE Collaboration], JHEP **01** (2012) 128
805 [2] B. Abelev et al. [ALICE Collaboration], Eur. Phys. J. C (2017) 77:245
806 [3] B. Abelev et al. [ALICE Collaboration], Phys.Lett. B719 (2013) 29-41
807 [4] B. Abelev et al. [ALICE Collaboration], Phys.Lett. B726 (2013) 164-177
808 [5] <https://aliceinfo.cern.ch/Figure/node/12130> (ALI-PREL-138003)
809 [6] ALICE Collaboration, arXiv:1609.06643 [nucl-ex]
810 [7] <https://aliceinfo.cern.ch/Notes/node/785>
811 [8] <https://aliceinfo.cern.ch/Notes/node/238>
812 [9] <https://aliceinfo.cern.ch/Notes/node/201>